Dipl.-Ing. Patrick Lainer, BSc

Hybrid Kinetic/MHD Modeling of Plasma Response to 3D Magnetic Perturbations in Tokamaks

DOCTORAL THESIS

to achieve the university degree of

Doktor der technischen Wissenschaften

submitted to

Graz University of Technology

Supervisor

Ao.Univ.-Prof.i.R. Dipl.-Ing. Dr.phil. Martin Heyn

Institute of Theoretical and Computational Physics

Graz, October 2024

AFFIDAVIT

I declare that I have authored this thesis independently, that I have not used other than the declared sources/resources, and that I have explicitly indicated all material which has been quoted either literally or by content from the sources used. The text document uploaded to TUGRAZonline is identical to the present doctoral thesis.

Date, Signature

Abstract

This thesis introduces a hybrid kinetic-MHD approach for the linear modelling of the interaction of resonant magnetic perturbations (RMPs) with tokamak plasmas. The model uses an iterative scheme where the solution of Ampère's law in realistic device geometry is combined with the computation of plasma response currents to a given magnetic perturbation. The latter computation employs the ideal MHD model in most of the plasma volume, and a collisional kinetic model inside the resonant layers centered around rational flux surfaces. Within a 1D kinetic model, a straight inhomogeneous plasma cylinder geometry is assumed, and the finite Larmor radius expansion of plasma response currents and charge densities up to second order is employed. For the solution of magnetostatic equations, a Fourier-finite-element method is introduced in order to decouple the solutions of the toroidal harmonics in two dimensions. The hybrid kinetic-MHD model is implemented in the code MEPHIT and applied to RMPs in ASDEX Upgrade experiments on edge-localized mode (ELM) suppression. The results of these simulations are compared to the results of the ideal MHD code GPEC, achieving at least qualitative agreement when the ideal MHD plasma response currents are used in MEPHIT. Application of the plasma response current from the kinetic model results in a markedly different picture, which might help explain the sensitivity to isotope content in ELM suppression experiments in the future.

Kurzfassung

In der vorliegenden Arbeit wird ein hybrider Ansatz aus kinetischer Theorie und MHD für die lineare Modellierung der Wechselwirkung von resonanten magnetischen Störungen (RMPs) mit Tokamak-Plasmen vorgestellt. Das Modell verwendet ein Iterationsschema, bei dem die Lösung des Ampèreschen Gesetzes in realistischer Tokamak-Geometrie mit der Berechnung der Plasma-Antwortströme aus einer gegebenen magnetischen Störung kombiniert wird. Für den letzteren Schritt kommt das ideale MHD-Modell im größten Teil des Plasmavolumens zur Anwendung, während die Berechnung innerhalb der resonanten Schichten, die die rationalen Flussflächen umgeben, nach einem kinetischen Modell mit Kollisionen erfolgt. In diesem eindimensionalen kinetischen Modell wird für das Plasma die Geometrie eines geraden, inhomogenen Zylinders angenommen und die Taylor-Reihe des Larmor-Radius in den Strömen und Ladungsdichten bis zur zweiten Ordnung entwickelt. Für die Lösung der magnetostatischen Gleichungen wird eine Fourier-Finite-Element-Methode eingeführt, um die Lösungen der toroidalen Fourier-Moden in zwei Dimensionen zu entkoppeln. Der Code MEPHIT implementiert dieses hybride Kinetik-MHD-Modell und wird auf Experimente zur Unterdrückung von *edge-localized modes* (ELMs) in ASDEX Upgrade angewendet. Diese Ergebnisse werden mit den Ergebnissen des idealen MHD-Codes GPEC verglichen, wobei zumindest qualitative Übereinstimmung erreicht wird, wenn die Plasma-Antwortströme gemäß dem idealen MHD-Modell berechnet werden. Werden die Plasma-Antwortströme gemäß dem kinetischen Modell berechnet, ergibt sich ein deutlich anderes Bild, das in Zukunft dazu beitragen könnte, die Abhängigkeit vom Isotopengehalt in Experiementen zur Untedrückung von ELMs zu erklären.

Contents

Acknowledgement

I want to thank Winfried Kernbichler, who provided me with the opportunity to pursue this research in the first place. As former head of the research group, he fostered an environment that encourages discussion and attention to detail, which also applied to our efforts in regards to teaching. My sincerest gratitude also extends to his successor Christopher Albert, whose perpetual guidance and advice helped me to keep the bigger picture in mind and put things into perspective. To Martin Heyn I am thankful for his supervision and thorough feedback. I am further indebted to Sergei Kasilov, whose insight and immense knowledge were of vital importance to the success of this endeavour. The great atmosphere in our research group certainly contributed as well, especially the fruitful discussions with Rico Buchholz, Markus Markl, Michael Reichelt, Michael Eder, Jonatan Schatzlmayr, and Georg Graßler. It was a pleasure working with you. Another special mention goes to Andreas Hirczy, who has put up with our demands for technical infrastructure. Last but not least, I am grateful for my friends and family, for their continuous support over all this time, and for helping me focus on what is important.

"Без муке нема науке."

This work has received funding from the KKKÖ at ÖAW.
This work has been carried out within the framework of the EUROfusion Consortium, funded by the European Union via the Euratom Research and Training Programme (Grant Agreement No 101052200 — EUROfusion). Views and opinions expressed are however those of the author(s) only and do not necessarily reflect those of the European Union or the European Commission. Neither the European Union nor the European Commission can be held responsible for them.

Chapter 1

Introduction

The class of plasma instabilities known as edge-localized modes (ELMs) is of special concern in tokamaks operating in the high-confinement mode, such as ASDEX Upgrade and the future ITER facility. One strategy for ELM mitigation is the application of resonant magnetic perturbations (RMPs) via external coils, as indicated in figure 1.2. Kinetic modeling accurately describes the plasma response to these RMPs *ab initio*, particularly the parallel shielding currents at resonant surfaces. The straight-cylinder approximation applied here still yields adequate results in the sense that it is free of the errors introduced with the simplifications resulting from fluid theory. Away from resonant surfaces, ideal magnetohydrodynamics (iMHD) is expected to yield sufficiently accurate results, providing a computationally less expensive option that could complement kinetic modeling.

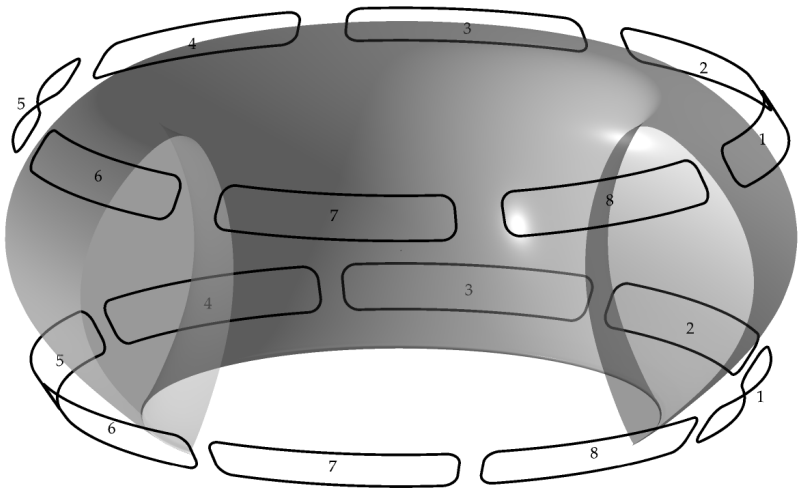

Figure 1.1: Eight sets of RMP coils ("B coils") are arranged in upper and lower position of ASDEX Upgrade. Coil currents are of the order 6.5 kA-turns and are approximately fitted to $\sin(2\varphi + \delta)$ with some phase shift δ, meaning the toroidal mode $n = 2$ is dominant in the resulting vacuum perturbation field. For reference, the separatrix up to the X-point is extruded.

The code MEPHIT has been developed to solve the linearized iMHD equations in a way that is compatible with iterative kinetic modeling approaches. We consider an axisymmetric iMHD equilibrium in realistic tokamak geometry under the influence of a quasi-static non-axisymmetric external perturbation from ELM mitigation coils. The plasma responds to this external magnetic perturbation with a current perturbation, which in turn produces a magnetic field perturbation. The resulting fixed-point equation can be solved in a self-

consistent manner by preconditioned iterations in which Ampère's equation and the magnetic differential equations for pressure and current are solved in alternation until convergence is reached. After expansion in toroidal Fourier harmonics, these equations are solved on a triangular mesh in the poloidal plane using finite elements.

Results that are part of this thesis have been published in [1, 2, 3, 4], where parts of the present text, including this introduction, can be found with some modifications. The corresponding references are marked in the text where appropriate.

1.1 Magnetic Field Structure and Geometric Considerations

Since the idealized tokamak is axisymmetric, it is convenient to work in cylindrical coordinates (R, φ, Z) and assume the fields are independent of φ. With these assumptions, the ideal MHD force balance yields the Grad–Shafranov equation,

$$\Delta^* \psi := R \frac{\partial}{\partial R}\left(\frac{1}{R}\frac{\partial \psi}{\partial R}\right) + \frac{\partial^2 \psi}{\partial Z^2} = -F\frac{\mathrm{d}F}{\mathrm{d}\psi} - R^2\frac{\mathrm{d}p}{\mathrm{d}\psi}, \tag{1.1}$$

a nonlinear elliptical second-order PDE for the *stream function* $\psi(R, Z)$ with the given *profiles* $p(\psi)$ and $F(\psi)$, which generally cannot be solved analytically. ψ is a normalized poloidal magnetic flux, $\Psi_{\mathrm{pol}} = 2\pi\psi$, but it can also be interpreted as the covariant toroidal component of the magnetic vector potential, $\psi = A_\varphi$. Thus, the poloidal components of the magnetic field can be recovered from ψ:

$$\hat{B}_R = -\frac{1}{R}\frac{\partial \psi}{\partial Z}, \qquad \hat{B}_R = \frac{1}{R}\frac{\partial \psi}{\partial R}. \tag{1.2}$$

Since F is identical to the covariant toroidal component of the magnetic field, $F = B_\varphi$, the *physical* toroidal component of the magnetic field is simply given by

$$\hat{B}_\varphi = \frac{F}{R}. \tag{1.3}$$

Applying Ampère's law, we find for the poloidal components of the current density

$$\hat{J}_R = \frac{c}{4\pi}F'(\psi)\hat{B}_R, \qquad \hat{J}_Z = \frac{c}{4\pi}F'(\psi)\hat{B}_Z, \tag{1.4}$$

which is why F is also called the *poloidal current function*. For the toroidal component of the current density, we find it is proportional to the right-hand side of (1.1),

$$\hat{J}_\varphi = cRp'(\psi) + \frac{c}{4\pi R}FF'(\psi). \tag{1.5}$$

Thus the solution of the Grad-Shafranov equation yields the *equilibrium* magnetic field and current density. This axisymmetric equilibrium is characterized by nested closed *magnetic flux*

surfaces (contours of constant ψ in the poloidal cross-section) in the *core plasma* surrounding the *magnetic axis* or *O-point*, the degenerate innermost magnetic flux surface. The core plasma is surrounded by the *scrape-off layer* where flux surfaces are not closed but intersect with the *divertor* plates at the bottom of the device. The boundary between core plasma and scrape-off layer is called the *separatrix*. It self-intersects at the *X-point*, a *poloidal null* or saddle point where the poloidal magnetic field vanishes. Below the X-point is the *private flux region* where flux surfaces also connect to the divertors. The resulting geometry and associated coordinate systems (see below) are illustrated in figure 1.1.

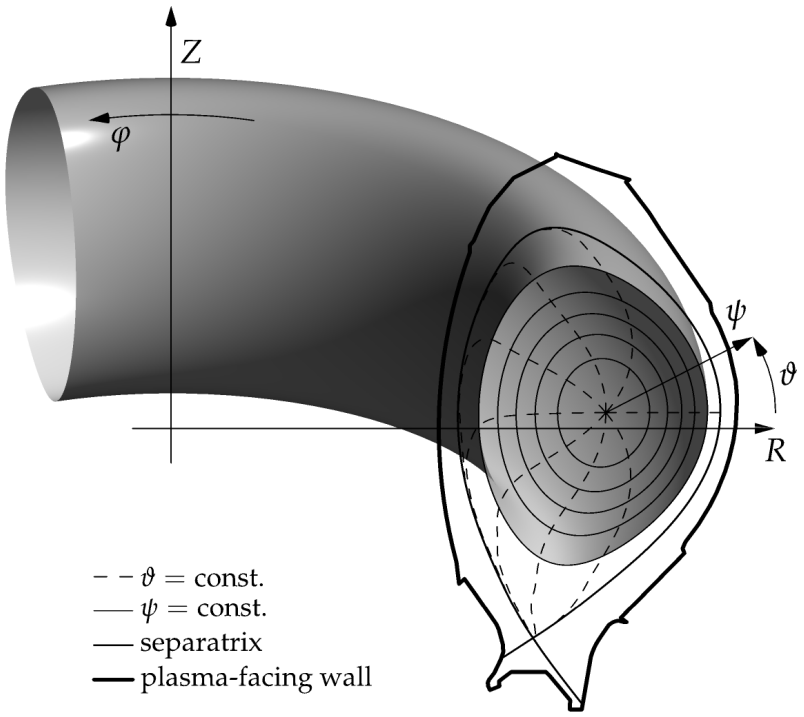

Figure 1.2: Poloidal cross-section of a tokamak plasma with nested flux surface cross-sections, one of which is extruded in toroidal direction. Coordinate directions are indicated by arrows for (R, φ, Z) and $(\psi, \varphi, \vartheta)$. The separatrix is not a closed flux surface and extends beyond the saddle point (X-point). The symmetry flux coordinate ϑ is distorted compared to the geometrical angle θ and is only defined up to the separatrix. Data is taken from ASDEX Upgrade shot #33353 at 2325 ms.

To describe this magnetic field structure, we additionally introduce pseudo-toroidal coordinates $(\varrho, \varphi, \vartheta)$. The plane perpendicular to the direction of φ is spanned by (R, Z) for cylindrical coordinates, which behave similarly to Cartesian coordinates, and by (ϱ, ϑ) for pseudo-toroidal coordinates, which behave similarly to bipolar coordinates. Here, we follow the convention of D'haeseleer et al. [5], where ϱ is a *flux surface label* which increases strictly monotonically from the axis outwards. In principle, any strictly monotonic flux surface quantity can be chosen for the actual coordinate, and we choose ψ. However, ψ might increase or decrease depending on the direction of the poloidal magnetic field it describes, and we write $\psi = \sigma_{\psi'} \varrho$, with $\sigma_{\psi'} = \psi'(\varrho) = \pm 1$ denoting the sign of the radial derivative. This way, we can maintain $(\varrho, \varphi, \vartheta)$ as a right-handed system with a positive Jacobian $\sqrt{g}$, and still accomodate

both possible variants with regard to ψ whenever the sign is relevant. For the system to be right-handed, φ and ϑ are also assumed to point in counter-clockwise direction, but see section 4.7 for more details.

There are multiple options to define φ and ϑ, but we already implied by notation that the toroidal angle φ of our pseudo-toroidal coordinates is the same as the azimuthal angle φ of cylindrical coordinates. With $\varrho = \sigma_{\psi'}\psi$ also fixed, this still leaves some freedom in defining ϑ, when allowing for a generalized notion of a poloidal "angle". There is a unique choice such that magnetic field lines are straight lines in (φ, ϑ) for fixed ψ, resulting in *symmetry flux coordinates* or PEST coordinates [6],

$$\left(\frac{\mathrm{d}\varphi}{\mathrm{d}\vartheta}\right)_{\psi=\text{const.}} = |q(\psi)|, \tag{1.6}$$

with the *safety factor* q. The safety factor describes the number of toroidal windings per poloidal winding of field lines on a particular flux surface labelled by ψ. The Jacobian of these coordinates is then given by

$$\sqrt{g} = \frac{\sigma_{\psi'}}{B_0^\vartheta} = \frac{q(\psi)}{F(\psi)} R^2 \sigma_{\psi'}. \tag{1.7}$$

Using (1.3), we can also express the safety factor via

$$q = \frac{B_0^\varphi}{B_0^\vartheta}. \tag{1.8}$$

As a consequence of the above, ϑ, $\sqrt{g}$, and some related quantities depend on the given equilibrium magnetic field and can only be obtained numerically in general. This procedure is described in section 4.1. Furthermore, since ψ and ϑ are generally not orthogonal to each other, it is expedient to use the co-/contravariant formalism, which is covered by D'haeseleer et al. [5] and briefly explained in section 2.1, albeit with some modifications to the notation.

Even if some quantity f is not axisymmetric, it still needs to be periodic in φ and thus lends itself to Fourier series expansion in φ,

$$f(R, \varphi, Z) = \sum_{n=-\infty}^{\infty} f_n(R, Z) \mathrm{e}^{\mathrm{i}n\varphi}. \tag{1.9}$$

When f is real-valued, toroidal Fourier amplitudes f_n with negative n are just the complex conjugate of the corresponding toroidal Fourier amplitude with positive n, i.e. $f_{-n} = f_n^*$. Thus we only need to consider positive n, which simplifies the sum to

$$f(R, \varphi, Z) = f_0(R, Z) + 2\,\mathrm{Re} \sum_{n=1}^{\infty} f_n(R, Z) \mathrm{e}^{\mathrm{i}n\varphi}. \tag{1.10}$$

This also highlights the distinction between axisymmetric and non-axisymmetric Fourier amplitudes, which is further discussed in section 2.1 along with Fourier series expansion of vector-valued quantities. If the toroidal Fourier series expansion is used with symmetry flux coordinates instead of cylindrical coordinates, poloidal Fourier series expansion can be applied subsequently:

$$f_n(\psi, \vartheta) = \sum_{m=-\infty}^{\infty} f_{mn}(\psi) \mathrm{e}^{\mathrm{i}m\vartheta}. \tag{1.11}$$

If we take the discrete Fourier transform of some $\sqrt{g} f_n$, the result is a convolution involving f_{mn} because $\sqrt{g}$ also depends on ϑ. Due to this *poloidal mode coupling*, the poloidal Fourier amplitudes are generally affected by neighbouring poloidal modes in toroidal geometry.

The choice of the coordinate system depends on the context; analytical derivations are often only feasible in symmetry flux coordinates including the above toroidal-poloidal decomposition. On the other hand, the coordinate singularity at the magnetic axis can be problematic for numerical calculations, which is one reason why MEPHIT uses cylindrical coordinates in the implementation. The coordinate singularity of cylindrical coordinates is less of a problem because the cylindrical axis is usually outside the computational domain of interest, but see section 2.1 for a counter-example.

A further coordinate system arises from a simplification of the toroidal geometry where a circular torus is cut open at a poloidal cross-section and "unbent" into a straight cylinder with coordinates (r, θ, z) and periodic boundary conditions in z to connect the two ends of the cylinder. The transformation to cylindrical coordinates is given by

$$R = R_0 + r\cos\theta, \qquad \varphi = \frac{z}{R_0}, \qquad Z = r\sin\theta. \tag{1.12}$$

This approximation is also called the *large aspect ratio* limit $A \to \infty$, where the aspect ratio

$$A = \frac{R_0}{a} \tag{1.13}$$

is the ratio of major radius R_0 and minor radius a. In this approximation, the flux poloidal angle ϑ reduces to the geometric poloidal angle θ, and the metric determinant reduces to $\sqrt{g} = r$, where r is usually the actual geomtric radius of the concentrically nested flux surfaces. As a consequence, no poloidal mode coupling occurs, and we can write the Fourier series expansion as

$$f(r, \theta, z) = \sum_{\boldsymbol{k}} f_{\boldsymbol{k}}(r) \mathrm{e}^{\mathrm{i}m\theta + \mathrm{i}k_z z}, \tag{1.14}$$

where the wave vector is given as

$$\boldsymbol{k} = m\nabla\theta + k_z \nabla z = m\nabla\theta + \frac{n}{R_0}\nabla z. \tag{1.15}$$

Chapter 2

Stationary Linear Perturbation of Linear Ideal MHD Equilibrium

This section has already been published in summarised form [2, 7].

Regardless of the geometry and the underlying plasma model, we can abstract the setup as follows. An axisymmetric equilibrium is characterized by its magnetic field $\boldsymbol{B}_0$, its current density $\boldsymbol{J}_0$, and its pressure p_0. A small non-axisymmetric perturbation (of relative order 10^{-4}) is applied to the equilibrium by switching on additional coils outside the plasma region as pictured in figure 1.2. The resulting coil field in the absence of plasma is variously called the external or *vacuum perturbation* field, $\delta\boldsymbol{B}_\mathrm{v}$. $\delta\boldsymbol{B}_\mathrm{v}$ induces a *plasma response current* density $\delta\boldsymbol{J}$, which produces a *plasma perturbation* field $\delta\boldsymbol{B}_\mathrm{p}$, in turn changing $\delta\boldsymbol{J}$. To arrive at a self-consistent solution, the *perturbed equilibrium*, we use a fixed-point iteration as follows.

$\delta\boldsymbol{B}_\mathrm{v}$ is computed for given coil currents with the Biot-Savart law and is fixed within iterations, assuming no feedback on the external coils from the plasma. $\delta\boldsymbol{B}_\mathrm{p}$ is computed via Ampère's law from $\delta\boldsymbol{J}$ in every iteration step, which we denote with an operator $\hat{M}$,

$$\nabla \times \delta\boldsymbol{B}_\mathrm{p} = \nabla \times \left(\nabla \times \delta\boldsymbol{A}_\mathrm{p}\right) = \frac{4\pi}{c}\delta\boldsymbol{J} \quad \leftrightarrow \quad \delta\boldsymbol{B}_\mathrm{p} = \hat{M}\delta\boldsymbol{J}. \tag{2.1}$$

Note that we do not need to distinguish between plasma and external contributions as we do for the magnetic field and the associated vector potential since the coil currents are outside the computational domain, i.e., the plasma region, and so we omit the subscript for plasma here.

$\delta\boldsymbol{J}$ is computed from the *full perturbation* $\delta\boldsymbol{B} = \delta\boldsymbol{B}_\mathrm{v} + \delta\boldsymbol{B}_\mathrm{p}$ in every iteration step using a suitable plasma model, e.g., ideal MHD, resistive MHD, or a more general description from kinetic theory [7]. Moreover, different models can be used for different regions. We represent this again with an operator $\hat{P}$,

$$\delta\boldsymbol{J} = \hat{P}\delta\boldsymbol{B} = \hat{P}\left(\delta\boldsymbol{B}_\mathrm{p} + \delta\boldsymbol{B}_\mathrm{v}\right). \tag{2.2}$$

We substitute $\delta\boldsymbol{J}$ from (2.2) into (2.1) and use the shorthand $\hat{K} = \hat{M}\hat{P}$ for a complete iteration step to arrive at a fixed-point equation for $\delta\boldsymbol{B}_\mathrm{p}$,

$$\delta\boldsymbol{B}_\mathrm{p} = \hat{K}\left(\delta\boldsymbol{B}_\mathrm{p} + \delta\boldsymbol{B}_\mathrm{v}\right). \tag{2.3}$$

Adding $\delta \boldsymbol{B}_\mathrm{v}$ on both sides yields a fixed-point equation for the full perturbation,

$$\delta \boldsymbol{B} = \hat{K} \delta \boldsymbol{B} + \delta \boldsymbol{B}_\mathrm{v}. \tag{2.4}$$

Repeated application of $\hat{K}$ corresponds to direct iterations with the initial value given by the vacuum field,

$$\delta \boldsymbol{B}^{[k+1]} = \hat{K} \delta \boldsymbol{B}^{[k]} + \delta \boldsymbol{B}_\mathrm{v}, \quad \delta \boldsymbol{B}^{[0]} = \delta \boldsymbol{B}_\mathrm{v}. \tag{2.5}$$

To obtain convergence conditions for linear $\hat{K}$, consider the explicit form of (2.4),

$$\delta \boldsymbol{B} = \left(\hat{I} - \hat{K}\right)^{-1} \delta \boldsymbol{B}_\mathrm{v} = \sum_{k=0}^{\infty} \hat{K}^k \delta \boldsymbol{B}_\mathrm{v}, \tag{2.6}$$

where the equality with the Neumann series holds if and only if the series converges. Assuming non-singular $\hat{K}$, we can formally write its eigendecomposition as

$$\hat{K} = \hat{V} \hat{\Lambda} \hat{V}^{-1}. \tag{2.7}$$

The Neumann series reduces to geometric series for the eigenvalues λ_k in the diagonal of $\hat{\Lambda}$, which yields the convergence condition $|\lambda_k| < 1 \ \forall k$. Since this is generally not the case, we introduce a preconditioning scheme as follows. We rearrange (2.4),

$$\left(\hat{I} - \hat{K}\right) \delta \boldsymbol{B} = \delta \boldsymbol{B}_\mathrm{v}, \tag{2.8}$$

apply a full-rank linear operator $\hat{\Pi}$,

$$\left(\hat{I} - \hat{\Pi}\right) \left(\hat{I} - \hat{K}\right) \delta \boldsymbol{B} = \left(\hat{I} - \hat{\Pi}\right) \delta \boldsymbol{B}_\mathrm{v}, \tag{2.9}$$

and regroup to arrive at

$$\left(\hat{I} - \hat{\bar{K}}\right) \delta \boldsymbol{B} = \delta \bar{\boldsymbol{B}}_\mathrm{v}, \tag{2.10}$$

where

$$\hat{\bar{K}} = \hat{\Pi} + \left(\hat{I} - \hat{\Pi}\right) \hat{K}, \tag{2.11}$$

$$\delta \bar{\boldsymbol{B}}_\mathrm{v} = \left(\hat{I} - \hat{\Pi}\right) \delta \boldsymbol{B}_\mathrm{v}. \tag{2.12}$$

Since (2.10) has the same form as (2.8), we can write preconditioned iterations in analogy to the direct iterations of (2.5),

$$\delta \bar{\boldsymbol{B}}^{[k+1]} = \hat{\bar{K}} \delta \bar{\boldsymbol{B}}^{[k]} + \delta \bar{\boldsymbol{B}}_\mathrm{v}, \quad \delta \bar{\boldsymbol{B}}^{[0]} = \delta \bar{\boldsymbol{B}}_\mathrm{v}, \tag{2.13}$$

which converge to the same result, i.e., $\delta \bar{\boldsymbol{B}} \to \delta \boldsymbol{B}$ for $k \to \infty$. Inserting (2.12) and (2.11) back

into (2.13),

$$\delta\bar{\boldsymbol{B}}^{[k+1]} = \hat{\Pi}\delta\bar{\boldsymbol{B}}^{[k]} + \left(\hat{I} - \hat{\Pi}\right)\left(\hat{K}\delta\bar{\boldsymbol{B}}^{[k]} + \delta\boldsymbol{B}_{\mathrm{v}}\right), \tag{2.14}$$

we see that the last parentheses capture the original direct iteration step, allowing us to rewrite (2.13) via the following two-part iteration step:

$$\delta\boldsymbol{B}^{[k+1]} = \hat{K}\delta\bar{\boldsymbol{B}}^{[k]} + \delta\boldsymbol{B}_{\mathrm{v}}, \tag{2.15}$$

$$\delta\bar{\boldsymbol{B}}^{[k+1]} = \delta\boldsymbol{B}^{[k+1]} + \hat{\Pi}\left(\delta\bar{\boldsymbol{B}}^{[k]} - \delta\boldsymbol{B}^{[k+1]}\right). \tag{2.16}$$

This preconditioned iteration only requires one additional matrix-vector multiplication per step, with $\hat{\Pi}$ to be determined.

The Arnoldi iteration described in further detail in section 4.6 yields approximations to the eigenvalues of largest magnitude and the associated eigenvectors, the so-called Ritz values and vectors. Thus, we consider only the r largest eigenvalues λ_k above a given threshold $\lambda_{\mathrm{sup}} \leq 1$,

$$|\lambda_k| \geq \lambda_{\mathrm{sup}} \quad \forall k \leq r. \tag{2.17}$$

Instead of the full eigendecomposition of $\hat{K}$ as in (2.7), we get a reduced eigendecomposition,

$$\hat{K}\hat{V}_r = \hat{V}_r\hat{\Lambda}_r, \tag{2.18}$$

with an $N \times r$ matrix of Ritz vectors and an $r \times r$ matrix of Ritz values. This allows us to demand

$$\hat{\tilde{K}}\hat{V}_r \stackrel{!}{=} \hat{0}, \tag{2.19}$$

so that these eigenvalues do not contribute to the preconditioned iterations in (2.13). Inserting (2.11), we get

$$\left(\hat{\Pi} + \left(\hat{I} - \hat{\Pi}\right)\hat{K}\right)\hat{V}_r = \hat{0}, \tag{2.20}$$

to which we apply (2.18), giving

$$\hat{\Pi}\hat{V}_r + \left(\hat{I} - \hat{\Pi}\right)\hat{V}_r\hat{\Lambda}_r = \hat{0}. \tag{2.21}$$

Rearrangement yields

$$\hat{\Pi}\hat{V}_r = \hat{V}_r\hat{\Lambda}_r\left(\hat{\Lambda}_r - \hat{I}\right)^{-1}, \tag{2.22}$$

but rectangular $\hat{V}_r$ cannot be inverted. Instead, we insert a unity term on the right-hand side,

$$\hat{\Pi}\hat{V}_r = \hat{V}_r\hat{\Lambda}_r\left(\hat{\Lambda}_r - \hat{I}\right)^{-1}\left(\hat{V}_r^\dagger\hat{V}_r\right)^{-1}\hat{V}_r^\dagger\hat{V}_r, \tag{2.23}$$

and comparison results in

$$\hat{\Pi} = \hat{V}_r\hat{\Lambda}_r\left(\hat{V}_r^\dagger\hat{V}_r\left(\hat{\Lambda}_r - \hat{I}\right)\right)^{-1}\hat{V}_r^\dagger. \tag{2.24}$$

Effectively, we have partially diagonalized $\hat{K}$ in the Krylov subspace of the largest eigenvalues, and continue with preconditioned iterations to solve the fixed-point equation in the complementary subspace. λ_{sup} is then the supremum of the *remaining* eigenvalues and the geometric series in λ_{sup} then serves as a convergent major to the Neumann series in (2.6). In MEPHIT, $\delta\boldsymbol{B}$ is represented as an array of size N with typical values on the order of 10^5, while the number r of eigenvalues is usually on the order of 10^1. By the choice of λ_{sup}, the necessary number of Arnoldi iteration steps and the succeeding preconditioned iteration steps can in principle be balanced against each other.

2.1 Magnetic Field Perturbation

This section has already been published as part of [1] and contains the derivation of a method to solve the magnetostatic equations in certain symmetric domains efficiently by applying the Fourier transform to the finite element method. Validation and benchmarking examples for this general approach are attached as section 5.1. In MEPHIT, we use it to solve (2.1) on the poloidal plane with symmetry in the toroidal direction, thus realizing the operator $\hat{M}$. Note that SI units are used in this section.

The magnetostatic equations for magnetic field intensity $\boldsymbol{H}(\boldsymbol{r})$, magnetic flux density $\boldsymbol{B}(\boldsymbol{r})$, and current density $\boldsymbol{J}(\boldsymbol{r})$ as functions of position $\boldsymbol{r}$ are

$$\mathbf{curl}\,\boldsymbol{H} = \boldsymbol{J}, \tag{2.25}$$

$$\operatorname{div}\boldsymbol{B} = 0, \tag{2.26}$$

where $\boldsymbol{H}$ is related to $\boldsymbol{B}$ via the constitutive relation

$$\boldsymbol{H} = \hat{\nu}\boldsymbol{B} \tag{2.27}$$

with local reluctivity (inverse permeability) tensor $\hat{\nu}(\boldsymbol{r}) = \hat{\mu}(\boldsymbol{r})^{-1}$. Written in terms of a vector potential $\boldsymbol{A}(\boldsymbol{r})$ with $\mathbf{curl}\,\boldsymbol{A} = \boldsymbol{B}$, such that (2.26) is automatically fulfilled, they are equivalent to the curl-curl equation,

$$\mathbf{curl}(\hat{\nu}\,\mathbf{curl}\,\boldsymbol{A}) = \boldsymbol{J}, \tag{2.28}$$

as long as the domain is simply connected.

The goal of this method is to solve (2.28) on a finite three-dimensional domain Ω with a symmetry direction $\boldsymbol{e}^3 = \mathbf{grad}\, x^3$ along which the cross-section Ω_t does not change and where all sources and boundary conditions are 2π-periodic in x^3. An illustration in appropriately ordered cylindrical coordinates $x^1 = Z$, $x^2 = R$, $x^3 = \varphi$ is found in figure 2.1.

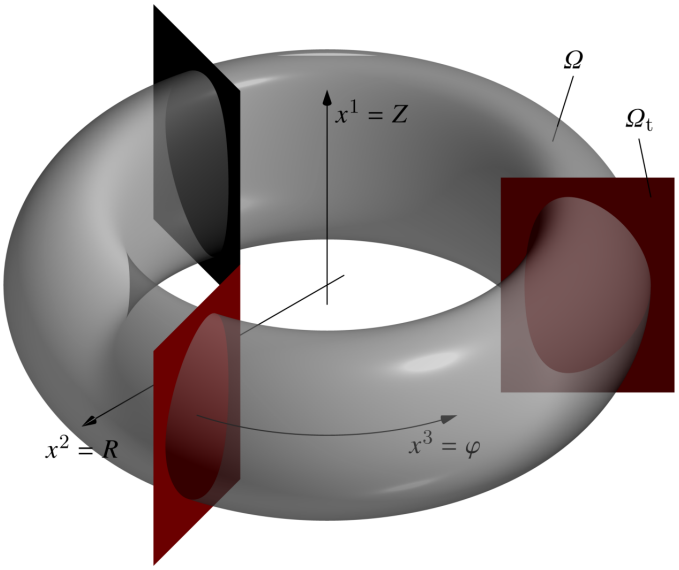

Figure 2.1: Example of an axisymmetric domain with indication of the coordinate axes for x^1, x^2, x^3. Note that the indicated transverse cross-sections do not change their shape along the symmetry direction x^3.

2.1.1 Vector Calculus in 3D and 2D Curvilinear Coordinates

Let (x^1, x^2, x^3) be right-handed curvilinear coordinates that uniquely describe any position $\boldsymbol{r} = \boldsymbol{r}(x^1, x^2, x^3)$ given by Cartesian components r^k in the relevant domain. Co- and contravariant basis vectors are respectively defined by

$$\boldsymbol{e}_k = \frac{\partial \boldsymbol{r}}{\partial x^k}, \qquad \boldsymbol{e}^k = \mathbf{grad}\, x^k, \tag{2.29}$$

and co- and contravariant components of vector fields $\boldsymbol{V}(\boldsymbol{r})$ by $V_k = \boldsymbol{V} \cdot \boldsymbol{e}_k$ and $V^k = \boldsymbol{V} \cdot \boldsymbol{e}^k$, respectively. Components g_{ij} of the metric tensor $\hat{g}$ are

$$g_{kl} = \boldsymbol{e}_k \cdot \boldsymbol{e}_l = g_{kl}(x^1, x^2, x^3), \tag{2.30}$$

and the metric determinant $g = \det[g_{kl}]$ is always positive, as we are considering right-handed systems. Its square-root $\sqrt{g}$ is equal to the Jacobian of the transformation to Cartesian coordinates and thus the weight of the volume element. The usual symmetry condition $g_{kl} = g_{lk}$ follows from the geometric definition of $\hat{g}$ in (2.30).

For the metric-free definition of differential operators and later use in their discretized form for numerics, it is useful to introduce densities of weight W as a generalization of scalars,

vectors, and tensors [8]. A density $\mathcal{U}$ (denoted in calligraphic letters) of weight W for a quantity U is defined as

$$\mathcal{U} = \sqrt{g}^{W} U, \tag{2.31}$$

where U can represent either a scalar, or co-/contravariant components of a vector or tensor field. If not stated otherwise, we use the term *density* for the default value $W = +1$. Usual scalars and vector/tensor components correspond to the case $W = 0$. Terms such as *contravariant vector density* and *contravariant density representation of a vector* will be used synonymously here for easier notation, as the conceptual difference has no practical concequence in the present context. A translation to notation in differential forms is found in table 2.1.

Table 2.1: Translation between terminology of classical tensor calculus and differential geometry in dimension N.

Tensor calculus	**Differential geometry**
scalar	0-form / scalar
scalar density	N-form
contravariant vector	vector
covariant vector	1-form / covector
contravariant vector density	$(N-1)$-form
rank-2 tensor densities	Hodge operators

Table 2.2: Natural input and output for differential operators in curvilinear coordinates. Densities are of weight +1 here.

Operator	**Notation**	**Argument**	**Result**
gradient	**grad**	scalar	covariant vector
curl	**curl**	covariant vector	contravariant vector density
divergence	div	contravariant vector density	scalar density
transverse gradient	$\mathbf{grad}_{\mathrm{t}}$	scalar	covariant vector
transverse scalar curl	$\mathrm{curl}_{\mathrm{t}}$	covariant vector	scalar density
transverse vector curl	$\mathbf{curl}_{\mathrm{t}}$	scalar	contravariant vector density
transverse divergence	$\mathrm{div}_{\mathrm{t}}$	contravariant vector density	scalar density

Table 2.2 lists the choice of input and output representation for differential operators such that the Jacobian $\sqrt{g}$ is formally removed from their definition. Note that the present notation only indicates co-/contravariance and densities for components, but not for abstract vectors, so for

example, we can write[1] $\boldsymbol{U} = \mathcal{U}^k \boldsymbol{e}_k$ or $\boldsymbol{V} = V_k \boldsymbol{e}^k$ and the distinction is given in the definition of each quantity. In this way, the coordinate-independent definitions of 3D divergence and gradient are

$$\mathbf{grad}\, U = \boldsymbol{e}^k \partial_k U, \qquad \operatorname{div} \boldsymbol{U} = \partial_k \mathcal{U}^k, \tag{2.32}$$

where the divergence acts on a contravariant vector density and yields a scalar density, and the gradient acts on a scalar field and yields a covariant vector field. The 3D curl operator

$$\mathbf{curl}\, \boldsymbol{U} = \epsilon^{ijk} \boldsymbol{e}_i \partial_j U_k \tag{2.33}$$

acts on a covariant vector field and yields a contravariant vector density. It contains the Levi–Civita tensor $\hat{\epsilon}$ with contravariant density components $\epsilon^{ijk} = 1$ for ijk being circular permutations of 123, -1 for circular permutations of 321, and 0 otherwise.

We want to treat the symmetry direction x^3 separately, splitting the problem into a longitudinal part along the symmetry direction, and a transverse part containing the remaining two dimensions. For the notation of abstract two-dimensional vectors as well as densities we use lowercase bold letters while components remain uppercase. We define two-dimensional transverse divergence and gradient operators analogous to the 3D case with

$$\mathbf{grad}_\mathrm{t}\, U = \boldsymbol{e}^1 \partial_1 U + \boldsymbol{e}^2 \partial_2 U, \qquad \operatorname{div}_\mathrm{t} \boldsymbol{u} = \partial_1 \mathcal{U}^1 + \partial_2 \mathcal{U}^2. \tag{2.34}$$

For the curl, in contrast to 3D, both a vectorial and a scalar transverse curl operator exist with

$$\mathbf{curl}_\mathrm{t}\, U = \boldsymbol{e}_1 \partial_2 U - \boldsymbol{e}_2 \partial_1 U, \qquad \operatorname{curl}_\mathrm{t} \boldsymbol{u} = \partial_1 U_2 - \partial_2 U_1, \tag{2.35}$$

yielding vector and scalar densities, respectively. Note that all four of these operations either take a scalar corresponding to the longitudinal part as input and give a two-dimensional vector corresponding to the transverse part as output, or vice versa.

Matching input and output of operators in table 2.2 reflect the de Rham complex [9] describing in which order operators may act between different function spaces. In 3D this is

$$H^1 \xrightarrow{\mathbf{grad}} H^{\mathbf{curl}} \xrightarrow{\mathbf{curl}} H^{\mathrm{div}} \xrightarrow{\mathrm{div}} L^2, \tag{2.36}$$

where application of two operators in a row yields zero, e.g., $\mathbf{curl}\,\mathbf{grad}\, U = 0$. This is the case for any de Rham complex. The 3D de Rham diagram leads from a scalar field in H^1 to a scalar density field in L^2. Here, L^2 is the space of square-integrable functions, and H^1 is the Sobolev space of such functions whose weak derivatives of first order are also square-integrable. $H^{\mathbf{curl}}$ and H^{div} are then limited to vector-valued functions whose curl and divergence are square-integrable, respectively.

[1] Here and later we use the notation $\partial_k = \partial/\partial x^k$, and the Einstein summation convention to sum over indices appearing twice, i.e. $\sum_{k=1}^{3}$ in (2.32).

Since the curl operator mixes vector components, and in order to distinguish between transverse and longitudinal parts, relation (2.36) breaks up into two separate ones in 2D, given by

$$H^1 \xrightarrow{\mathbf{grad}_\mathrm{t}} H^{\mathrm{curl}_\mathrm{t}} \xrightarrow{\mathrm{curl}_\mathrm{t}} L^2, \tag{2.37}$$

$$H^1 \xrightarrow{\mathbf{curl}_\mathrm{t}} H^{\mathrm{div}_\mathrm{t}} \xrightarrow{\mathrm{div}_\mathrm{t}} L^2. \tag{2.38}$$

As in the 3D case, both diagrams lead from a scalar field in H^1 to a scalar density field in L^2. The difference lies in the use of covariant vectors in $H^{\mathrm{curl}_\mathrm{t}}$ or contravariant vector densities in $H^{\mathrm{div}_\mathrm{t}}$. These two cases can be translated into each other by rotation via the 2D Levi–Civita tensor $\hat{\epsilon}_\mathrm{t}$ with contravariant density components given by

$$\epsilon_\mathrm{t}^{kl} = \begin{pmatrix} 0 & 1 \\ -1 & 0 \end{pmatrix}. \tag{2.39}$$

Relations between 2D differential operators can be written as

$$\mathbf{curl}_\mathrm{t}\, U = \hat{\epsilon}_\mathrm{t}\, \mathbf{grad}_\mathrm{t}\, U, \tag{2.40}$$

$$\mathrm{curl}_\mathrm{t}\, \boldsymbol{u} = \mathrm{div}_\mathrm{t}(\hat{\epsilon}_\mathrm{t}\boldsymbol{u}). \tag{2.41}$$

With $\hat{\epsilon}_\mathrm{t}$, the cross product of vectors with covariant components U_k and V_k can be cast as

$$\boldsymbol{U} \times \boldsymbol{V} = (\boldsymbol{u}\hat{\epsilon}_\mathrm{t}\boldsymbol{v})\boldsymbol{e}_3 + V_3\hat{\epsilon}_\mathrm{t}\boldsymbol{u} - U_3\hat{\epsilon}_\mathrm{t}\boldsymbol{v}. \tag{2.42}$$

2.1.2 Covariant Formulation of Classical Electrodynamics

Using differential operators in the metric-free way stated above, Maxwell's equations act on density representations of fields listed in table 2.3. In SI units they are written as

$$\partial_k \mathcal{D}^k = \rho, \tag{2.43}$$

$$\epsilon^{ijk}\partial_j E_k = -\frac{\partial \mathcal{B}^i}{\partial t}, \tag{2.44}$$

$$\epsilon^{ijk}\partial_j H_k = \mathcal{J}^i + \frac{\partial \mathcal{D}^i}{\partial t}, \tag{2.45}$$

$$\partial_k \mathcal{B}^k = 0, \tag{2.46}$$

in any curvilinear coordinate system. To fulfill (2.44) and (2.46) automatically, E_k and $\mathcal{B}^k$ can be written in terms of a scalar potential Φ and a vector potential A_k with

$$E_k = -\partial_k \Phi - \frac{\partial A_k}{\partial t}, \qquad \mathcal{B}^k = \epsilon^{ijk}\partial_i A_j. \tag{2.47}$$

Ambiguities in these potentials can be fixed by transformation with a gauge potential χ,

$$\Phi \to \Phi - \frac{\partial \chi}{\partial t}, \qquad A_k \to A_k + \partial_k \chi. \tag{2.48}$$

Magnetostatic equations (2.25)–(2.26) are reproduced in the stationary limit of (2.45)–(2.46) with vanishing time derivatives. The constitutive relations linking excitations $\mathcal{D}^k, H_k$ to local linear responses $E_l, \mathcal{B}^l$ are

$$\mathcal{D}^k = \varepsilon^{kl} E_l, \tag{2.49}$$
$$H_k = \nu_{kl} \mathcal{B}^l, \tag{2.50}$$

with permittivity $\hat{\varepsilon}$ and reluctivity $\hat{\nu}$ respectively represented by contravariant $W = +1$ density and covariant $W = -1$ density components,

$$\varepsilon^{kl} = \sqrt{g} \boldsymbol{e}^k \cdot \hat{\varepsilon} \boldsymbol{e}^l, \tag{2.51}$$
$$\nu_{kl} = \sqrt{g}^{-1} \boldsymbol{e}_k \cdot \hat{\nu} \boldsymbol{e}_l. \tag{2.52}$$

While the field equations (2.43)–(2.46) remain independent of coordinates, (2.49)–(2.50) contain all influence from the metric tensor $\hat{g}$ implicitly via the basis vectors and the Jacobian in (2.51)–(2.52). In particular for a scalar ν, components of $\hat{g}$ enter the resulting covariant density representation of $\hat{\nu}$ in curvilinear coordinates,

$$\nu_{kl} = \frac{1}{\sqrt{g}} \sum_{i,j} \partial_k r^i \partial_l r^j \nu \delta_{ij} = \frac{g_{kl}}{\sqrt{g}} \nu. \tag{2.53}$$

This means that covariant reluctivity components generated by a scalar ν inherit their symmetry properties from g_{kl}. If physical components of the permeability tensor are already given in the desired coordinate frame as a matrix $[\mu_{(kl)}]$, covariant density components of $\hat{\nu}$ can be found by taking its inverse $[\nu_{(kl)}] = [\mu_{(kl)}]^{-1}$ and computing

$$\nu_{kl} = \frac{\sqrt{g_{kk} g_{ll}}}{\sqrt{g}} \nu_{(kl)}. \tag{2.54}$$

One can see that if ν_{kl} are constant in certain curvilinear coordinates, physical components $\nu_{(kl)}$ will usually vary locally and vice versa. One should remark that the solution for *covariant* components H_k in curvilinear geometry with *constant* physical $\nu_{(kl)}$ is identical to the one for *Cartesian* components of $\boldsymbol{H}$ with a spatially *varying* $\nu_{(kl)}$. Thus one could emulate curvilinear geometry for magnetostatics in flat geometry by a material with locally varying permeability, and vice versa.

Table 2.3: Conventions to represent electromagnetic scalar, vector and tensor fields by densities of varying weight.

Quantity	Symbol	Type	Weight
metric tensor	g_{kl}	covariant	0
inverse metric	g^{kl}	contravariant	0
Jacobian	$\sqrt{g}$	scalar	+1
Levi–Civita tensor	ϵ^{ijk}	contravariant	+1
charge density	ρ	scalar	+1
current density	$\mathcal{J}^k$	contravariant	+1
electric field	E_k	covariant	0
magnetic flux density	$\mathcal{B}^k$	contravariant	+1
electric displacement	$\mathcal{D}^k$	contravariant	+1
magnetic field intensity	H_k	covariant	0
scalar potential	Φ	scalar	0
vector potential	A_k	covariant	0
gauge potential	χ	scalar	0
magnetic surface charge density	σ_{m}	scalar	+1
surface current density	$\mathcal{K}^k$	contravariant	+1
permittivity	ε^{kl}	contravariant	+1
permeabiliy	μ^{kl}	contravariant	+1
reluctivity	ν_{kl}	covariant	−1
longitudinal reluctivity	ν_{33}	scalar	−1
transverse reluctivity	$\nu_{\mathrm{t},kl}$	covariant	−1
modified transverse reluctivity	$\bar{\nu}_{\mathrm{t}}^{kl}$	contravariant	+1
transverse Levi–Civita tensor	$\epsilon_{\mathrm{t}}^{kl}$	contravariant	+1

2.1.3 Reduction of Magnetostatics to 2D by Fourier Expansion

To reduce the 3D problem of (2.28) to a number of 2D equations we write quantities assumed to be 2π-periodic in x^3 as a Fourier series

$$f(x^1, x^2, x^3) = \sum_{n=-\infty}^{\infty} f_n(x^1, x^2)\, e^{\mathrm{i}nx^3}, \tag{2.55}$$

where i is the imaginary unit. With this convention, the forward transform reads

$$f_n(x^1, x^2) = \frac{1}{2\pi} \int_0^{2\pi} f(x^1, x^2, x^3)\, e^{-\mathrm{i}nx^3}\, \mathrm{d}x^3. \tag{2.56}$$

These transforms are not applied to whole vector fields, as a reader familiar with the reciprocal space of crystallography might assume. Instead, dual vector bases are used for the covariant formalism, and the Fourier transform is applied only on one out of three coordinates here. Only the component functions are expanded as Fourier series, all with the same n. To be compatible with the respective equations, the actual representation is taken as in table 2.3 for each quantity. For example, for contravariant vector field density components we write

$$\boldsymbol{F} = \mathcal{F}^k(x^1, x^2, x^3)\boldsymbol{e}_k = \left(\sum_{n=-\infty}^{\infty} \mathcal{F}_n^k(x^1, x^2)\, e^{\mathrm{i}nx^3} \right) \boldsymbol{e}_k = \sum_{n=-\infty}^{\infty} \boldsymbol{F}_n\, e^{\mathrm{i}nx^3}, \tag{2.57}$$

where an implicit sum is taken over k.

The Fourier basis $\exp(\mathrm{i}nx^3)$ is orthogonal, so the following equations have to hold for each harmonic individually, as long as no mode-coupling occurs. Thus we omit n as an index in the notation and use $\bar{f} \equiv f_{n=0}$ for non-oscillatory and $\tilde{f} \equiv f_{n\neq 0}$ for oscillatory harmonics. This allows for compact notation when transforming 3D differential operators to 2D differential operators:

$$\mathbf{grad}\, U \to \mathbf{grad}_\mathrm{t}\, U + \mathrm{i}n\tilde{U}\boldsymbol{e}^3, \tag{2.58}$$

$$\operatorname{div} \boldsymbol{U} \to \operatorname{div}_\mathrm{t} \boldsymbol{u} + \mathrm{i}n\tilde{\mathcal{U}}^3, \tag{2.59}$$

$$\mathbf{curl}\, \boldsymbol{U} \to \boldsymbol{e}_3 \operatorname{curl}_\mathrm{t} \boldsymbol{u} + \mathbf{curl}_\mathrm{t}\, U_3 - \mathrm{i}n\hat{\epsilon}_\mathrm{t}\tilde{\boldsymbol{u}}. \tag{2.60}$$

Applying (2.58) to (2.48), we see that $\bar{A}_3$ is not affected by any gauge, but we can set $\tilde{A}_3 = 0$ by using the gauge potential

$$\tilde{\chi} = \frac{\mathrm{i}}{n}\tilde{A}_3. \tag{2.61}$$

Independent gauging in this manner is possible for each $n \neq 0$. Due to the superposition principle, we can use a fully transverse vector potential with a different gauge for each individual harmonic and take a Fourier sum in the end. Contravariant magnetic flux density components follow as

$$\tilde{\mathcal{B}}^3 = \operatorname{curl}_\mathrm{t} \tilde{\boldsymbol{a}}, \qquad \tilde{\boldsymbol{b}} = -\mathrm{i}n\hat{\epsilon}_\mathrm{t}\tilde{\boldsymbol{a}}, \tag{2.62}$$

$$\bar{\mathcal{B}}^3 = \operatorname{curl}_\mathrm{t} \bar{\boldsymbol{a}}, \qquad \bar{\boldsymbol{b}} = \mathbf{curl}_\mathrm{t}\, \bar{A}_3. \tag{2.63}$$

Thus, the original problem splits into three separate cases, classified by components of $\boldsymbol{A}$: $\tilde{\boldsymbol{a}}$ (transverse $n \neq 0$), $\bar{\boldsymbol{a}}$ (transverse $n = 0$), and $\bar{A}_3$ (longitudinal $n = 0$).

To retain linearity of terms involving x^3 and thus avoid mode-coupling via convolution in the constitutive relation (2.50), we require covariant $W = -1$ density components $\nu_{kl} = \nu_{kl}(x^1, x^2)$ of the reluctivity tensor $\hat{\nu}$ to be independent of the symmetry coordinate x^3 to allow arbitrary harmonics n for the fields. In addition, to be able to split transverse and longitudinal components of fields later, off-diagonal components in x^3 shall vanish. This

means that

$$\nu_{kl} = \begin{pmatrix} & & 0 \\ & \nu_{\mathrm{t},kl} & 0 \\ 0 & 0 & \nu_{33} \end{pmatrix}, \tag{2.64}$$

with transverse reluctivity

$$\nu_{\mathrm{t},kl} = \begin{pmatrix} \nu_{11} & \nu_{12} \\ \nu_{21} & \nu_{22} \end{pmatrix} \tag{2.65}$$

as a covariant $W = -1$ density and longitudinal reluctivity ν_{33} as a scalar $W = -1$ density. In the case of a scalar permeability, those symmetry restrictions thus apply to the metric tensor and vice versa, so $\sqrt{g}^{-1} g_{kl}$ shall be independent of x^3 and $g_{k3} = g_{3k} = 0$ for $k \neq 3$. A modified[1] transverse reluctivity

$$\hat{\bar{\nu}}_\mathrm{t} = -\hat{\epsilon}_\mathrm{t} \hat{\nu}_\mathrm{t} \hat{\epsilon}_\mathrm{t} \tag{2.66}$$

is useful to introduce, with contravariant density components

$$\bar{\nu}_\mathrm{t}^{kl} = \begin{pmatrix} \nu_{22} & -\nu_{21} \\ -\nu_{12} & \nu_{11} \end{pmatrix} \tag{2.67}$$

proportional to the inverse of (2.65). For scalar ν and g_{kl} of the form (2.64) this reduces to

$$\bar{\nu}_\mathrm{t}^{kl} = \frac{\sqrt{g}\, g_\mathrm{t}^{kl}}{g_{33}} \nu, \tag{2.68}$$

where g_t^{kl} is the transverse part of the (symmetric) inverse metric tensor.[2]

Under the given restrictions, Ampère's law in the form of (2.28) splits into transverse and longitudinal parts. For all n, the transverse part is given by

$$\mathbf{curl}_\mathrm{t} \left(\nu_{33} \operatorname{curl}_\mathrm{t} \boldsymbol{a} \right) + n^2 \hat{\bar{\nu}}_\mathrm{t} \boldsymbol{a} = \boldsymbol{j}. \tag{2.69}$$

As opposed to the singular ungauged three-dimensional curl-curl equation (2.28), the additional term resulting from the fixed gauge makes (2.69) uniquely solvable for $n \neq 0$, analogous to the 3D curl-curl equation with a time-harmonic term. Like in the scalar Helmholtz equation $-\Delta \Phi + n^2 \Phi = \varrho$ arising from Fourier expansion of the Poisson equation in electrostatics, a positive definite $\hat{\bar{\nu}}_\mathrm{t}$ weighted by n^2 leads to decaying solutions, opposed to oscillating solutions which would typically result from the Fourier expansion of a wave equation in time.

For $n = 0$, the longitudinal part reads

$$\operatorname{curl}_\mathrm{t} (\hat{\nu}_\mathrm{t} \mathbf{curl}_\mathrm{t} \bar{A}_3) = \bar{\mathcal{J}}^3. \tag{2.70}$$

[1] The bar does not refer to the Fourier series coefficient with $n = 0$ here, but since we required tensor components to be independent of x^3, the notation is unambiguous.

[2] If instead the inverse of the transverse part of $\hat{g}$ were used, the result would be identical, e.g. for cylindrical coordinates $\bar{\nu}_\mathrm{t}^{ZZ} = \bar{\nu}_\mathrm{t}^{RR} = \nu / R$. This inverted dependency on R compared to the usual Laplacian Δ in cylindrical coordinates is characteristic for the Grad–Shafranov operator $\Delta^\star$ (see [5]).

Using the relations between 2D differential operators in (2.40)–(2.41) together with the modified transverse reluctivity $\hat{\bar{\nu}}_\mathrm{t}$ of (2.66), we can rewrite (2.70) as a Poisson equation

$$-\operatorname{div}_\mathrm{t}(\hat{\bar{\nu}}_\mathrm{t}\,\mathbf{grad}_\mathrm{t}\,\bar{A}_3) = \bar{\mathcal{J}}^3. \tag{2.71}$$

The longitudinal part for $n \neq 0$,

$$\mathrm{i}n\operatorname{div}_\mathrm{t}(\hat{\tilde{\nu}}_\mathrm{t}\tilde{\boldsymbol{a}}) = \tilde{\mathcal{J}}^3 \tag{2.72}$$

is automatically fulfilled via the divergence relation for Fourier harmonics

$$\operatorname{div}_\mathrm{t}\boldsymbol{j} + \mathrm{i}n\mathcal{J}^3 = 0, \tag{2.73}$$

which can be seen from applying $\operatorname{div}_\mathrm{t}$ to (2.69). Thus the longitudinal case has to be solved only for $n = 0$.

All equations are now given in coordinate space (x^1, x^2) on a cross-section perpendicular to the symmetry direction x^3 of the original domain Ω. The coordinate-independent formulation uses integrals of densities with the volume element $\mathrm{d}x^1\,\mathrm{d}x^2$ in the 2D coordinate domain Ω_t and line element

$$\mathrm{d}\ell = \sqrt{(\mathrm{d}x^1)^2 + (\mathrm{d}x^2)^2} \tag{2.74}$$

on the boundary Γ_t in coordinate space.

2.1.4 Boundary Conditions

Well-posed boundary value problems for (2.28) in $\boldsymbol{A}$ include Dirichlet, Neumann, or Robin boundary conditions. Since Robin boundary conditions are just weighted sums of Dirichlet and Neumann boundary conditions, they are not treated specifically here.

For a Dirichlet boundary condition, the magnetic flux density component perpendicular to the surface is given by

$$\boldsymbol{B}\cdot\boldsymbol{N} = \mathcal{B}^k N_k = \sigma_\mathrm{m}, \tag{2.75}$$

where $\boldsymbol{N}$ is the outward unit normal vector on the boundary Γ, and σ_m is a magnetic surface charge density (perpendicular component of the induction) with weight $W = +1$. Integration over the boundary Γ yields the magnetic flux Ψ through the boundary Γ, which is zero for a closed boundary.

Inserting (2.62)–(2.63) into (2.75) and separating the case $n = 0$ from $n \neq 0$ yields

$$\tilde{\sigma}_\mathrm{m} = N_3\operatorname{curl}_\mathrm{t}\tilde{\boldsymbol{a}} - \mathrm{i}n\boldsymbol{n}\hat{\epsilon}_\mathrm{t}\tilde{\boldsymbol{a}}, \tag{2.76}$$

$$\bar{\sigma}_\mathrm{m} = N_3\operatorname{curl}_\mathrm{t}\bar{\boldsymbol{a}} + \boldsymbol{n}\cdot\mathbf{curl}_\mathrm{t}\,\bar{A}_3. \tag{2.77}$$

Due to the symmetry imposed, $N_3 = 0$ and the Dirichlet boundary condition for the case $n \neq 0$ can be written as

$$\tilde{\boldsymbol{a}}\hat{\epsilon}_\mathrm{t}\boldsymbol{n} = -\frac{\mathrm{i}}{n}\tilde{\sigma}_\mathrm{m}. \tag{2.78}$$

For $n = 0$, no restrictions for $\bar{\boldsymbol{a}}$ can be imposed via (2.77), so we are free to set

$$\bar{\boldsymbol{a}}\hat{\epsilon}_{\mathrm{t}}\boldsymbol{n} = 0. \tag{2.79}$$

Rewriting the remaining term of (2.77) results in,

$$\bar{\sigma}_{\mathrm{m}} = -\hat{\epsilon}_{\mathrm{t}}\boldsymbol{n} \cdot \mathbf{grad}_{\mathrm{t}}\, \bar{A}_3, \tag{2.80}$$

where the right-hand side is the directional derivative along the tangent of the boundary Γ_{t}. Integration along a line element $\mathrm{d}\ell$ of Γ_{t} yields

$$\bar{A}_3 = -\int_{\Gamma_{\mathrm{t}}} \bar{\sigma}_{\mathrm{m}}\, \mathrm{d}\ell, \tag{2.81}$$

where the direction of integration is given by the direction of $\hat{\epsilon}_{\mathrm{t}}\boldsymbol{n}$. We require all Dirichlet boundaries to be connected in order to share the same integration constant in (2.81). This problem is discussed further in section 5.1.1.

For a Neumann boundary condition, the magnetic field components parallel to the surface are given by

$$\boldsymbol{H} \times \boldsymbol{N} = \boldsymbol{K} \Leftrightarrow \epsilon^{ijk} H_i N_j = \mathcal{K}^k, \tag{2.82}$$

where $\boldsymbol{K}$ is a surface current density. Taking an inner product with $\boldsymbol{N}$, we get the condition $\boldsymbol{K} \cdot \boldsymbol{N} = 0$, leaving only two components of $\boldsymbol{K}$ to be chosen independently for any given $\boldsymbol{N}$. Neumann boundary conditions are subject to compatibility conditions,

$$\oint_{\Gamma} \boldsymbol{K}\, \mathrm{d}\Gamma = -\int_{\Omega} \boldsymbol{J}\, \mathrm{d}\Omega, \tag{2.83}$$

on a closed surface Γ, and

$$\operatorname{div} \boldsymbol{K} = \boldsymbol{J} \cdot \boldsymbol{N}, \tag{2.84}$$

on every point of the boundary Γ. Integration of the latter yields the current I flowing through the boundary Γ.

Inserting all pertaining definitions into (2.82) and splitting components gives

$$\tilde{\boldsymbol{k}} = -\nu_{33}(\operatorname{curl}_{\mathrm{t}} \tilde{\boldsymbol{a}})\hat{\epsilon}_{\mathrm{t}}\boldsymbol{n} + \mathrm{i}nN_3\hat{\bar{\nu}}_{\mathrm{t}}\tilde{\boldsymbol{a}}, \tag{2.85}$$

$$\bar{\boldsymbol{k}} = -\nu_{33}(\operatorname{curl}_{\mathrm{t}} \bar{\boldsymbol{a}})\hat{\epsilon}_{\mathrm{t}}\boldsymbol{n} - N_3\hat{\bar{\nu}}_{\mathrm{t}}\, \mathbf{grad}_{\mathrm{t}}\, \bar{A}_3, \tag{2.86}$$

$$\tilde{\mathcal{K}}^3 = -\mathrm{i}n\boldsymbol{n}\hat{\bar{\nu}}_{\mathrm{t}}\tilde{\boldsymbol{a}}, \tag{2.87}$$

$$\bar{\mathcal{K}}^3 = \boldsymbol{n}\hat{\bar{\nu}}_{\mathrm{t}}\, \mathbf{grad}_{\mathrm{t}}\, \bar{A}_3. \tag{2.88}$$

Since $N_3 = 0$, the transverse equations (2.85) and (2.86) reduce to a single equation valid for all n,

$$\nu_{33}(\operatorname{curl}_{\mathrm{t}} \boldsymbol{a})\hat{\epsilon}_{\mathrm{t}}\boldsymbol{n} = -\boldsymbol{k}. \tag{2.89}$$

Equation (2.87) is automatically fulfilled by prescribing (2.85), as can be seen by inserting both equations into $\boldsymbol{k} \cdot \boldsymbol{n} + \mathcal{K}^3 N_3 = 0$, which holds even without $N_3 = 0$. Finally, (2.88) can be used for the longitudinal case with $n = 0$ as is.

2.1.5 Variational Formulation in Coordinate Space

To find a variational formulation for numerical computations, (2.71) and (2.69) are multiplied by a test function and integrated with weight $\sqrt{g}$ in coordinate space (x^1, x^2). Volume integration of quantities $F(x^1, x^2)$ over Ω and dividing the result by the range 2π of x^3 results in an integral over the 2D coordinate domain Ω_t of the density representation $\mathcal{F} = \sqrt{g}F$,

$$\frac{1}{2\pi}\int_\Omega F(x^1,x^2)\ \mathrm{d}\Omega = \frac{1}{2\pi}\int_0^{2\pi}\mathrm{d}x^3\int_{\Omega_\mathrm{t}}\mathcal{F}(x^1,x^2)\ \mathrm{d}x^1\,\mathrm{d}x^2 = \int_{\Omega_\mathrm{t}}\mathcal{F}(x^1,x^2)\ \mathrm{d}x^1\,\mathrm{d}x^2. \tag{2.90}$$

The variational form of the longitudinal equation (2.71) for $n = 0$ with scalar test function $w(x^1, x^2)$ is

$$\int_{\Omega_\mathrm{t}}(\partial_k w)\bar{\nu}_\mathrm{t}^{kl}(\partial_l \bar{A}_3)\ \mathrm{d}x^1\,\mathrm{d}x^2 - \int_{\Gamma_\mathrm{t}} w\bar{\mathcal{K}}^3\ \mathrm{d}\ell = \int_{\Omega_\mathrm{t}} w\bar{\mathcal{J}}^3\ \mathrm{d}x^1\,\mathrm{d}x^2. \tag{2.91}$$

Here $\boldsymbol{n} = (N_1, N_2)$ is the unit outward normal vector across the boundary line Γ_t in coordinate space (x^1, x^2) and the implied sums are taken over k, l from 1 to 2. The reduced Neumann boundary condition is the natural boundary condition for this weak form. For the special case $w = 1$ the compatibility condition (2.83) in the transverse plane follows as

$$-\int_{\Gamma_\mathrm{t}}\bar{\mathcal{K}}^3\ \mathrm{d}\ell = \int_{\Omega_\mathrm{t}}\bar{\mathcal{J}}^3\ \mathrm{d}x^1\,\mathrm{d}x^2, \tag{2.92}$$

fixing the Neumann term in (2.91) corresponding to the magnetic field parallel to the transverse boundary to the total current through the surface $x^3 = \text{const.}$ within the domain.

For the transverse equation (2.69) for $n = 0$ as well as $n \neq 0$, with vectorial test function $\boldsymbol{w}$ with covariant components W_k, we obtain

$$\int_{\Omega_\mathrm{t}}\mathrm{curl}_\mathrm{t}\,\boldsymbol{w}\,\nu_{33}\,\mathrm{curl}_\mathrm{t}\,\boldsymbol{a}\ \mathrm{d}x^1\,\mathrm{d}x^2 + n^2\int_{\Omega_\mathrm{t}} W_k\bar{\nu}_\mathrm{t}^{kl}A_l\ \mathrm{d}x^1\,\mathrm{d}x^2 - \int_{\Gamma_\mathrm{t}} W_k\mathcal{K}^k\ \mathrm{d}\ell = \int_{\Omega_\mathrm{t}} W_k\mathcal{J}^k\ \mathrm{d}x^1\,\mathrm{d}x^2. \tag{2.93}$$

The resulting linear system is singular for $n = 0$ and either needs an iterative solver, or an ad-hoc regularization where n^2 is set to a value small enough in order not to perturb the solution, but large enough (compared to machine precision) in order to make the resulting stiffness matrix non-singular.

The longitudinal $n = 0$ Poisson problem (2.91) can be treated via standard (Lagrange)

finite elements for the scalar function $\bar{A}_3$ as well as the test function w. For the general transverse variational problem (2.93), the natural discretization for $\boldsymbol{a}$ are 2D (Nédélec) edge elements conforming to $H^{\mathbf{curl}_\mathrm{t}}(\Omega_\mathrm{t})$. Due to its fixed divergence in (2.70), components $\mathcal{J}^k$ of the transverse current density $\boldsymbol{j}$ should be discretized by 2D (Raviart–Thomas) elements conforming to $H^{\mathrm{div}_\mathrm{t}}(\Omega_\mathrm{t})$.

Since $\operatorname{div} \boldsymbol{J} = 0$, it may also be written as $\boldsymbol{J} = \mathbf{curl}\, \boldsymbol{T}$. Here, $\boldsymbol{T}$ is an analogue to the vector potential $\boldsymbol{A}$ in (2.61) and similar considerations apply. Fourier decomposition then yields

$$\tilde{\mathcal{J}}^3 = \operatorname{curl}_\mathrm{t} \tilde{\boldsymbol{t}}, \qquad \tilde{\boldsymbol{j}} = -\mathrm{i}n\hat{\epsilon}_\mathrm{t}\tilde{\boldsymbol{t}}, \tag{2.94}$$

$$\bar{\mathcal{J}}^3 = \operatorname{curl}_\mathrm{t} \bar{\boldsymbol{t}}, \qquad \bar{\boldsymbol{j}} = \mathbf{curl}_\mathrm{t}\, \bar{T}_3. \tag{2.95}$$

From (2.94) it also follows that $\operatorname{div}_\mathrm{t} \tilde{\boldsymbol{j}} = -\mathrm{i}n \operatorname{curl}_\mathrm{t} \tilde{\boldsymbol{t}}$ and so it is apparent that $\boldsymbol{t}$ can be discretized by 2D Nédélec elements, which can be interpreted as an orthogonal rotation of Raviart–Thomas Elements. This makes implementation of (2.93) convenient since all appearing vector fields can be represented by the same type of finite element.

2.1.6 Cartesian, Cylindrical and Spherical Coordinates

For the simplest case of scalar reluctivity ν, we shall list the concrete tensor components according to (2.54) and (2.68) for the conceivably most common sets of coordinates.

In *Cartesian* coordinates

$$x^1 = X, \qquad x^2 = Y, \qquad x^3 = 2\pi\frac{Z}{Z_0}, \tag{2.96}$$

where Z_0 is the period of Z, we have the simple result

$$g_{11} = g_{22} = 1, \qquad g_{33} = \left(\frac{2\pi}{Z_0}\right)^2, \qquad \sqrt{g} = \frac{2\pi}{Z_0}, \tag{2.97}$$

$$\bar{\nu}_\mathrm{t}^{11} = \bar{\nu}_\mathrm{t}^{22} = \frac{Z_0}{2\pi}\nu, \qquad \nu_{33} = \frac{2\pi}{Z_0}\nu, \tag{2.98}$$

where only a constant factor is introduced to keep the notation of the Fourier series exponent consistent.

For *cylindrical* coordinates with symmetry in the azimuthal angle φ, we write a right-handed system (R, φ, Z) as

$$x^1 = Z, \qquad x^2 = R, \qquad x^3 = \varphi, \tag{2.99}$$

in order to keep our convention of assigning the symmetry direction to the third coordinate.

This results in the following metric and reluctivity components:

$$g_{11} = g_{22} = 1, \qquad g_{33} = R^2, \qquad \sqrt{g} = R, \tag{2.100}$$

$$\bar{\nu}_{\mathrm{t}}^{11} = \bar{\nu}_{\mathrm{t}}^{22} = \frac{\nu}{R}, \qquad \nu_{33} = R\nu. \tag{2.101}$$

Spherical coordinates with azimuthal angle φ and inclination angle θ, i.e. with the following conversion to Cartesian coordinates,

$$X = r\sin\theta\cos\varphi, \qquad Y = r\sin\theta\sin\varphi, \qquad Z = r\cos\theta, \tag{2.102}$$

constitute a right-handed system with the ordering

$$x^1 = r, \qquad x^2 = \theta, \qquad x^3 = \varphi. \tag{2.103}$$

This yields the metric components

$$g_{11} = 1, \qquad g_{22} = r^2, \qquad g_{33} = r^2\sin^2\theta, \tag{2.104}$$

Jacobian

$$\sqrt{g} = r^2\sin\theta, \tag{2.105}$$

and reluctivity

$$\bar{\nu}_{\mathrm{t}}^{11} = \frac{\nu}{\sin\theta}, \qquad \bar{\nu}_{\mathrm{t}}^{22} = \frac{\nu}{r^2\sin\theta}, \qquad \nu_{33} = \nu\sin\theta. \tag{2.106}$$

Note that the underlying symmetry is still cylindrical and not spherical since the Fourier transform is taken along the same azimuthal angle in both cases. The distinguishing feature concerns the transverse part of the problem: planes of constant φ are spanned by quasi-polar coordinates (r, θ) instead of quasi-Cartesian coordinates (R, Z). Taking spherical symmetry into account would reduce the problem to one dimension in r, thus rendering the finite element method unnecessary, and require expansion in spherical harmonics instead of Fourier series, which is outside the scope of this work.

Cylindrical, spherical and related coordinates contain singularities near axis positions and poles. In the present work this problem is treated in an ad-hoc way. In case the computational domain contains such a singularity, we impose a homogeneous Neumann condition for transverse cases with $n = 0$, and a homogeneous Dirichlet condition for all other cases, both at a small distance from the actual singular boundary. To avoid division by zero at $R = 0$, it was found to be sufficient to move the boundary of the computational domain (extending up to $R = 1$) to $R = 10^{-31}$, without any visible impact on the solution. In the future we expect this problem to be solved in a general manner by imposing uniqueness and regularity in the limiting case directly at the boundary, or by coupling to an analytical or numerical solution in an interior domain with different coordinates [10].

2.2 Plasma Response Current

In this section, we derive the plasma response current for a purely ideal MHD model and a hybrid MHD/kinetic model, thus realizing the operator $\hat{P}$ in (2.2).

Neglecting time derivatives and flow velocity, the ideal MHD force balance equation for the axisymmetric equilibrium is given by

$$c\nabla p_0 = \boldsymbol{J}_0 \times \boldsymbol{B}_0. \tag{2.107}$$

Applying non-axysymmetric perturbations to all terms, we get

$$c\nabla \left(p_0 + \delta p\right) = \left(\boldsymbol{J}_0 + \delta \boldsymbol{J}\right) \times \left(\boldsymbol{B}_0 + \delta \boldsymbol{B}\right). \tag{2.108}$$

We then linearize by neglecting terms of order $O(\delta^2)$, and subtract (2.107) to arrive at

$$c\nabla \delta p = \delta \boldsymbol{J} \times \boldsymbol{B}_0 + \boldsymbol{J}_0 \times \delta \boldsymbol{B}. \tag{2.109}$$

The scalar product of this linearized force balance equation with $\boldsymbol{B}_0$ yields the *magnetic differential equation* (MDE), a first-order partial differential equation, for the pressure perturbation,

$$c\boldsymbol{B}_0 \cdot \nabla \delta p = \left(\boldsymbol{B}_0 \times \boldsymbol{J}_0\right) \cdot \delta \boldsymbol{B} \overset{(2.107)}{=} -c\nabla p_0 \cdot \delta \boldsymbol{B} = -cp_0'(\psi)\delta B^{\psi}. \tag{2.110}$$

Since $B_0^{\psi} = 0$, the MDE decouples in radial direction and is reduced to two dimensions with periodic boundary conditions in φ and ϑ,

$$\left(B_0^{\vartheta}\partial_{\vartheta} + B_0^{\varphi}\partial_{\varphi}\right)\delta p = -p_0'(\psi)\delta B^{\psi}, \tag{2.111}$$

which can be solved on each magnetic flux surface cross-section independently. The Fourier transform in the toroidal angle further reduces this to a first-order ordinary differential equation with periodic boundary conditions in ϑ,

$$\left(B_0^{\vartheta}\partial_{\vartheta} + \mathrm{i}nB_0^{\varphi}\right)p_n = -p_0'(\psi)B_n^{\psi}. \tag{2.112}$$

If we use cylindrical coordinates with physical components instead, the result is

$$\left(\boldsymbol{B}_0^{\mathrm{pol}} \cdot \nabla_{\mathrm{pol}} + \frac{\mathrm{i}n}{R}B_0^{\mathrm{tor}}\right)p_n = -p_0'(\psi)B_n^{\psi}, \tag{2.113}$$

which we solve with a first-order finite difference scheme as described in section 4.5, although a solution via a least-squares Galerkin method is feasible as well [11, 12]. In either case, solving the MDE yields the pressure perturbation, given the equilibrium quantities and the magnetic field perturbation, which leaves only the current perturbation unknown.

Due to the cross product in (2.109), $\delta \boldsymbol{J}$ is determined up to a component parallel to $\boldsymbol{B}_0$, the

Pfirsch-Schlüter current perturbation. To isolate the perpendicular components, the *diamagnetic current* perturbation, we take another cross product with a vector parallel to $\boldsymbol{B}_0$ and simplify:

$$\begin{aligned}\frac{\boldsymbol{h}}{B_0} \times c\nabla\delta p &= \frac{\boldsymbol{h}}{B_0} \times (\delta\boldsymbol{J} \times \boldsymbol{B}_0 + \boldsymbol{J}_0 \times \delta\boldsymbol{B}) \\ &= (\boldsymbol{h}\cdot\boldsymbol{h})\delta\boldsymbol{J} - (\delta\boldsymbol{J}\cdot\boldsymbol{h})\boldsymbol{h} + \frac{\delta\boldsymbol{B}\cdot\boldsymbol{h}}{B_0}\boldsymbol{J}_0 - \frac{\boldsymbol{J}_0\cdot\boldsymbol{h}}{B_0}\delta\boldsymbol{B} \\ &= \delta\boldsymbol{J}^\perp + \frac{\delta B^\parallel}{B_0}\boldsymbol{J}_0 - \frac{J_0^\parallel}{B_0}\delta\boldsymbol{B}. \end{aligned} \tag{2.114}$$

Considering only the parallel component of the last equation, we get

$$\frac{\delta B^\parallel}{B_0}J_0^\parallel - \frac{J_0^\parallel}{B_0}\delta B^\parallel = 0 \tag{2.115}$$

which is trivially true. The remaining perpendicular components yield

$$\delta\boldsymbol{J}^\perp = \frac{c}{B_0}\boldsymbol{h}\times\nabla\delta p + \frac{J_0^\parallel}{B_0}\delta\boldsymbol{B}^\perp - \frac{\delta B^\parallel}{B_0}\boldsymbol{J}_0^\perp = \tag{2.116}$$

$$= \frac{c}{B_0}\boldsymbol{h}\times\nabla\delta p + \frac{J_0^\parallel}{B_0}\delta\boldsymbol{B} - \cancel{\frac{J_0^\parallel}{B_0}\delta B^\parallel\boldsymbol{h}} - \frac{\delta B^\parallel}{B_0}\boldsymbol{J}_0 + \cancel{\frac{\delta B^\parallel}{B_0}J_0^\parallel\boldsymbol{h}} = \tag{2.117}$$

$$= \frac{1}{B_0^2}\Big(c\boldsymbol{B}_0\times\nabla\delta p + (\boldsymbol{J}_0\cdot\boldsymbol{B}_0)\,\delta\boldsymbol{B} - (\delta\boldsymbol{B}\cdot\boldsymbol{B}_0)\,\boldsymbol{J}_0\Big) \tag{2.118}$$

With the perpendicular components fixed, the remaining parallel component can be determined from the condition of zero divergence:

$$\nabla\cdot\left(\delta J^\parallel\boldsymbol{h}\right) + \nabla\cdot\delta\boldsymbol{J}^\perp = 0 \tag{2.119}$$

$$\boldsymbol{B}_0\cdot\nabla\frac{\delta J^\parallel}{B_0} = -\nabla\cdot\delta\boldsymbol{J}^\perp \tag{2.120}$$

The latter equation again takes the form of an MDE, for which we compute the divergence of the perpendicular components on the right-hand side analytically:

$$\begin{aligned}\nabla\cdot\delta\boldsymbol{J}^\perp &= \Big(c\boldsymbol{B}_0\times\nabla\delta p + (\boldsymbol{J}_0\cdot\boldsymbol{B}_0)\,\delta\boldsymbol{B} - (\delta\boldsymbol{B}\cdot\boldsymbol{B}_0)\,\boldsymbol{J}_0\Big)\cdot\nabla\frac{1}{B_0^2} + \\ &\quad + \frac{1}{B_0^2}\nabla\cdot\Big(c\boldsymbol{B}_0\times\nabla\delta p + (\boldsymbol{J}_0\cdot\boldsymbol{B}_0)\,\delta\boldsymbol{B} - (\delta\boldsymbol{B}\cdot\boldsymbol{B}_0)\,\boldsymbol{J}_0\Big) = \\ &= B_0^2\delta\boldsymbol{J}^\perp\cdot\frac{-2}{B_0^3}\nabla B_0 + \frac{1}{B_0^2}\Big(c\nabla\cdot(\boldsymbol{B}_0\times\nabla\delta p) + \nabla\cdot\Big((\boldsymbol{J}_0\cdot\boldsymbol{B}_0)\,\delta\boldsymbol{B}\Big) - \nabla\cdot\Big((\delta\boldsymbol{B}\cdot\boldsymbol{B}_0)\,\boldsymbol{J}_0\Big)\Big) = \\ &= B_0^2\delta\boldsymbol{J}^\perp\cdot\frac{-1}{B_0^4}\nabla(\boldsymbol{B}_0\cdot\boldsymbol{B}_0) + \frac{1}{B_0^2}\Big(\cancel{c\boldsymbol{B}_0\cdot(\nabla\times\nabla\delta p)} - c\nabla\delta p\cdot(\nabla\times\boldsymbol{B}_0) + \\ &\quad + \delta\boldsymbol{B}\cdot\nabla(\boldsymbol{J}_0\cdot\boldsymbol{B}_0) + \cancel{(\boldsymbol{J}_0\cdot\boldsymbol{B}_0)\nabla\cdot\delta\boldsymbol{B}} - \boldsymbol{J}_0\cdot\nabla(\delta\boldsymbol{B}\cdot\boldsymbol{B}_0) - \cancel{(\delta\boldsymbol{B}\cdot\boldsymbol{B}_0)\nabla\cdot\boldsymbol{J}_0}\Big) = \end{aligned}$$

$$= \frac{1}{B_0^2}\left(-\delta \boldsymbol{J}^{\perp} \cdot \nabla \left(\boldsymbol{B}_0 \cdot \boldsymbol{B}_0\right) - 4\pi \boldsymbol{J}_0 \cdot \nabla \delta p + \delta \boldsymbol{B} \cdot \nabla \left(\boldsymbol{J}_0 \cdot \boldsymbol{B}_0\right) - \boldsymbol{J}_0 \cdot \nabla \left(\delta \boldsymbol{B} \cdot \boldsymbol{B}_0\right)\right) \tag{2.121}$$

Note that Ampère's law has been used in addition to vector calculus identities. The partial derivatives of the remaining simple scalar products are easily evaluated via the product rule. Fourier mode expansion of (2.120) and (2.121) yields

$$\left(\boldsymbol{B}_0^{\mathrm{pol}} \cdot \nabla_{\mathrm{pol}} + \frac{\mathrm{i}n}{R} B_0^{\mathrm{tor}}\right) \frac{J_n^{\parallel}}{B_0} = \frac{1}{B_0^2}\Big(\boldsymbol{J}_n^{\perp} \cdot \nabla_{\mathrm{pol}} \left(\boldsymbol{B}_0 \cdot \boldsymbol{B}_0\right) - \boldsymbol{B}_n \cdot \nabla_{\mathrm{pol}} \left(\boldsymbol{J}_0 \cdot \boldsymbol{B}_0\right) + \\ + \left(\boldsymbol{J}_0^{\mathrm{pol}} \cdot \nabla_{\mathrm{pol}} + \frac{\mathrm{i}n}{R} J_0^{\mathrm{tor}}\right) \left(4\pi p_n + \boldsymbol{B}_n \cdot \boldsymbol{B}_0\right)\Big), \tag{2.122}$$

which is an MDE and can be solved in the same manner as (2.113). This solution of (2.122) can be interpolated and combined with (2.118) to give the full $\boldsymbol{J}_n$:

$$\boldsymbol{J}_n = J_n^{\parallel} \boldsymbol{h} + \boldsymbol{J}_n^{\perp} = \frac{J_n^{\parallel}}{B_0} \boldsymbol{B}_0 + \frac{1}{B_0^2}\left(c \boldsymbol{B}_0 \times \left(\nabla_{\mathrm{pol}} p_n + \frac{\mathrm{i}n}{R} p_n \hat{\boldsymbol{e}}_{\mathrm{tor}}\right) + \left(\boldsymbol{J}_0 \cdot \boldsymbol{B}_0\right) \boldsymbol{B}_n - \left(\boldsymbol{B}_n \cdot \boldsymbol{B}_0\right) \boldsymbol{J}_0\right) \tag{2.123}$$

To summarize: with known equilibrium quantities, the magnetic field perturbation, and the pressure perturbation, the diamagnetic current perturbation and the Pfirsch-Schlüter current perturbation can be solved for.

We have not yet accounted for the δ distribution in the current density that iMHD predicts at resonance positions, or for the current density of finite value and extent that occurs in kinetic models instead. In the first case, the δ distribution can not be represented by the finite element bases covered in section 4.3, so we need to approximate it by a current density of finite value and width as well[1]. In section 2.2.1, we derive such an approximation in a slab model with the intent to roughly reproduce the ideal shielding provided by the δ distribution. Both this approach and the kinetic model used in chapter 3 yield a parallel current density, similar to the Pfirsch-Schlüter current, from which we need to reconstruct a *helical* current density, i.e., one for which the radial component vanishes. Thus our ansatz in symmetry flux coordinates $(\varrho, \varphi, \vartheta)$ is

$$\delta \boldsymbol{J} = \frac{\delta J^{\parallel}}{B_0} \boldsymbol{B}_0 + \delta C^{\perp} \boldsymbol{B}_0 \times \nabla \psi, \tag{2.124}$$

where $\delta C^{\perp} = \delta C^{\perp}(\varrho, \varphi, \vartheta)$ describes the contribution by the perpendicular part. Since no products of functions of φ appear, we can immediately rewrite our ansatz for toroidal Fourier

[1] Basis functions of XFEM (extended FEM) could include such a discontinuity, but that approach is beyond the scope of this thesis. Also, for the higher goal of treating the resonant current with a kinetic model, it is not necessary to accomodate such discontinuities.

modes:

$$\boldsymbol{J}_n = \frac{J_n^{\parallel}}{B_0}\boldsymbol{B}_0 + C_n^{\perp}\boldsymbol{B}_0 \times \nabla\psi. \tag{2.125}$$

With the other two components fixed, we can determine $\delta C^{\perp}$ from the condition of zero divergence, for which we need to calculate the contravariant density components:

$$\sqrt{g}J_n^k = \frac{J_n^{\parallel}}{B_0}\sqrt{g}B_0^k + C_n^{\perp}\varepsilon^{ijk}B_{0i}\partial_j\psi \rightarrow \tag{2.126}$$

$$\sqrt{g}J_n^{\varrho} = \frac{J_n^{\parallel}}{B_0}\sqrt{g}B_0^{\varrho} + C_n^{\perp}\varepsilon^{ij\varrho}B_{0i}\partial_j\psi = 0, \tag{2.127}$$

$$\sqrt{g}J_n^{\varphi} = \frac{J_n^{\parallel}}{B_0}\sqrt{g}B_0^{\varphi} + C_n^{\perp}\varepsilon^{ij\varphi}B_{0i}\partial_j\psi = \frac{J_n^{\parallel}}{B_0}q\sigma_{\psi'} + C_n^{\perp}B_{0\vartheta}\sigma_{\psi'}, \tag{2.128}$$

$$\sqrt{g}J_n^{\vartheta} = \frac{J_n^{\parallel}}{B_0}\sqrt{g}B_0^{\vartheta} + C_n^{\perp}\varepsilon^{ij\vartheta}B_{0i}\partial_j\psi = \frac{J_n^{\parallel}}{B_0}\sigma_{\psi'} - C_n^{\perp}B_{0\varphi}\sigma_{\psi'}. \tag{2.129}$$

Here we used $B_0^{\varrho} = 0$ and $\partial_j\psi = \delta_{j\varrho}\sigma_{\psi'}$ as well as (1.7) and (1.8). This yields the condition of zero divergence as

$$0 = \partial_k\left(\sqrt{g}J_n^k\right) = \mathrm{i}n\frac{J_n^{\parallel}}{B_0}q\sigma_{\psi'} + \mathrm{i}nC_n^{\perp}B_{0\vartheta}\sigma_{\psi'} + \frac{\partial}{\partial\vartheta}\frac{J_n^{\parallel}}{B_0}\sigma_{\psi'} - \frac{\partial}{\partial\vartheta}C_n^{\perp}B_{0\varphi}\sigma_{\psi'}. \tag{2.130}$$

Cancelling $\sigma_{\psi'}$ and rearranging yields an ODE in ϑ for $C_n^{\perp}$ with ψ fixed. Since $B_{0\vartheta}$ depends on ϑ, we cannot use a Fourier transform in ϑ without a convolution, but we can expand the parallel current as a Fourier series in ϑ instead:

$$\frac{\partial}{\partial\vartheta}C_n^{\perp} - \mathrm{i}n\frac{B_{0\vartheta}}{B_{0\varphi}}C_n^{\perp} = \frac{1}{B_{0\varphi}}\left(\mathrm{i}nq + \frac{\partial}{\partial\vartheta}\right)\frac{J_n^{\parallel}}{B_0} \tag{2.131}$$

$$= \frac{1}{B_{0\varphi}}\left(\mathrm{i}nq + \frac{\partial}{\partial\vartheta}\right)\sum_{m\in m_{\mathrm{res}}}\left(\frac{J_n^{\parallel}}{B_0}\right)_m \mathrm{e}^{\mathrm{i}m\vartheta} \tag{2.132}$$

$$= \sum_{m\in m_{\mathrm{res}}}\frac{\mathrm{i}(nq+m)}{B_{0\varphi}}\left(\frac{J_n^{\parallel}}{B_0}\right)_m \mathrm{e}^{\mathrm{i}m\vartheta}. \tag{2.133}$$

Note that only resonant poloidal modes are considered. Since (2.133) is of the same type as the MDE (2.112), except for the coefficients, we can solve it with the same finite difference scheme described in section 4.5. $C_n^{\perp}$ is then interpolated like in (4.34). Inserting (1.2) and (1.3) into (2.125) yields a convenient form for projection to finite elements according to (4.29) and (4.32),

$$\hat{J}_{nR} = \left(\frac{J_n^{\parallel}}{B_0} + C_n^{\perp}R\hat{B}_{0\varphi}\right)\hat{B}_{0R}, \tag{2.134}$$

$$\hat{J}_{nZ} = \left(\frac{J_n^{\parallel}}{B_0} + C_n^{\perp} R \hat{B}_{0\varphi} \right) \hat{B}_{0Z}, \tag{2.135}$$

$$\hat{J}_{n\varphi} = \frac{J_n^{\parallel}}{B_0} \hat{B}_{0\varphi} + C_n^{\perp} R \left(\hat{B}_{0R}^2 + \hat{B}_{0Z}^2 \right). \tag{2.136}$$

When adding this kind of current density, the Pfirsch-Schlüter current and the pressure perturbation should be damped near the resonance position. To this end, we modify the MDEs (2.113) and (2.122) on the left-hand side such that $n \to n + \mathrm{i}\varepsilon(\psi)$, where the damping is given as

$$\varepsilon(\psi) = \sum_{m \in m_{\mathrm{res}}} \frac{nq'(\psi)}{q(\psi)} \delta_{mn} \exp\left(-\frac{(\psi - \psi_{mn})^2}{\delta_{mn}^2} \right). \tag{2.137}$$

Here, ψ_{mn} is the resonance position and δ_{mn} is the width of the resonance layer in terms of ψ which is given by (45) in [13].

2.2.1 Ideal MHD Response Current

We consider a slab model where x stands in as the radial coordinate, y as the poloidal coordinate, and z as the toroidal coordinate. We place the magnetic axis at $x = -L$ and the plasma edge at $x = L$. We use Fourier series expansion in y and z and write

$$\boldsymbol{B}(\boldsymbol{r}) = \left(B^x(x)\hat{\boldsymbol{e}}_x + B^y(x)\hat{\boldsymbol{e}}_y + B^z(x)\hat{\boldsymbol{e}}_z \right) \mathrm{e}^{\mathrm{i}k_y y + \mathrm{i}k_z z}. \tag{2.138}$$

In the vector form we notate

$$\boldsymbol{k} = k_y \hat{\boldsymbol{e}}_y + k_z \hat{\boldsymbol{e}}_z. \tag{2.139}$$

Note that in this section, we omit the index $\boldsymbol{k}$ in the Fourier amplitudes to avoid cluttering the equations. Equilibrium quantities are explicitly introduced, such as the equilibrium magnetic field. It has flux surfaces $x = \text{const}$ so that its unit vector is

$$\boldsymbol{h}(x) = h^y(x)\hat{\boldsymbol{e}}_y + h^y(x)\hat{\boldsymbol{e}}_z. \tag{2.140}$$

We assume that the resonant surface is located at $x = x_{\mathrm{s}}$ such that $\boldsymbol{k} \cdot \boldsymbol{h}(x_{\mathrm{s}}) = 0$.

To reproduce shielding of the radial perturbation field at rational surfaces, we need to derive an expression for the paralell current density to be used with (2.125). We consider a vacuum with a shielding current $\boldsymbol{J}$ flowing within flux surfaces, i.e., it is helical and $J^x = 0$. The condition of zero divergence thus reduces to $\boldsymbol{k} \cdot \boldsymbol{J} = 0$. If this current were purely parallel, $\boldsymbol{J} = \boldsymbol{h} J_{\parallel}$, the condition of zero divergence is $\boldsymbol{k} \cdot \boldsymbol{h}(x) J_{\parallel} = 0$, which means that $J_{\parallel} = C_{\parallel} \delta(\boldsymbol{k} \cdot \boldsymbol{h})$ differs from zero only at the resonant surface. For the finite radial grid, the width of the

current must be finite. Therefore we model this shielding current as

$$\boldsymbol{J} = \boldsymbol{h} J_\mathrm{s} \, [\![-\Delta x < x < \Delta x]\!] \, \mathrm{e}^{\mathrm{i}k_y y + \mathrm{i}k_z z}. \tag{2.141}$$

Here J_s is a constant to be determined, the resonant point x_s is located in the interval $-\Delta x < x < \Delta x$, and the Iverson bracket $[\![\cdot]\!]$ yields one if the condition in the argument is true and zero otherwise. This means that we add (2.141) via (2.125) to (2.123) at the radial grid points surrounding the resonance position x_s, here modelled by $\pm\Delta x$.

Ampère's law and the condition of zero convergence reduce to

$$\mathrm{i}\left(k_y B^z - k_z B^y\right) = \frac{4\pi}{c} J^x = 0, \tag{2.142}$$

$$\mathrm{i}k_z B^x - \frac{\partial B^z}{\partial x} = \frac{4\pi}{c} J^y, \tag{2.143}$$

$$\frac{\partial B^y}{\partial x} - \mathrm{i}k_y B^x = \frac{4\pi}{c} J^z, \tag{2.144}$$

$$\frac{\partial B^x}{\partial x} + \mathrm{i}k_y B^y + \mathrm{i}k_z B^z = 0, \tag{2.145}$$

Due to (2.142) and (2.145) one of the equations (2.143) and (2.144) is redundant and, introducing the new unknown,

$$F = \frac{\mathrm{i}B^z}{k_z} = \frac{\mathrm{i}B^y}{k_y}, \tag{2.146}$$

we reduce the set of remaining three equations to two equations,

$$\frac{\partial F}{\partial x} + B^x = \frac{4\pi\mathrm{i}}{c k_y} J^z = -\frac{4\pi\mathrm{i}}{c k_z} J^y, \tag{2.147}$$

$$\frac{\partial B^x}{\partial x} + k^2 F = 0, \tag{2.148}$$

where $k^2 = k_y^2 + k_z^2$. We set the boundary conditions $B^x(-L) = 0$, which models the magnetic axis, and $B^x(L) = B_{\mathrm{v}L}$, which models the vacuum field driven by the external coil current. With the shielding current (2.141), the equation set (2.147) to (2.148) is solved in three regions. In the regions $-L < x < -\Delta x$ and $\Delta x < x < L$ where $J^y = J^z = 0$, the solutions are

$$B^x(x) = \left(\mathrm{e}^{k(x+L)} - \mathrm{e}^{-k(x+L)}\right) B_-, \qquad -L \le x \le -\Delta x, \tag{2.149}$$

$$B^x(x) = \left(\mathrm{e}^{k(x-L)} - \mathrm{e}^{-k(x-L)}\right) B_+ + \mathrm{e}^{k(x-L)} B_{\mathrm{v}L}, \qquad \Delta x \le x \le L, \tag{2.150}$$

where B_- is a free constant in the left (inner) region and B_+ is a free constant in the right (outer) region. In the middle region $-\Delta x < x < \Delta x$, where

$$\frac{4\pi\mathrm{i}}{c}\frac{J^z}{k_y} = -\frac{4\pi\mathrm{i}}{c}\frac{J^y}{k_z} = \frac{4\pi\mathrm{i}}{c}\frac{h^z}{k_y} J_\mathrm{s} = B_{\mathrm{s}0}, \tag{2.151}$$

the solution is

$$B^x(x) = B_{s0} + \beta_+ e^{kx} - \beta_- e^{-kx}, \qquad -\Delta x \le x \le \Delta x. \tag{2.152}$$

Since B^x and its derivatives are continuous at the region boundaries, we obtain four linear equations for the four unknown constants B_-, B_+, β_+ and β_-.

It is more convenient to consider the field $B^x_v(x)$ driven by the coil current and the field $B^x_s(x)$ driven by the shielding current separately,

$$B^x = B^x_v(x) + B^x_s(x). \tag{2.153}$$

The first of these fields does not require splitting into three regions since it is obtained for $B_{s0} = 0$. This solution can immediately be written as

$$B^x_v(x) = B_{vL} \frac{\sinh\left(k(x+L)\right)}{\sinh(2kL)}. \tag{2.154}$$

For the field driven by the shielding current, we should set $B_{vL} = 0$ in (2.150). Then, $B^x_s(x) = B^x_s(-x)$ is an even function, which is given explicitly for the three regions as

$$B^x_s(x) = B_{s0} \frac{\sinh(k\Delta x)}{\cosh(kL)} \sinh\left(k(L+x)\right), \qquad -L \le x \le -\Delta x, \tag{2.155}$$

$$B^x_s(x) = B_{s0} \left(1 - \frac{\cosh\left(k(L-\Delta x)\right)}{\cosh(kL)} \cosh(kx)\right), \qquad -\Delta x \le x \le \Delta x, \tag{2.156}$$

$$B^x_s(x) = B_{s0} \frac{\sinh(k\Delta x)}{\cosh(kL)} \sinh\left(k(L-x)\right), \qquad \Delta x \le x \le L. \tag{2.157}$$

An example for these two fields is shown in figure 2.2.

Now we link the amplitude of the shielding current J_s to the radial magnetic field at two points, $x = -\Delta x$ and $x = \Delta x$. Since J_s can be expressed through B_{s0} via (2.151), we link B_{s0} directly to the radial magnetic field as follows,

$$B_{s0} = \alpha_- B^x(-\Delta x) + \alpha_+ B^x(\Delta x), \tag{2.158}$$

where α_- and α_+ are some constants to be determined. Using the explicit expressions (2.155) to (2.157) and the fact that $B^x_s(x)$ is an even function, we obtain an equation for B_{s0},

$$\begin{aligned} B_{s0} &= (\alpha_- + \alpha_+) B^x_s(\Delta x) + \alpha_- B^x_v(-\Delta x) + \alpha_+ B^x_v(\Delta x) \\ &= (\alpha_- + \alpha_+) B_{s0} \frac{\sinh(k\Delta x)}{\cosh(kL)} \sinh\left(k(L-\Delta x)\right) + \alpha_- B^x_v(-\Delta x) + \alpha_+ B^x_v(\Delta x), \end{aligned} \tag{2.159}$$

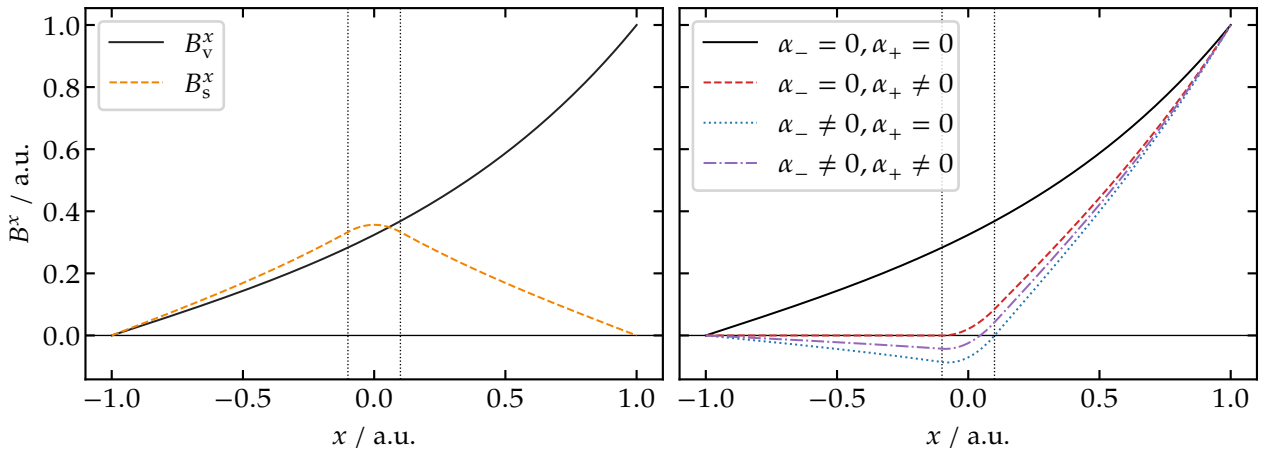

Figure 2.2: Radial magnetic fields $B^x_v(x)$, driven by the coil current, and $B^x_s(x)$, driven by the shielding current (left) and the sum of the two fields for different combinations of shielding constants $\alpha_\pm$ (right). The fields are evaluated according to (2.154) to (2.157) and (2.160) for the values $L = 1, \Delta x = 0.1, k = 1/L, B_{vL} = 1$. In the left plot, $B_{s0} = 5$, and in the right plot, the nonzero values are $\alpha_\pm = 10^4$. The dotted vertical lines indicate the boundaries at $\pm\Delta x$.

which is solved as

$$B_{s0} = \left(1 - (\alpha_- + \alpha_+)\frac{\sinh(k\Delta x)}{\cosh(kL)}\sinh\left(k(L-\Delta x)\right)\right)^{-1}\left(\alpha_- B^x_v(-\Delta x) + \alpha_+ B^x_v(\Delta x)\right). \quad (2.160)$$

The radial magnetic field driven by the shielding current at the edges of this current then is

$$B^x_s(\pm\Delta x) = \left(1 - (\alpha_- + \alpha_+)\frac{\sinh(k\Delta x)}{\cosh(kL)}\sinh\left(k(L-\Delta x)\right)\right)^{-1}\frac{\sinh(k\Delta x)}{\cosh(kL)}\sinh\left(k(L-\Delta x)\right) \times \\ \times \left(\alpha_- B^x_v(-\Delta x) + \alpha_+ B^x_v(\Delta x)\right). \quad (2.161)$$

We observe that there exists a particular value of the sum $(\alpha_- + \alpha_+)$ such that the denominator in (2.160) goes to zero. For this particular value, the iterations diverge – this is the only case where the preconditioned iterations cannot succeed in principle.

For estimations, it is convenient to simplify the exact expressions above using typical parameters for the modes of interest. These are the modes which can penetrate in the core region in the vacuum case, such that $kL \sim 1$ or $kL \ll 1$, since high poloidal modes with $kL \gg 1$ are exponentially small already in the vacuum case. In MEPHIT, the width Δx of the shielding current is limited by the radial grid divisions, which means $\Delta x \ll L$. For the modes of interest, this means also that $k\Delta x \ll 1$. In this limit, (2.161) can be approximately written as

$$B^x_s(\pm\Delta x) = \frac{k\Delta x \tanh(kL)}{1 - (\alpha_- + \alpha_+)k\Delta x \tanh(kL)}\left(\alpha_- B^x_v(-\Delta x) + \alpha_+ B^x_v(\Delta x)\right). \quad (2.162)$$

2.2.1.1 Large Shielding Constants

Our main interest is in large values of α_-, α_+, or both so that we can ignore the 1 in the denominator in (2.161). As follows from (2.162), this limit corresponds to

$$|\alpha_- + \alpha_+| k\Delta x \to \infty. \tag{2.163}$$

In this limit, we get for the field driven by the shielding current

$$B^x_{\mathrm{s}}(\pm\Delta x) \to -\frac{\alpha_- B^x_{\mathrm{v}}(-\Delta x) + \alpha_+ B^x_{\mathrm{v}}(\Delta x)}{\alpha_- + \alpha_+}, \tag{2.164}$$

which means that the total field is shielded,

$$B^x(\pm\Delta x) \to B^x_{\mathrm{v}}(\pm\Delta x) - \frac{\alpha_- B^x_{\mathrm{v}}(-\Delta x) + \alpha_+ B^x_{\mathrm{v}}(\Delta x)}{\alpha_- + \alpha_+} = \frac{\pm\alpha_\mp \left(B^x_{\mathrm{v}}(\Delta x) - B^x_{\mathrm{v}}(-\Delta x)\right)}{\alpha_- + \alpha_+}. \tag{2.165}$$

Introducing a "form factor" $f(x)$ as the ratio of total field to the vacuum field B^x_{v},

$$f(x) = \frac{B^x(x)}{B^x_{\mathrm{v}}(x)} = 1 + \frac{B^x_{\mathrm{s}}(x)}{B^x_{\mathrm{v}}(x)}, \tag{2.166}$$

we evaluate this form factor at the boundaries of the shielding current with substitution of (2.164) and (2.165), which gives

$$f(\pm\Delta x) \to \frac{\alpha_\mp}{\alpha_- + \alpha_+}\left(1 - \frac{B^x_{\mathrm{v}}(\mp\Delta x)}{B^x_{\mathrm{v}}(\pm\Delta x)}\right). \tag{2.167}$$

We see that shielding occurs if Δx is small compared to the scale of the vacuum field, $k\Delta x \ll 1$, which is the cases for the modes of interest. For these modes, using (2.154), we get in the leading order

$$\frac{B^x_{\mathrm{v}}(\mp\Delta x)}{B^x_{\mathrm{v}}(\pm\Delta x)} = \frac{\sinh\left(k(L \mp \Delta x)\right)}{\sinh\left(k(L \pm \Delta x)\right)} \approx 1 \mp \frac{2k\Delta x}{\tanh(kL)}, \tag{2.168}$$

so that

$$f(\pm\Delta x) \approx \frac{\pm\alpha_\mp}{\alpha_- + \alpha_+}\frac{2k\Delta x}{\tanh(kL)}. \tag{2.169}$$

Shielding improves with the reduction of the poloidal mode number k since for $kL \sim 1$ we have

$$f(\pm\Delta x) \sim \frac{\alpha_\mp}{\alpha_- + \alpha_+} k\Delta x, \tag{2.170}$$

but then it saturates for very small $kL \ll 1$,

$$f(\pm\Delta x) \approx \frac{\pm\alpha_{\mp}}{\alpha_- + \alpha_+}\frac{2\Delta x}{L}. \tag{2.171}$$

If we use only one boundary, say, $x = \Delta x$ for setting the shielding current, this corresponds to $\alpha_- = 0$. We can see from (2.169) that $f(\Delta x) = 0$ and $f(-\Delta x) = k\Delta x/\tanh(kL)$ with this choice, i.e., shielding is complete at the chosen boundary and is up to $k\Delta x \ll 1$ at the other one.

An example of strong shielding at the outer and at the inner edge of the shielding current is shown in figure 2.2. Results in the right plot are computed for large value of $\alpha_+ + \alpha_- = 10^4$ and are already close to the asymptotical limit (2.164). Results for smaller values of this parameter and shielding at the outer edge, $\alpha_- = 0$, are shown in figure 2.3.

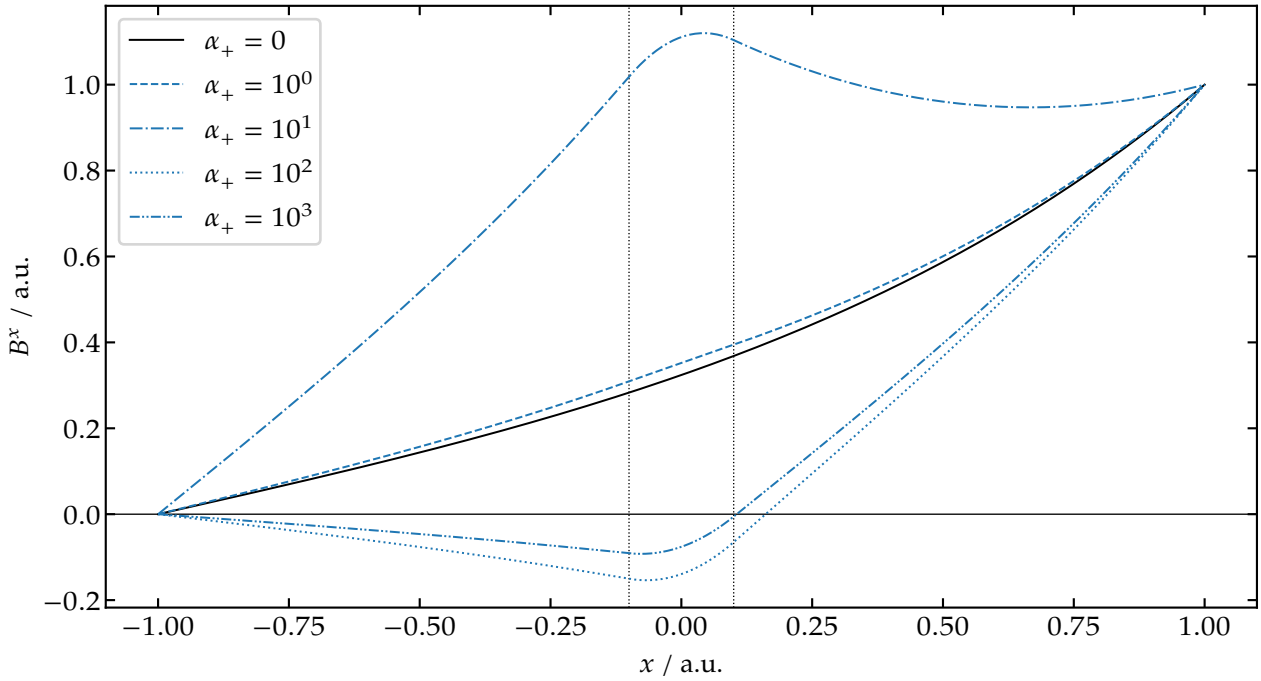

Figure 2.3: Total radial magnetic field for $\alpha_- = 0$ and different values of α_+. The remaining parameters are the same as in figure 2.2 and the dotted vertical lines indicate the boundaries at $\pm\Delta x$. The case $\alpha_- = \alpha_+ = 0$ again corresponds to the vacuum field.

They are quite demonstrative. It can be seen that $\alpha_+ = 1$ is too small to cause any shielding, $\alpha_+ = 100$ is already close to the asymptotical case and $\alpha_+ = 1000$ is almost indistinguishable from that case. At the same time, we see even an amplification for $\alpha_+ = 10$ which corresponds to the intermediate case with $|\alpha_- + \alpha_+|k\Delta x = 1$, according to the parameters given for figure 2.2 in contrast to to (2.163).

Thus, we conclude that using this method without compensation at the boundaries of the shielding current, meaning $|\alpha_- + \alpha_+| \sim \max|\alpha_\pm|$, an effect resulting, finally, in shielding occurs

if

$$\max|\alpha_{\pm}| > \frac{1}{|k\Delta x|} \gg 1. \tag{2.172}$$

2.2.1.2 Method with Compensation

It can be seen from (2.169) that instead of shielding there is an infinite amplification if we take $\alpha_{-} = -\alpha_{+}$. On the other hand, this case does not fit our strong shielding limit (2.164). Therefore we consider it separately using the exact formula (2.161), which results in

$$\begin{aligned} B^x_{\mathrm{s}}(\pm\Delta x) &= \alpha_{+}\frac{\sinh(k\Delta x)}{\cosh(kL)}\sinh\left(k(L-\Delta x)\right)\left(B^x_{\mathrm{v}}(\Delta x) - B^x_{\mathrm{v}}(-\Delta x)\right) \\ &\approx \frac{\alpha_{+}k\Delta x}{\tanh(kL)}\left(B^x_{\mathrm{v}}(\Delta x) - B^x_{\mathrm{v}}(-\Delta x)\right). \end{aligned} \tag{2.173}$$

For the form factor (2.166), we use the approximation $k\Delta x \ll 1$ as we did for (2.168), and obtain

$$f(\pm\Delta x) \approx 1 + 2\alpha_{+}\left(\frac{k\Delta x}{\tanh(kL)}\right)^2. \tag{2.174}$$

We can see that in contrast to the uncompensated case, an indefinite increase of α_{+} does not cause shielding, but instead leads to the indefinite amplification of the field. On the other hand, the effect of shielding shows up for much larger values of α_{+} as compared to (2.172), such that

$$|\alpha_{+}| > \frac{1}{(k\Delta x)^2} \gg 1. \tag{2.175}$$

This is compatible with our aim to create a scheme where resonant currents, which should be shielded, are treated with the uncompensated method, and the non-resonant currents, which should not be shielded, are treated with the compensated method.

2.2.1.3 Discrimination of Modes via Pressure Perturbation

It is obvious from the estimates (2.172) and (2.175) that shielding of the modes in the case where the amplitude of the shielding current is linked directly to the radial magnetic field via (2.158) with fixed constants $\alpha_{\pm}$ does not distinguish resonant modes from non-resonant modes and shields (or does not shield) them all in a similar way. Therefore, in order to make the constants $\alpha_{\pm}$ sensitive to the resonance condition, we use the pressure perturbation to discriminate the modes. Specifically, the "helical" current density J_{s} is linked to the pressure perturbation via

$$J_{\mathrm{s}} = B_0\left(C_{-}p(-\Delta x) + C_{+}p(\Delta x)\right), \tag{2.176}$$

where the pressure perturbation is given by

$$p(x) = \frac{\mathrm{i}p_0'(x)}{B_0 k_\parallel(x)} B^x(x), \tag{2.177}$$

with the equilibrium pressure p_0, the equilibrium magnetic field modulus B_0, and

$$k_\parallel(x) = \boldsymbol{k} \cdot \boldsymbol{h}(x) = k_y h^y(x) + k_z h^z(x). \tag{2.178}$$

Combining (2.177) with (2.176) and substituting the result into (2.151), we obtain

$$B_{s0} = -\frac{4\pi}{c}\frac{h^z}{k_y}\left(C_- \frac{p_0'(-\Delta x)}{k_\parallel(-\Delta x)} B^x(-\Delta x) + C_+ \frac{p_0'(\Delta x)}{k_\parallel(\Delta x)} B^x(\Delta x) \right). \tag{2.179}$$

Comparing this to (2.158), we obtain

$$\alpha_\pm = -\frac{4\pi}{c}\frac{h^z}{k_y}\frac{p_0'(\pm\Delta x)}{k_\parallel(\pm\Delta x)} C_\pm = \frac{4\pi}{c}\frac{h^y}{k_z}\frac{p_0'(\pm\Delta x)}{k_\parallel(\pm\Delta x)} C_\pm. \tag{2.180}$$

It is obvious from the last expression that the only quantity which is mode-dependent is $k_\parallel$, since k_z corresponds to the toroidal mode number n which we consider fixed in the context of toroidal Fourier series expansion.

2.2.1.4 Method without Compensation

First, let us obtain the criteria for $C_\pm$ for the uncompensated method by setting one of the constants, say $C_- = 0$. Then, according to (2.175), we must fulfill the condition $|\alpha_+ k\Delta x| \gg 1$ for the resonant mode and the condition $|\alpha_+ k\Delta x| \ll 1$ for the non-resonant modes. The second condition is most critical for the nearest non-resonant mode which is non-resonant within the limits of the shielding current but its resonant point is the closest to the shielding current. For both resonant and nearest non-resonant modes we will use the expansion of $k_\parallel(x)$ around the resonant point, which we denote with x_s for the resonant mode and with $x_{\bar{s}}$ for the non-resonant mode, respectively yielding

$$k_\parallel(x) \approx \frac{\partial k_\parallel(x_{s,\bar{s}})}{\partial x}(x - x_{s,\bar{s}}) = k_\parallel'(x - x_{s,\bar{s}}). \tag{2.181}$$

Thus we obtain a double condition for the coefficient C_+,

$$|\Delta x - x_s| \ll \left| \frac{4\pi h^y p_0'}{c k_z k_\parallel'} k\Delta x \right| |C_+| \ll |\Delta x - x_{\bar{s}}|, \tag{2.182}$$

where we assumed that the derivative $k_\parallel'$ is about the same for both modes. For the resonant mode, we have to take the largest possible value of $|\Delta x - x_s|$, which is obtained for $x_s = 0$. For the non-resonant mode, we assume $|x_{\bar{s}}| \gg \Delta x$. Thus, the estimate (2.182) for x_s in general

location is

$$1 \ll \left|\frac{4\pi h^y k p_0'}{c k_z k_\parallel'}\right| |C_+| \ll \frac{|x_{\bar{s}}|}{\Delta x}. \tag{2.183}$$

We see that uncompensated method has a relatively narrow window for coarse grids where the condition $\Delta x \ll |x_{\bar{s}}|$ is not very strong. It is convenient to rewrite (2.183) in terms of threshold constant

$$C_s = \left|\frac{c k_z k_\parallel'}{4\pi h^y k p_0'}\right| \tag{2.184}$$

so that it takes the form

$$1 \ll \frac{|C_+|}{C_s} \ll \frac{|x_{\bar{s}}|}{\Delta x}. \tag{2.185}$$

Note that for strong shielding we need $|C_+| \gg C_s$, while $|C_+| \approx C_s$ can even result in an amplification of the resonant mode.

2.2.1.5 Method with Selective Compensation

Due to the dependence of the coefficients $\alpha_\pm$ on x in (2.180), the choice $C_- = -C_+$ does not mean that the compensation condition $\alpha_- = -\alpha_+$ is fulfilled exactly. Moreover, for the resonant mode with $-\Delta x < x_s < \Delta x$, the compensation condition for $\alpha_\pm$ is not fulfilled at all, which can be seen by keeping the dependence on x in (2.180) only for $k_\parallel(x)$ and ignoring the small change of p_0' over the resonant layer. With this, we obtain

$$\alpha_- = \frac{\Delta x + x_s}{\Delta x - x_s}\alpha_+, \tag{2.186}$$

i.e., both $\alpha_\pm$ have the same sign. Therefore, $|C_+| \gg C_s$ remains a sufficient criterion for strong shielding of the resonant mode, the same as in the uncompensated method.

As can be seen from (2.180), again ignoring the change of p_0' which has a larger scale than $k_\parallel$, we have partial compensation of $\alpha_\pm$ for the non-resonant modes,

$$\alpha_- \approx -\alpha_+ \left(1 - \frac{2\Delta x}{x_{\bar{s}}}\right), \tag{2.187}$$

with $|x_{\bar{s}}| \gg \Delta x$. Since we have only partial compensation, we cannot use the limit of large shielding constants of section 2.2.1.1 or the limit of full compensation of section 2.2.1.2 and, therefore, we use as a starting point the more general expression (2.162). Together with (2.187), this yields

$$B_s^x(\pm\Delta x) = \frac{\alpha_+ k\Delta x \tanh(kL)}{1 - 2\alpha_+ k\Delta x^2 \tanh(kL) x_{\bar{s}}^{-1}} \left(B_v^x(\Delta x) - B_v^x(-\Delta x)\left(1 - \frac{2\Delta x}{x_{\bar{s}}}\right)\right). \tag{2.188}$$

Using (2.168), we approximate the last parentheses as

$$\left(B_{\mathrm{v}}^{x}(\Delta x)-B_{\mathrm{v}}^{x}(-\Delta x)\left(1-\frac{2\Delta x}{x_{\bar{\mathrm{s}}}}\right)\right)\approx 2\Delta x B_{\mathrm{v}}^{x}(\pm\Delta x)\left(k+\frac{1}{x_{\bar{\mathrm{s}}}}\right), \tag{2.189}$$

and the condition of weak non-resonant mode shielding $|B_{\mathrm{s}}^{x}| \ll |B_{\mathrm{v}}^{x}|$ takes the form

$$\left|\frac{B_{\mathrm{s}}^{x}(\pm\Delta x)}{B_{\mathrm{v}}^{x}(\pm\Delta x)}\right| \approx \left|\frac{2\alpha_{+}k\Delta x^{2}\tanh(kL)(k+x_{\bar{\mathrm{s}}}^{-1})}{1-2\alpha_{+}k\Delta x^{2}\tanh(kL)x_{\bar{\mathrm{s}}}^{-1}}\right| \ll 1. \tag{2.190}$$

For the modes of interest, we estimate $\tanh(kL) \sim 1$, yielding as a sufficient condition for weak shielding

$$|\alpha_{+}|\,k\Delta x^{2}\max\left(k,\frac{1}{|x_{\bar{\mathrm{s}}}|}\right) \ll 1. \tag{2.191}$$

For the non-resonant mode, (2.180) and (2.184) result in

$$|\alpha_{+}| \approx \frac{|C_{+}|}{k|x_{\bar{\mathrm{s}}}|C_{\mathrm{s}}} \tag{2.192}$$

Then, the condition of strong shielding of the resonant mode, $|C_{+}| \gg C_{\mathrm{s}}$, combined with the condition of weak shielding of the nearest non-resonant mode take the form

$$1 \ll \frac{|C_{+}|}{C_{\mathrm{s}}} \ll \frac{x_{\bar{\mathrm{s}}}^{2}}{\Delta x^{2}\max\left(1,k|x_{\bar{\mathrm{s}}}|\right)}. \tag{2.193}$$

Comparing this to the conditions (2.185) of the uncompensated method, we see that the method with selective compensation allows for larger a shielding constant C_{+}, whose upper limit is now quadratic in the large parameter $x_{\bar{\mathrm{s}}}/\Delta x$, replacing the linear dependence in (2.185).

2.2.1.6 Extension to Tokamak Geometry

It is convenient to express quantities pertinent to slab geometry through quantities of tokamak geometry and so we write

$$x \to r - r_{0}, \qquad h^{y} \to \hat{h}^{\theta} \approx \frac{r}{qR_{0}}, \qquad k_{y} \to \hat{k}_{\theta} = \frac{m}{r}, \qquad k_{z} \to \hat{k}_{\varphi} = \frac{n}{R_{0}}, \tag{2.194}$$

where r_{0} is an appropriate offset for positioning x close to resonance position. For the parallel wave vector $k_{\parallel}$ and its derivative at the resonant surface we have

$$k_{\parallel}(x) \to \frac{m+nq(r)}{q(r)R_{0}}, \qquad \left(\frac{\partial k_{\parallel}}{\partial x}\right)_{x_{\mathrm{s}}} \to \frac{nq'}{qR_{0}}. \tag{2.195}$$

Since $\hat{k}_\varphi \ll \hat{k}_\theta$, we approximately have $k \approx \hat{k}_\theta$. Thus, our shielding threshold constant (2.184) takes the form

$$C_\mathrm{s} = \frac{c}{4\pi}\frac{n^2|q'|}{R_0|mp_0'|} = \frac{c}{4\pi}\frac{n|q'|}{qR_0|p_0'|}, \tag{2.196}$$

where we used the resonance condition $k_\parallel = 0$ to eliminate the explicit dependence on m. Derivatives of q and p_0 over the minor radius r can obviously be replaced with derivatives over any other flux surface label ψ without a formal change,

$$C_\mathrm{s} = \frac{c}{4\pi}\frac{n}{qR_0}\left|\frac{\partial q}{\partial \psi}\right|\left|\frac{\partial p_0}{\partial \psi}\right|^{-1}. \tag{2.197}$$

Finally, let us express the distance between nearest resonant modes $x_{\bar{\mathrm{s}}}$ in terms of tokamak geometry. If the mode m is resonant at the radius r_s, the nearest non-resonant poloidal modes $m \pm 1$ are resonant at the radii $r_\mathrm{s} + x_{\bar{\mathrm{s}}}$. Using (2.195), we get the resonance conditions for these modes as

$$k_\parallel(x_{\bar{\mathrm{s}}}) = \frac{m \pm 1 + nq(r_\mathrm{s} + x_{\bar{\mathrm{s}}})}{q(r_\mathrm{s} + x_{\bar{\mathrm{s}}})R_0} \approx \frac{\pm 1 + nq'(r_\mathrm{s})x_{\bar{\mathrm{s}}}}{q(r_\mathrm{s})R_0} = 0, \tag{2.198}$$

which results in

$$|kx_{\bar{\mathrm{s}}}| = \frac{|k|}{n|q'|} = \frac{|m|}{rn|q'|} = \frac{|q|}{r|q'|} = \frac{1}{|s|}, \tag{2.199}$$

where s is the shear parameter. Normally, $s \sim 1$, but it becomes large near the separatrix. Thus, we can transform the upper limits in the conditions (2.185) and (2.193) using

$$\frac{|x_{\bar{\mathrm{s}}}|}{\Delta x} = \frac{|kx_{\bar{\mathrm{s}}}|}{k\Delta x} \to \frac{r}{\Delta r|ms|} = \frac{q}{\Delta r|mq'|} = \frac{1}{n\Delta q}, \qquad \max(1, k|x_{\bar{\mathrm{s}}}|) \to 1, \tag{2.200}$$

where $\Delta q = q'\Delta r$ is the change of safety factor between radial positions on the grid. Consequently, the condition (2.185) for the uncompensated method takes the form

$$1 \ll \frac{|C_+|}{C_\mathrm{s}} \ll \frac{1}{n\Delta q}, \tag{2.201}$$

and the condition (2.193) for the compensated method takes the form

$$1 \ll \frac{|C_+|}{C_\mathrm{s}} \ll \frac{1}{n^2\Delta q^2}. \tag{2.202}$$

It can be seen that rather good radial grid resolution is needed for the uncompensated method due to the shear parameter. E.g., if we want to shield the resonant mode 10-fold and at the same time change the non-resonant modes by not more than 10 %, we need $n\Delta q < 0.01$, which means for $n = 2$ not more than 0.5 % change of the safety factor per radial grid step. This may

quickly get critical at the edge where q changes rapidly. The compensated method should work with higher change of 5 %, which allows for 10 times coarser grids. Finally, we stress that shielding threshold constant (2.197) is independent of the grid size and is the same for both methods.

As noted in [2], "[a]bove the lower limit in [(2.202)], shielding of the resonant poloidal mode is enforced; below the upper limit, the effect on the poloidal modes which are not resonant at given surface is minimized. It can be shown that the particular choice within these limits only slightly influences the resultant resonant current, and we choose the geometric mean of the lower and upper limits,

$$C_+ = \frac{C_\mathrm{s}}{n\Delta q}. \tag{2.203}$$

If we use poloidal modes [as suggested by (2.133)], we can discriminate between resonant and non-resonant modes directly, thus eliminating the upper limit in [(2.202)]. It nevertheless serves as a useful estimate."

2.2.1.7 Shielding Current

As a last step, let us show that the shielding current depends only weakly on the shielding constants if the shielding is strong. We define the linear density of this current as

$$j_\mathrm{s} = \int_{-L}^{L} \mathrm{d}x\, \boldsymbol{J}\cdot\boldsymbol{h}\, \mathrm{e}^{-\mathrm{i}k_y y - \mathrm{i}k_z z} = 2\Delta x J_\mathrm{s}, \tag{2.204}$$

where (2.141) has been used. According to (2.151), we have

$$\frac{4\pi\mathrm{i}}{c}\frac{h^z}{k_y} j_\mathrm{s} = 2\Delta x B_{\mathrm{s}0}, \tag{2.205}$$

and according to (2.157), we have

$$B^x_\mathrm{s}(\pm\Delta x) = B_{\mathrm{s}0}\frac{\sinh(k\Delta x)}{\cosh(kL)}\sinh\left(k(L-\Delta x)\right) \approx k\Delta x B_{\mathrm{s}0}\tanh(kL). \tag{2.206}$$

Relating the field of the shielding current to the vacuum field via the form factor (2.166) and using for this form factor the strong shielding limit (2.169), we get for the field of the shielding current

$$\begin{aligned} B^x_\mathrm{s}(\pm\Delta x) = \left(f(\pm\Delta x)-1\right) B^x_\mathrm{v}(\pm\Delta x) &= \left(\frac{\pm\alpha_\mp}{\alpha_- + \alpha_+}\frac{2k\Delta x}{\tanh(kL)} - 1\right) B^x_\mathrm{v}(\pm\Delta x) \\ &\approx -\left(1 + \frac{\alpha_- - \alpha_+}{\alpha_- + \alpha_+}\frac{k\Delta x}{\tanh(kL)}\right) B^x_\mathrm{v}(0) \end{aligned} \tag{2.207}$$

and thus for the line density (2.204) of the shielding current

$$j_{\mathrm{s}} \approx \frac{\mathrm{i}ck_y B_{\mathrm{v}}^x(0)}{2\pi h^z k \tanh(kL)} \left(1 + \frac{\alpha_- - \alpha_+}{\alpha_- + \alpha_+} \frac{k\Delta x}{\tanh(kL)}\right). \tag{2.208}$$

In our selective compensation method, $\alpha_-\alpha_+ > 0$ for the resonant mode, and thus $|\alpha_- - \alpha_+| < |\alpha_- + \alpha_+|$. Therefore the second term in parentheses, which depends on the shelding constants, is always small as $k\Delta x \ll 1$, i.e., the line density of the shielding current (2.204) is only weakly dependent on those constants.

Chapter 3

Kinetic Response Current

This chapter is based on the papers by Markl et al. [13] and Heyn et al. [14] and follows their notation, e.g., using $\boldsymbol{m} \equiv (m, n)$ to refer to the specific poloidal and toroidal Fourier mode of a linear perturbation indicated by an index of 1, unless noted otherwise. They consider a circular tokamak in the large aspect ratio limit, thus derivations are conducted in straight-cylinder coordinates (r, θ, z) discussed in section 1.1 for the most part. First, we shall recapitulate the derivations also for quantities not mentioned by Markl et al. [13] and Heyn et al. [14], where we specifically discuss the electric potential perturbation. Second, we adapt the solution thus obtained to toroidal geometry. Finally, we repeat these derivations for the finite Larmor radius expansion up to second order. A short summary of the results has already been published [3, 4].

In (60), Heyn et al. [14] give the drift-kinetic expression for the Fourier amplitude of the parallel current density of species α in the collisional case as

$$J^{\alpha}_{\parallel \boldsymbol{m}} = -\frac{n_\alpha e_\alpha v_{T\alpha}}{\nu_\alpha B_0} \left[\left(\left(A^\alpha_1 + A^\alpha_2\right) I^{11} + \frac{1}{2} A^\alpha_2 I^{31} \right) v_{T\alpha} B^r_{\boldsymbol{m}} + \right. \\ \left. + \left(\left(A^\alpha_1 + A^\alpha_2\right) I^{10} + \frac{1}{2} A^\alpha_2 I^{21} \right) c E_{\perp \boldsymbol{m}} \right]. \tag{3.1}$$

Here, n_α, e_α, $v_{T\alpha} = \sqrt{T_\alpha / m_\alpha}$, T_α, m_α, and ν_α are the density, charge, thermal velocity, temperature, mass, and collision frequency of species α, respectively. The thermodynamic forces are given in (22) of [14] as

$$A^\alpha_1 = \frac{1}{n_\alpha} \frac{\partial n_\alpha}{\partial r} + \frac{e_\alpha}{T_\alpha} \frac{\partial \Phi_0}{\partial r} - \frac{3}{2T_\alpha} \frac{\partial T_\alpha}{\partial r}, \qquad A^\alpha_2 = \frac{1}{T_\alpha} \frac{\partial T_\alpha}{\partial r}, \tag{3.2}$$

where Φ_0 is the equilibrium electric potential. The complex *susceptibility functions* $I^{kl}(x_1, x_2)$ are thoroughly discussed by Markl et al. [13] in appendix A; here we only repeat the definitions of its arguments according to (8) through (10):

$$x_1 = \frac{k_\parallel v_{T\alpha}}{\nu_\alpha}, \qquad x_2 = -\frac{\omega_E}{\nu_\alpha}, \tag{3.3}$$

where the wave vector (see also (1.15)) and its projections to the magnetic field unit vector

are given by

$$k_\parallel = \boldsymbol{k}\cdot\boldsymbol{h}, \qquad k_\perp = \boldsymbol{k}\cdot(\boldsymbol{h}\times\nabla r), \qquad \boldsymbol{k} = m\nabla\theta + \frac{n}{R_0}\nabla z, \qquad \boldsymbol{h} = \frac{\boldsymbol{B}_0}{B_0}, \tag{3.4}$$

and the electric rotation frequency[1] and the radial electric field are given by

$$\omega_E = k_\perp V_{E\times B} = -\frac{ck_\perp E_{0r}}{B_0}, \qquad E_{0r} = -\frac{\partial\Phi_0}{\partial r}. \tag{3.5}$$

x_1 can be interpreted as a normalized distance to the resonance position r_m, i.e., $x_1 \to 0$ as $r \to r_m$, because $k_\parallel \propto (r - r_m)$. x_2 is a proxy for collisionality, i.e., $x_2 \ll 1$ for high collisionality and $x_2 \gg 1$ in the collisionless limit.

The only quantity in (3.1) we have not yet accounted for is the perpendicular electric field perturbation

$$E_{\perp m} = -\mathrm{i}k_\perp \Phi_m. \tag{3.6}$$

To this end, we compute the perturbations of charge density and current density in the lowest order over Larmor radius, which means that we ignore the difference between the guiding center position and the actual particle position and treat the Fourier amplitude of the perturbed distribution function (3.13), defined at the guiding center position, as a function of actual particle position. Thus, when computing the current density (3.8) as a velocity-space integral of the distribution function times the actual particle velocity $v = v_\mathrm{g} + v_\mathrm{L}$, only the guiding center velocity v_g contributes to the current, while the Larmor gyration velocity v_L averages to zero upon integration over the gyrophase. Moreover, we retain in the guiding center velocity only the parallel motion and the $\boldsymbol{E}\times\boldsymbol{B}$ drift and ignore the magnetic drift, so that this velocity is

$$\boldsymbol{v}_\mathrm{g} \approx v_\parallel \frac{\boldsymbol{B}}{B} + c\frac{\boldsymbol{B}\times\nabla\Phi}{B^2}. \tag{3.7}$$

By doing so, we ignore the "polarization charge" density responsible for slow modes (drift mode in particular) and also the diamagnetic and Pfirsch-Schlüter current density. The latter two are important in the bulk plasma (outside resonant layers, where they provide small corrections) and are accounted for by the ideal MHD response currents covered in section 2.2.

We consider the definition of $J^\alpha_{\parallel m}$ in (60) of [14] as a moment of the perturbed distribution function,

$$J^\alpha_{\parallel m} = e_\alpha \int \mathrm{d}^3p\, v_\parallel f_m, \tag{3.8}$$

[1] For this definition, Markl et al. [13] use $V_{E\times B}$ where Heyn et al. [14] use $v_{E\perp}$, which is the perpendicular component of $\boldsymbol{v}_E$ in (3.12).

where f_m is the Fourier amplitude of (20),

$$\tilde{f} = f_1 + f_0 \frac{e_\alpha \Phi_1}{T_\alpha}, \tag{3.9}$$

the index 1 denotes the perturbation of linear order[1], and f_0^α is a local Maxwellian defined by (17),

$$f_0^\alpha(v_\perp, v_\parallel) = \frac{n_\alpha(r)}{(2\pi m_\alpha T_\alpha(r))^{\frac{3}{2}}} \exp\left(-\frac{m_\alpha\left(v_\perp^2 + v_\parallel^2\right)}{2T_\alpha(r)}\right). \tag{3.10}$$

We insert (37) into (40) and retain the first two terms of (29), i.e., those of zero order in Larmor radius,

$$v_m^r \approx \frac{v_\parallel}{B_0} B_m^r - \frac{\mathrm{i}ck_\perp}{B_0}\Phi_m \tag{3.11}$$

which is the Fourier amplitude of the radial guiding center velocity (drift velocity) $v_{\mathrm{g}1}^r$, and Φ_m is the Fourier amplitude of Φ_1. Compare this with the unperturbed (zero order) guiding center velocity given by (12) of [14],

$$\boldsymbol{v}_{\mathrm{g}0} \approx v_\parallel \frac{\boldsymbol{B}_0}{B_0} + \boldsymbol{v}_E, \qquad \boldsymbol{v}_E = c\frac{\boldsymbol{B}_0 \times \nabla\Phi_0}{B_0^2}, \tag{3.12}$$

where the same approximation has been made as in (3.7). Putting everything together, we arrive at

$$\begin{aligned} f_{1,m}^\alpha &= f_m^\alpha - \frac{e_\alpha \Phi_m}{T_\alpha} f_0^\alpha \\ &= -\int_{-\infty}^{\infty} \mathrm{d}v_\parallel' \, G_m(v_\parallel, v_\parallel') \left(A_1^\alpha + \frac{m_\alpha\left(v_\perp^2 + v_\parallel'^2\right)}{2T_\alpha} A_2^\alpha\right) f_0^\alpha(v_\perp, v_\parallel') \times \\ &\quad \times \left(\frac{v_\parallel'}{B_0} B_m^r - \frac{\mathrm{i}ck_\perp}{B_0}\Phi_m\right) - \frac{e_\alpha \Phi_m}{T_\alpha} f_0^\alpha(v_\perp, v_\parallel). \end{aligned} \tag{3.13}$$

Here, G_m is the Green's function of the kinetic equation.

Up to the linear order in perturbation amplitude, the distribution function of species α is given by $f^\alpha \approx f_0^\alpha + f_1^\alpha$. The charge and current density perturbations of this order are

$$\varrho_1 = \sum_\alpha e_\alpha \int \mathrm{d}^3p \, f_1^\alpha, \qquad \boldsymbol{J}_1 = \sum_\alpha e_\alpha \int \mathrm{d}^3p \, \left(\boldsymbol{v}_{\mathrm{g}0} f_1^\alpha + \boldsymbol{v}_{\mathrm{g}1} f_0^\alpha\right). \tag{3.14}$$

Due to the symmetry of the Maxwellian, the first term in (3.7) does not contribute to the

[1] B_1 in this chapter would correspond to δB in other chapters

current density. Thus, this density is

$$\sum_\alpha e_\alpha \int \mathrm{d}^3p\, \boldsymbol{v}_{\mathrm{g}1} f_0^\alpha = c \sum_\alpha e_\alpha \left(\frac{\boldsymbol{B} \times \nabla \Phi}{B^2} \right)_1 n_\alpha = 0 \tag{3.15}$$

due to the charge neutrality condition,

$$\sum_\alpha e_\alpha n_\alpha = 0. \tag{3.16}$$

Thus we obtain for the Fourier amplitudes of current and charge density perturbations

$$\boldsymbol{J}_{\boldsymbol{m}} = \sum_\alpha e_\alpha \int \mathrm{d}^3p\, f_{1,\boldsymbol{m}}^\alpha \left(\boldsymbol{h} v_\parallel + \boldsymbol{v}_E \right) = \boldsymbol{h} J_{\parallel \boldsymbol{m}} + \boldsymbol{v}_E \varrho_{\boldsymbol{m}}, \tag{3.17}$$

$$\varrho_{\boldsymbol{m}} = \sum_\alpha e_\alpha \int \mathrm{d}^3p\, f_{1,\boldsymbol{m}}^\alpha. \tag{3.18}$$

It can be seen that current density has no radial component, i.e., it is tangential to the unperturbed flux surfaces. Now, we insert (3.13) and (3.10), and integrate over $p_\perp = m_\alpha v_\perp$ to obtain

$$\begin{aligned} J_{\parallel \boldsymbol{m}} = &- \sum_\alpha \frac{e_\alpha n_\alpha}{\sqrt{2\pi}\, v_{T\alpha} B_0} \int_{-\infty}^{\infty} \mathrm{d}v_\parallel \int_{-\infty}^{\infty} \mathrm{d}v_\parallel'\, G_{\boldsymbol{m}}(v_\parallel, v_\parallel') \left(A_1^\alpha + A_2^\alpha + \frac{{v_\parallel'}^2}{2v_{T\alpha}^2} A_2^\alpha \right) \times \\ &\times \exp\left(-\frac{{v_\parallel'}^2}{2v_{T\alpha}^2} \right) \left(v_\parallel' B_{\boldsymbol{m}}^r + c E_{\perp \boldsymbol{m}} \right) v_\parallel, \end{aligned} \tag{3.19}$$

$$\begin{aligned} \varrho_{\boldsymbol{m}} = &- \sum_\alpha \frac{e_\alpha n_\alpha}{\sqrt{2\pi}\, v_{T\alpha} B_0} \int_{-\infty}^{\infty} \mathrm{d}v_\parallel \int_{-\infty}^{\infty} \mathrm{d}v_\parallel'\, G_{\boldsymbol{m}}(v_\parallel, v_\parallel') \left(A_1^\alpha + A_2^\alpha + \frac{{v_\parallel'}^2}{2v_{T\alpha}^2} A_2^\alpha \right) \times \\ &\times \exp\left(-\frac{{v_\parallel'}^2}{2v_{T\alpha}^2} \right) \left(v_\parallel' B_{\boldsymbol{m}}^r + c E_{\perp \boldsymbol{m}} \right) - \sum_\alpha \frac{e_\alpha^2 n_\alpha}{T_\alpha} \Phi_{\boldsymbol{m}}, \end{aligned} \tag{3.20}$$

where we used (3.6). These quantities can be expressed in terms of the susceptibility functions defined via (50) of [14],

$$\begin{aligned} J_{\parallel \boldsymbol{m}} = &- \sum_\alpha \frac{e_\alpha n_\alpha v_{T\alpha}}{\nu_\alpha B_0} \left[\left(\left(A_1^\alpha + A_2^\alpha \right) I^{11} + \frac{1}{2} A_2^\alpha I^{13} \right) v_{T\alpha} B_{\boldsymbol{m}}^r + \right. \\ &\left. + \left(\left(A_1^\alpha + A_2^\alpha \right) I^{10} + \frac{1}{2} A_2^\alpha I^{12} \right) c E_{\perp \boldsymbol{m}} \right], \end{aligned} \tag{3.21}$$

$$\begin{aligned} \varrho_{\boldsymbol{m}} = &- \sum_\alpha \frac{e_\alpha n_\alpha}{\nu_\alpha B_0} \left[\left(\left(A_1^\alpha + A_2^\alpha \right) I^{01} + \frac{1}{2} A_2^\alpha I^{03} \right) v_{T\alpha} B_{\boldsymbol{m}}^r + \right. \\ &\left. + \left(\left(A_1^\alpha + A_2^\alpha \right) I^{00} + \frac{1}{2} A_2^\alpha I^{02} \right) c E_{\perp \boldsymbol{m}} \right] - \sum_\alpha \frac{e_\alpha^2 n_\alpha}{T_\alpha} \Phi_{\boldsymbol{m}}. \end{aligned} \tag{3.22}$$

The first of these expressions agrees with (3.1) due to the symmetry of susceptibility functions over indices, $I^{kl} = I^{lk}$.

Next, we show that the current density in (3.17) has zero divergence, i.e,

$$\boldsymbol{k} \cdot \boldsymbol{J}_{\boldsymbol{m}} = k_{\parallel} J_{\parallel \boldsymbol{m}} + k_{\perp} v_E \varrho_{\boldsymbol{m}} = k_{\parallel} J_{\parallel \boldsymbol{m}} + \omega_E \varrho_{\boldsymbol{m}} = 0, \tag{3.23}$$

where we used (3.5) in the last step. Substituting (3.21) and (3.22), we obtain

$$\begin{aligned} \boldsymbol{k} \cdot \boldsymbol{J}_{\boldsymbol{m}} = -\sum_{\alpha} \frac{e_\alpha n_\alpha k_{\parallel} v_{T\alpha}}{\nu_\alpha B_0} \Bigg[\left(\left(A_1^\alpha + A_2^\alpha \right) \left(I^{11} - \sqrt{2} z_\alpha I^{01} \right) + \frac{1}{2} A_2^\alpha \left(I^{13} - \sqrt{2} z_\alpha I^{03} \right) \right) v_{T\alpha} B_{\boldsymbol{m}}^r + \\ + \left(\left(A_1^\alpha + A_2^\alpha \right) \left(I^{10} - \sqrt{2} z_\alpha I^{00} \right) + \frac{1}{2} A_2^\alpha \left(I^{12} - \sqrt{2} z_\alpha I^{02} \right) \right) c E_{\perp \boldsymbol{m}} \Bigg] - \sum_{\alpha} \frac{e_\alpha^2 n_\alpha}{T_\alpha} \omega_E \Phi_{\boldsymbol{m}}, \end{aligned} \tag{3.24}$$

where we used

$$\sqrt{2} z_\alpha = \frac{x_2}{x_1} = -\frac{\omega_E}{k_{\parallel} v_{T\alpha}} \tag{3.25}$$

from (A5) in [13], as well as the following recurrence relations between susceptibility functions, also discussed in appendix A of [13]:

$$I^{10} = \sqrt{2} z_\alpha I^{00} - \frac{\mathrm{i}}{x_1}, \tag{3.26}$$

$$I^{11} = \sqrt{2} z_\alpha I^{01}, \tag{3.27}$$

$$I^{12} = \sqrt{2} z_\alpha I^{02} - \frac{\mathrm{i}}{x_1}, \tag{3.28}$$

$$I^{13} = \sqrt{2} z_\alpha I^{03} = \sqrt{2} z_\alpha I^{12}. \tag{3.29}$$

We notice that the factor in front of the magnetic field perturbation (on the first line in (3.24)) is identically zero while the factor in front of the perpendicular electric field perturbation (on the second line in (3.24)) does not contain susceptibility functions anymore. We insert x_1 from (3.3), as well as (3.6), (3.2), and (3.5) to arrive at

$$\begin{aligned} \boldsymbol{k} \cdot \boldsymbol{J}_{\boldsymbol{m}} &= \sum_{\alpha} \frac{e_\alpha n_\alpha}{B_0} \left(A_1^\alpha + \frac{3}{2} A_2^\alpha \right) \mathrm{i} c E_{\perp \boldsymbol{m}} - \sum_{\alpha} \frac{e_\alpha^2 n_\alpha}{T_\alpha} \omega_E \Phi_{\boldsymbol{m}} \\ &= \sum_{\alpha} \frac{e_\alpha n_\alpha}{B_0} \left(\frac{1}{n_\alpha} \frac{\partial n_\alpha}{\partial r} + \frac{e_\alpha}{T_\alpha} \frac{\partial \Phi_0}{\partial r} \right) c k_\perp \Phi_{\boldsymbol{m}} - \sum_{\alpha} \frac{e_\alpha^2 n_\alpha}{T_\alpha} \frac{c k_\perp}{B_0} \frac{\partial \Phi_0}{\partial r} \Phi_{\boldsymbol{m}} \\ &= \frac{c k_\perp}{B_0} \Phi_{\boldsymbol{m}} \frac{\partial}{\partial r} \sum_{\alpha} e_\alpha n_\alpha = 0, \end{aligned} \tag{3.30}$$

where charge neutrality (3.16) accounts for the last step.

3.1 Electric Potential Perturbation

We rewrite the charge density in (3.22) via the recurrence relations (3.26) through (3.29) to arrive at

$$\begin{aligned}\varrho_m = &-\sum_\alpha \frac{e_\alpha n_\alpha v_{T\alpha}}{\nu_\alpha B_0}\left(\left(A_1^\alpha + A_2^\alpha\right) I^{01} + \frac{1}{2}A_2^\alpha I^{03}\right)\left(B_m^r + \frac{cx_1}{v_{T\alpha}x_2}E_{\perp m}\right) - \\ &-\sum_\alpha \frac{e_\alpha n_\alpha}{\nu_\alpha B_0}\left(A_1^\alpha + \frac{3}{2}A_2^\alpha\right)\frac{\mathrm{i}c}{x_2}E_{\perp m} - \sum_\alpha \frac{e_\alpha^2 n_\alpha}{T_\alpha}\Phi_m.\end{aligned} \tag{3.31}$$

The second line of (3.31) corresponds to $\omega_E \boldsymbol{k}\cdot\boldsymbol{J}_m$, which can be seen from the first line of (3.30), and vanishes accordingly. Therefore, the charge density is

$$\varrho_m = -\left(\frac{B_m^r}{B_0} - \frac{\mathrm{i}k_\parallel \Phi_m}{E_{0r}}\right)\sum_\alpha \frac{e_\alpha n_\alpha v_{T\alpha}}{\nu_\alpha}\left(\left(A_1^\alpha + A_2^\alpha\right) I^{01} + \frac{1}{2}A_2^\alpha I^{03}\right). \tag{3.32}$$

Comparing this result to the *misalignment field* given by (12) of [13],

$$E_{\perp m}^{\mathrm{MA}} = E_{\perp m} + \frac{k_\perp B_m^r}{k_\parallel B_0}E_{0r}, \tag{3.33}$$

we can see that

$$\frac{B_m^r}{B_0} - \frac{\mathrm{i}k_\parallel \Phi_m}{E_{0r}} = \frac{k_\parallel E_{\perp m}^{\mathrm{MA}}}{k_\perp E_{0r}}. \tag{3.34}$$

Introducing the misaligment potential as

$$\Phi_m^{\mathrm{MA}} = \frac{\mathrm{i}E_{\perp m}^{\mathrm{MA}}}{k_\perp} = \Phi_m + \mathrm{i}\frac{E_{0r}B_m^r}{k_\parallel B_0}, \tag{3.35}$$

we can present (3.32) as

$$\varrho_m = -\frac{\mathrm{i}\Phi_m^{\mathrm{MA}}}{E_{0r}}\sum_\alpha e_\alpha n_\alpha x_1\left(\left(A_1^\alpha + A_2^\alpha\right) I^{01} + \frac{1}{2}A_2^\alpha I^{03}\right). \tag{3.36}$$

The implications become apparent when we consider the Poisson equation for the potential perturbation Φ_1,

$$\Delta\Phi_1 = -4\pi\varrho_1 = \cdots + \sum_\alpha \frac{\Phi_1}{\lambda_{\mathrm{D}\alpha}^2}, \tag{3.37}$$

where we inserted (3.22) and focussed on the last term, which also contains the potential perturbation, as well as the Debye length

$$\lambda_{\mathrm{D}\alpha} = \sqrt{\frac{T_\alpha}{4\pi n_\alpha e_\alpha^2}}. \tag{3.38}$$

We estimate the Laplacian term as

$$\Delta\Phi_1 \sim \frac{\Phi_1}{\delta_m^2}, \tag{3.39}$$

where δ_m is the typical resonant layer width according to (45) of [13]. Since $\delta_m^2 \gg \lambda_{\mathrm{D}\alpha}^2$, we could neglect the Laplacian term and continue with charge neutrality, i.e., $\varrho_m = 0$. However, for (3.32) to fulfill this condition it is required that (3.34) becomes zero. In this case, the perturbed equipotential surfaces coincide with the perturbed flux surfaces, which means the misalignment field vanishes and shielding is lost according to (13) of [13]. Moreover, $k_\parallel \to 0$ approaching the resonance position, resulting in a singular Φ_m there, which would need to be balanced by a correspondingly large term to achieve vanishing ϱ_m. Thus, further investigation is warranted.

In the region outside the resonant layer, where we apply iMHD, we derive the asymptotics of the susceptibility functions as follows. In the case of high collisionality, we have $x_1^2 \gg |x_2|$, which we use to further approximate (A11) of [13]. In the case of low collisionality, we have $x_1^2 \gg x_2^2$, equivalent to $z_\alpha \ll 1$, which we use to further approximate (A18) of [13]. Together with (3.29), both approximations yield

$$I^{01} \approx I^{03} \approx -\frac{\mathrm{i}}{x_1}, \quad |x_1| \gg 1. \tag{3.40}$$

Inserting this into (3.36) yields

$$\begin{aligned}\varrho_m &\to -\frac{\Phi_m^{\mathrm{MA}}}{E_{0r}} \sum_\alpha e_\alpha n_\alpha \left(A_1^\alpha + \frac{3}{2}A_2^\alpha\right) = -\frac{\Phi_m^{\mathrm{MA}}}{E_{0r}} \sum_\alpha e_\alpha n_\alpha \left(\frac{1}{n_\alpha}\frac{\partial n_\alpha}{\partial r} + \frac{e_\alpha}{T_\alpha}\frac{\partial \Phi_0}{\partial r}\right) \\ &= -\Phi_m^{\mathrm{MA}} \sum_\alpha \frac{e_\alpha^2 n_\alpha}{T_\alpha} = -\Phi_m^{\mathrm{MA}} \sum_\alpha \frac{1}{4\pi\lambda_{\mathrm{D}\alpha}^2}.\end{aligned} \tag{3.41}$$

In this case, the Poisson equation (3.37) reads

$$\Delta\Phi_1 = \Phi_1^{\mathrm{MA}} \sum_\alpha \frac{1}{\lambda_{\mathrm{D}\alpha}^2} = (\Phi_1 - \Phi_1^{\mathrm{A}}) \sum_\alpha \frac{1}{\lambda_{\mathrm{D}\alpha}^2}, \tag{3.42}$$

where Φ_1^{A} is the potential aligned with the perturbed flux surfaces. Its Fourier amplitude

follows from (3.35) as

$$\Phi_m^{\mathrm{A}} = -\mathrm{i}\frac{E_{0r}B_m^r}{k_\parallel B_0}, \tag{3.43}$$

which means that it satisfies the magnetic differential equation

$$\mathrm{i}k_\parallel B_0 \Phi_m^{\mathrm{A}} + B_m^r \frac{\partial \Phi_0}{\partial r} = 0. \tag{3.44}$$

Respectively, the aligned potential satisfies

$$\boldsymbol{B}_0 \cdot \nabla \Phi_1^{\mathrm{A}} + B_1^r \frac{\partial \Phi_0}{\partial r} = 0, \tag{3.45}$$

which is the same form as for the pressure perturbation (2.113) if one replaces the unperturbed pressure p_0 with the unperturbed electrostatic potential Φ_0. Actually, this equation is valid also in real tokamak geometry, and can be used for setting boundary conditions at the boundaries of the resonant layer. Indeed, far from the resonance position r_m where $|r - r_m| \gg \delta_m \gg \lambda_{\mathrm{D}\alpha}$ such that the asymptotical approximation (3.42) is already valid one can ignore the Laplacian in the left-hand side of (3.42) which means a fully aligned field, $\Phi_1 = \Phi_1^{\mathrm{A}}$.

Within the resonant layer, however, we cannot ignore the Laplacian, as previously discussed. Close to the resonant surface where $|r - r_m| \ll \delta_m$, the asymptotics of the susceptibility functions are

$$I^{03} \approx 3I^{01} \approx \frac{3x_1}{x_2}, \quad |x_1| \ll 1, \tag{3.46}$$

which means that the coefficient of Φ_m^{MA} in (3.36) scales with $x_1^2 \propto k_\parallel^2 \propto (r - r_m)^2$. The inverse scaling of the aligned potential with distance to the flux surface, $\Phi_m^{\mathrm{MA}} \propto k_\parallel^{-1} \propto (r - r_m)^{-1}$, cannot beat the quadratic scaling of the coefficient. Therefore, the perturbation of the charge density vanishes at the resonant surface, and one cannot ignore the Laplacian there anymore since this is the only term remaining in the Poisson equation.

Application of the iterative approach to the Poisson equation (3.37) looks problematic. If we invert the Laplacian and iterate the right-hand side,

$$\Phi_1 = -4\pi\Delta^{-1}\varrho_1, \tag{3.47}$$

direct iterations (2.5) mean iterating over the large parameter $\delta_m^2/\lambda_{\mathrm{D}\alpha}^2 \gg 1$. Preconditioned iterations (2.16) will not help much because the number of large eigenvalues will be too high. One way to improve the convergence is to rewrite the Poisson equation as

$$\Delta\Phi_1 - \Phi_1 \sum_\alpha \frac{1}{\lambda_{\mathrm{D}\alpha}^2} = -4\pi\varrho_1 - \Phi_1 \sum_\alpha \frac{1}{\lambda_{\mathrm{D}\alpha}^2} \tag{3.48}$$

and then invert the left-hand side operator. Iterations of the right-hand side operator in the resulting equation

$$\Phi_1 = -\left(\Delta - \sum_\alpha \frac{1}{\lambda_{\mathrm{D}\alpha}^2}\right)^{-1}\left(4\pi\varrho_1 + \Phi_1 \sum_\alpha \frac{1}{\lambda_{\mathrm{D}\alpha}^2}\right) \tag{3.49}$$

should not result in large eigenvalues. However, this is reserved for future work, which will be necessary when treating the solution of the kinetic equation in realistic geometry. For now, we shall derive a quick solution in cylindrical geometry and ignore poloidal mode coupling. For the Fourier amplitudes, the Poisson equation reduces to a second-order ODE in r,

$$\frac{1}{r}\frac{\partial}{\partial r}\left(r\frac{\partial}{\partial r}\right)\Phi_m - \left(\frac{m^2}{r^2} + \frac{n^2}{R_0^2}\right)\Phi_m = 4\pi\left(\frac{B_m^r}{B_0} - \frac{\mathrm{i}k_\parallel}{E_{0r}}\Phi_m\right)\times \\ \times \sum_\alpha \frac{e_\alpha n_\alpha v_{T\alpha}}{\nu_\alpha}\left(\left(A_1^\alpha + A_2^\alpha\right) I^{01} + \frac{1}{2}A_2^\alpha I^{03}\right). \tag{3.50}$$

It is more convenient to replace the susceptibility functions I^{01} and I^{03} by I^{11} and I^{13} using (3.27) and (3.28) and their symmetry $I^{kl} = I^{lk}$ as follows,

$$I^{01} = -\frac{k_\parallel v_{T\alpha}}{\omega_E} I^{11}, \qquad I^{03} = -\frac{k_\parallel v_{T\alpha}}{\omega_E} I^{13}. \tag{3.51}$$

Thus we get

$$\frac{1}{r}\frac{\partial}{\partial r}\left(r\frac{\partial}{\partial r}\right)\Phi_m - \left(\frac{m^2}{r^2} + \frac{n^2}{R_0^2}\right)\Phi_m = -\frac{4\pi k_\parallel}{\omega_E}\left(\frac{B_m^r}{B_0} - \frac{\mathrm{i}k_\parallel}{E_{0r}}\Phi_m\right) F_m \tag{3.52}$$

with

$$F_m = \sum_\alpha \frac{e_\alpha n_\alpha v_{T\alpha}^2}{\nu_\alpha}\left(\left(A_1^\alpha + A_2^\alpha\right) I^{11} + \frac{1}{2}A_2^\alpha I^{13}\right). \tag{3.53}$$

The function F_m stays finite at the resonant surface where

$$I^{13} = 3I^{11} = \frac{3}{1 - \mathrm{i}x_2} \tag{3.54}$$

according to (A27) of [13].

We can now express the current density (3.21) via the function (3.53) too by using the recurrence relations (3.27) and (3.29) in the form

$$I^{10} = -\frac{k_\parallel v_{T\alpha}}{\omega_E} I^{11}, \qquad I^{12} = -\frac{k_\parallel v_{T\alpha}}{\omega_E} I^{13}. \tag{3.55}$$

Thus we obtain

$$J_{\parallel \boldsymbol{m}} = -\left(\frac{B^r_{\boldsymbol{m}}}{B_0} - \frac{\mathrm{i}k_\parallel}{E_{0r}} \Phi_{\boldsymbol{m}} \right) F_{\boldsymbol{m}}. \tag{3.56}$$

From this form of the parallel current density it is obvious that it is zero in case we ignore the Laplacian on the left-hand side of the Poisson equation (3.52). Actually, this Laplacian can also be strongly simplified taking into account that the radial derivatives of $\Phi_{\boldsymbol{m}}$ can be estimated as $\Phi_{\boldsymbol{m}}/\delta_{\boldsymbol{m}}$, i.e., they scale inversely with the small resonant layer width. Therefore, one can approximate the Laplacian in (3.52) as follows,

$$\frac{1}{r}\frac{\partial}{\partial r}\left(r \frac{\partial}{\partial r} \right) \Phi_{\boldsymbol{m}} - \left(\frac{m^2}{r^2} + \frac{n^2}{R_0^2} \right) \Phi_{\boldsymbol{m}} \approx \frac{\partial^2}{\partial r^2} \Phi_{\boldsymbol{m}}. \tag{3.57}$$

3.2 Phenomenological Account of Toroidal Geometry

Having derived an expression for the parallel current density in (3.56), we can use (2.125) to reconstruct the full helical current density. However,

$$\frac{J_{\parallel \boldsymbol{m}}}{B_0} = \left(\frac{J_{1\parallel}}{B_0} \right)_{\boldsymbol{m}} \tag{3.58}$$

holds in our straight-cylinder geometry, but not in toroidal geometry. In order to apply (3.58), we approximate the result for straight-cylinder geometry to get rid of any dependencies on θ. We divide the factor containing the misalignment potential in (3.56) by B_0 and rearrange it,

$$\frac{1}{B_0}\left(\frac{B^r_{\boldsymbol{m}}}{B_0} - \frac{\mathrm{i}k_\parallel \Phi_{\boldsymbol{m}}}{E_{0r}} \right) = \frac{B_0^\varphi}{B_0^2}\left(\frac{B^r_{\boldsymbol{m}}}{B_0^\varphi} - \frac{\mathrm{i}k_\parallel B_0 \Phi_{\boldsymbol{m}}}{B_0^\varphi E_{0r}} \right) = \frac{B_0^\varphi}{B_0^2}\left(\left(\frac{B_1^r}{B_0^\varphi} \right)_{\boldsymbol{m}} - \frac{1}{E_{0r}} \left(\frac{\boldsymbol{B}_0 \cdot \nabla \Phi_1}{B_0^\varphi} \right)_{\boldsymbol{m}} \right). \tag{3.59}$$

Note that we already used analogues of (3.58) in the last step. The last term in parentheses can be expanded in flux coordinates as

$$\frac{\boldsymbol{B}_0 \cdot \nabla \Phi_1}{B_0^\varphi} = \frac{1}{B_0^\varphi}\left(B_0^\vartheta \frac{\partial \Phi_1}{\partial \vartheta} + B_0^\varphi \frac{\partial \Phi_1}{\partial \varphi} \right) = \frac{1}{q}\frac{\partial \Phi_1}{\partial \vartheta} + \frac{\partial \Phi_1}{\partial \varphi}, \tag{3.60}$$

and, therefore,

$$\left(\frac{\boldsymbol{B}_0 \cdot \nabla \Phi_1}{B_0^\varphi} \right)_{\boldsymbol{m}} = \mathrm{i}\frac{m + nq}{q} \Phi_{\boldsymbol{m}}. \tag{3.61}$$

The covariant component E_{0r} is a flux function and, seeing how this also applies to $B_{0\varphi}$, we approximate $B_0^2 = B_{0\vartheta}B_0^\vartheta + B_{0\varphi}B_0^\varphi \approx B_{0\varphi}B_0^\varphi$, so we can write

$$\frac{B_0^\varphi}{B_0^2} \approx \frac{1}{B_{0\varphi}}. \tag{3.62}$$

Thus, the expression for the current density (3.56) takes the form

$$\left(\frac{J_{1\parallel}}{B_0}\right)_{\boldsymbol{m}} \approx -\frac{F_{\boldsymbol{m}}}{B_{0\varphi}}\left(\left(\frac{B_1^r}{B_0^\varphi}\right)_{\boldsymbol{m}} - \mathrm{i}\frac{m+nq}{qE_{0r}}\Phi_{\boldsymbol{m}}\right). \tag{3.63}$$

In order to interpret the function $F_{\boldsymbol{m}}$ in toroidal geometry, we notice that all the factors in (3.53) except for the susceptibility functions are flux functions. The argument x_2 is almost a flux function because

$$\omega_E = \frac{c\boldsymbol{k}\cdot\boldsymbol{E}_0\times\boldsymbol{B}_0}{B_0^2} = \frac{cE_{0r}}{\sqrt{g}B_0^2}\left(k_\vartheta B_{0\varphi} - k_\varphi B_{0\vartheta}\right) = \frac{cE_{0r}}{\sqrt{g}B_0^2}\left(mB_{0\varphi} - nB_{0\vartheta}\right), \tag{3.64}$$

where $\sqrt{g}$ is the Jacobian of (r,φ,ϑ) coordinates with a general radial coordinate r. In the vicinity of the resonance position, $m \approx -nq$, so we get

$$\omega_E \approx -\frac{cE_{0r}n}{\sqrt{g}B_0^2}\left(qB_{0\varphi} + B_{0\vartheta}\right) = -\frac{ncE_{0r}}{\sqrt{g}B_0^\vartheta} = -\frac{ncE_{0r}}{\frac{\partial\psi}{\partial r}} = -n\Omega_E. \tag{3.65}$$

Here, Ω_E is the toroidal $\boldsymbol{E}\times\boldsymbol{B}$ rotation frequency,

$$\Omega_E = c\frac{\partial\Phi_0}{\partial\psi}. \tag{3.66}$$

The only quantity where we need a forced interpretation is the argument x_1 containing $k_\parallel$, which we postulate to be the same as in the straight cylinder geometry,

$$k_\parallel = \frac{m+nq}{qR_0} \quad\rightarrow\quad x_1 = \frac{(m+nq)\,v_{T\alpha}}{qR_0\nu_\alpha}, \tag{3.67}$$

where R_0 is a reference major radius. Note that r is still a general radial variable, although it is convenient to use ψ, and we already inserted (1.7) above, but in principle any radial variable can be used as long as the thermodynamic forces in (3.2) are adapted to use the same variable.

For a more general interpretation of the Poisson equation (3.52), we proceed in a similar manner. Noting that

$$k_\parallel B_0 = \frac{m+nq}{q}B_0^\varphi, \tag{3.68}$$

we multiply this equation with $(B_0/B_0^\varphi)^2$ and obtain

$$\left(\left(\frac{B_0}{B_0^\varphi}\right)^2 \Delta\Phi_1\right)_m = -\frac{4\pi(m+nq)F_m}{q\omega_E}\left(\left(\frac{B_1^r}{B_0^\varphi}\right)_m - \mathrm{i}\frac{m+nq}{qE_{0r}}\Phi_m\right). \tag{3.69}$$

With a similar argument as above, we retain in the Laplacian only the largest term with the second derivative of Φ_1 over radius,

$$\Delta\Phi_1 = \frac{1}{\sqrt{g}}\frac{\partial}{\partial x^i}\left(\sqrt{g}g^{ij}\frac{\partial\Phi_1}{\partial x^j}\right) \approx g^{rr}\frac{\partial^2\Phi_1}{\partial r^2}, \tag{3.70}$$

and ignore poloidal mode coupling by replacing the factor

$$g^{rr}\left(\frac{B_0}{B_0^\varphi}\right)^2 \approx g^{rr}\frac{B_{0\varphi}}{B_0^\varphi} \tag{3.71}$$

with its average over the poloidal angle, indicated by $\langle\cdot\rangle_\theta$, and get

$$\left\langle g^{rr}\frac{B_{0\varphi}}{B_0^\varphi}\right\rangle_\theta \frac{\partial^2\Phi_m}{\partial r^2} = -\frac{4\pi(m+nq)F_m}{q\omega_E}\left(\left(\frac{B_1^r}{B_0^\varphi}\right)_m - \mathrm{i}\frac{m+nq}{qE_{0r}}\Phi_m\right). \tag{3.72}$$

Using for the symmetry flux coordinates $B_{0\varphi} = R^2B_0^\varphi$ and using the definition $g^{rr} = |\nabla r|^2$, we rewrite (3.52) as

$$\frac{\partial^2\Phi_m}{\partial r^2} = -\frac{4\pi(m+nq)F_m}{q\omega_E\left\langle R^2|\nabla r|^2\right\rangle_\theta}\left(\left(\frac{B_1^r}{B_0^\varphi}\right)_m - \mathrm{i}\frac{m+nq}{qE_{0r}}\Phi_m\right). \tag{3.73}$$

This second order ODE should be solved for Φ_m in the resonant layer with the boundary conditions of vanishing right-hand side outside the resonant layer.

3.3 Finite Larmor Radius Effects

For the following derivations, we stay in a straight cylinder geometry where the unperturbed motion is simple. In zeroth order, we take the Boltzmann distribution

$$f_{\mathrm{B}}^\alpha(r_{\mathrm{g}}, H) = \frac{n_\alpha(r_{\mathrm{g}})}{\left(2\pi m T_\alpha(r_{\mathrm{g}})\right)^{\frac{3}{2}}}\exp\left(\frac{e_\alpha\Phi_0(r_{\mathrm{g}}) - H}{T_\alpha(r_{\mathrm{g}})}\right), \tag{3.74}$$

where

$$H = \frac{m_\alpha \boldsymbol{v}^2}{2} + e_\alpha\Phi(\boldsymbol{r}) \tag{3.75}$$

is the total energy and

$$r_{\mathrm{g}} = r - \varrho^r = r - \frac{\boldsymbol{h} \times \boldsymbol{v} \cdot \nabla r}{\omega_{\mathrm{c}\alpha}} \tag{3.76}$$

is the guiding center radius computed in the unperturbed field with the cyclotron frequency

$$\omega_{\mathrm{c}\alpha} = \frac{e_\alpha B_0}{m_\alpha c}. \tag{3.77}$$

The Vlasov operator for the stationary electromagnetic field,

$$\hat{L}_{\mathrm{V}} = \boldsymbol{v} \cdot \nabla + \frac{e_\alpha}{m_\alpha}\left(-\nabla \Phi + \frac{1}{c}\boldsymbol{v} \times \boldsymbol{B}\right) \cdot \frac{\partial}{\partial \boldsymbol{v}}, \tag{3.78}$$

conserves total energy in any magnetic geometry, $\hat{L}_{\mathrm{V}} H = 0$. The unperturbed Vlasov operator

$$\hat{L}_{\mathrm{V}0} = \boldsymbol{v} \cdot \nabla + \frac{e_\alpha}{m_\alpha}\left(-\nabla \Phi_0 + \frac{1}{c}\boldsymbol{v} \times \boldsymbol{B}_0\right) \cdot \frac{\partial}{\partial \boldsymbol{v}}, \tag{3.79}$$

conserves the guiding center radius in the straight cylinder geometry, $\hat{L}_{\mathrm{V}0} r_{\mathrm{g}} = 0$. Introducing the perturbation of the Vlasov operator,

$$\delta\hat{L}_{\mathrm{V}} = \frac{e_\alpha}{m_\alpha}\left(-\nabla \delta\Phi + \frac{1}{c}\boldsymbol{v} \times \delta\boldsymbol{B}\right) \cdot \frac{\partial}{\partial \boldsymbol{v}}, \tag{3.80}$$

such that $\hat{L}_{\mathrm{V}} = \hat{L}_{\mathrm{V}0} + \delta\hat{L}_{\mathrm{V}}$, we look for the solution of the kinetic equation

$$\hat{L}_{\mathrm{V}} f^\alpha = \hat{L}_{\mathrm{C}} f^\alpha, \tag{3.81}$$

where $\hat{L}_{\mathrm{C}}$ is the Coulomb collision operator such that $\hat{L}_{\mathrm{C}} f_{\mathrm{B}}^\alpha = 0$, and

$$f^\alpha(\boldsymbol{r}, \boldsymbol{v}) = f_{\mathrm{B}}^\alpha(r_{\mathrm{g}}, H) + \delta f_\alpha(\boldsymbol{r}, \boldsymbol{v}). \tag{3.82}$$

Up to linear order in the perturbation we get,

$$\hat{L}_{\mathrm{V}0} \delta f^\alpha + \hat{L}_{\mathrm{V}} f_{\mathrm{B}}^\alpha = \hat{L}_{\mathrm{C}} \delta f^\alpha. \tag{3.83}$$

Given the previous definitions, we simplify the second term,

$$\hat{L}_{\mathrm{V}} f_{\mathrm{B}}^\alpha = \frac{\partial f_{\mathrm{B}}^\alpha}{\partial H}\hat{L}_{\mathrm{V}} H + \frac{\partial f_{\mathrm{B}}^\alpha}{\partial r_{\mathrm{g}}}\hat{L}_{\mathrm{V}} r_{\mathrm{g}} = \frac{\partial f_{\mathrm{B}}^\alpha}{\partial r_{\mathrm{g}}}\hat{L}_{\mathrm{V}} r_{\mathrm{g}} = \frac{\partial f_{\mathrm{B}}^\alpha}{\partial r_{\mathrm{g}}}\delta\hat{L}_{\mathrm{V}} r_{\mathrm{g}} = \left(A_1^\alpha + \frac{H - e_\alpha \Phi_0}{T_\alpha} A_2^\alpha\right) f_{\mathrm{B}}^\alpha \delta\hat{L}_{\mathrm{V}} r_{\mathrm{g}}, \tag{3.84}$$

and

$$\delta\hat{L}_{\mathrm{V}} r_{\mathrm{g}} = \frac{c\nabla r \times \boldsymbol{h} \cdot \nabla \delta\Phi}{B_0} + \frac{\delta\boldsymbol{B} \cdot \nabla r}{B_0} \boldsymbol{h} \cdot \boldsymbol{v} - \frac{\delta\boldsymbol{B} \cdot \boldsymbol{h}}{B_0} \boldsymbol{v} \cdot \nabla r. \tag{3.85}$$

We ignore the last term whose contribution to the gyroaverge is of the order of $\varrho_{\mathrm{L}\alpha} k_\perp \delta B^\parallel \ll \delta B^\perp$ compared to the previous one, where

$$\varrho_{\mathrm{L}\alpha} = \frac{v_{T\alpha}}{\omega_{\mathrm{c}\alpha}} \tag{3.86}$$

is the Larmor radius. This term, however may contribute significantly to the first cyclotron harmonic. We nevertheless ignore it assuming that its perturbation is of Alfvénic type, i.e., it is purely perpendicular, $\delta\boldsymbol{B} \cdot \boldsymbol{h} = 0$. Denoting the parallel velocity with respect to the unperturbed field as $\boldsymbol{h} \cdot \boldsymbol{v} = v_\parallel$, we get

$$\delta\hat{L}_{\mathrm{V}} r_{\mathrm{g}} \approx -\frac{\mathrm{i}ck_\perp \delta\Phi}{B_0} + \frac{\delta B^r}{B_0} v_\parallel = \frac{\delta B^r v_\parallel + c\delta E^\perp}{B_0}. \tag{3.87}$$

Thus we get the kinetic equation as

$$\left(\hat{L}_{\mathrm{V}0} - \hat{L}_{\mathrm{C}}\right) \delta f^\alpha = -\left(A_1^\alpha + \frac{H - e_\alpha \Phi_0}{T_\alpha} A_2^\alpha\right) f_{\mathrm{B}}^\alpha \frac{\delta B^r v_\parallel + c\delta E^\perp}{B_0}. \tag{3.88}$$

Here, we ignore the perturbation of the potential (leading to the quadratic correction) in the factor

$$\frac{H - e_\alpha \Phi_0}{T_\alpha} \approx \frac{H - e_\alpha \Phi}{T_\alpha} = \frac{m_\alpha \left(v_\perp^2 + v_\parallel^2\right)}{2T_\alpha} \tag{3.89}$$

as well as in the Boltzmann distribution, where we set $\Phi_0 \to \Phi$ so that it becomes a local Maxwellian, $f_{\mathrm{B}}^\alpha \to f_0^\alpha$. We further transform the uperturbed Vlasov operator to the guiding center variables,

$$\hat{L}_{\mathrm{V}0} \approx \left(v_\parallel \boldsymbol{h} + \boldsymbol{v}_E\right) \cdot \nabla_{\mathrm{g}} - \omega_{\mathrm{c}\alpha} \frac{\partial}{\partial\phi} = \mathrm{i}(k_\parallel v_\parallel + \omega_E) - \omega_{\mathrm{c}\alpha} \frac{\partial}{\partial\phi}. \tag{3.90}$$

Here, ∇_{g} denotes derivatives over the guiding center position. Also, we ignored the magnetic drift in the unperturbed field in favour of the elecric drift, as we did before.

Since we ignored the compressional perturbations by assuming $\delta\boldsymbol{B} \cdot \boldsymbol{h} = 0$, the main contribution comes from the zero cyclotron harmonic (gyroaverge) of the distribution function $\langle \delta f^\alpha \rangle_\phi$ descibed by the gyrokinetic equation

$$\left(\mathrm{i}(k_\parallel v_\parallel + \omega_E) - \hat{L}_{\mathrm{C}}\right) \langle \delta f^\alpha \rangle_\phi = -\left(A_1^\alpha + \frac{m_\alpha (v_\perp^2 + v_\parallel^2)}{2T_\alpha} A_2^\alpha\right) f_0^\alpha \frac{\langle \delta B^r \rangle_\phi v_\parallel + c\left\langle \delta E^\perp \right\rangle_\phi}{B_0}. \tag{3.91}$$

Except for gyroaveraging, this is the same equation as we solved before. We compute the gyroaverges of the perturbation field to the leading order, ignoring FLR corrections to the angles, e.g., for any a,

$$\begin{aligned}\left\langle a(r,\theta,z)\right\rangle_\phi \approx \left\langle a\left(r_\mathrm{g}-\varrho^r,\theta_\mathrm{g},z_\mathrm{g}\right)\right\rangle_\phi &\approx \left\langle\left(1+\frac{(\varrho^r)^2}{2}\frac{\partial^2}{\partial r_\mathrm{g}^2}\right)a(r_\mathrm{g},\theta_\mathrm{g},z_\mathrm{g})\right\rangle_\phi \\ &= \left(1+\frac{v_\perp^2}{4\omega_{\mathrm{c}\alpha}^2}\frac{\partial^2}{\partial r_\mathrm{g}^2}\right)a(r_\mathrm{g},\theta_\mathrm{g},z_\mathrm{g}). \end{aligned} \tag{3.92}$$

When computing the moments of $\langle\delta f^\alpha(r_\mathrm{g},\theta_\mathrm{g},z_\mathrm{g})\rangle_\phi$, we have to transform it back to actual positions (r,θ,z), which we do to the same accuracy in Larmor radius. So we get, e.g., for the density

$$\begin{aligned}\delta n_\alpha &= m_\alpha^3\int \mathrm{d}^3v\left\langle\delta f^\alpha(r_\mathrm{g},\theta_\mathrm{g},z_\mathrm{g})\right\rangle_\phi = m_\alpha^3\int \mathrm{d}^3v\left\langle\delta f^\alpha\left(r-\varrho^r,\theta-\varrho^\theta,z-\varrho^z\right)\right\rangle_\phi \\ &\approx m_\alpha^3\int \mathrm{d}^3v\left\langle\delta f^\alpha\left(r-\varrho^r,\theta,z\right)\right\rangle_\phi \approx m_\alpha^3\int \mathrm{d}^3v\left(1+\frac{\partial^2}{\partial r^2}\frac{v_\perp^2}{4\omega_{\mathrm{c}\alpha}^2}\right)\left\langle\delta f^\alpha(r,\theta,z)\right\rangle_\phi. \end{aligned} \tag{3.93}$$

If we ignore the FLR correction terms proportional to $v_\perp^2/\omega_{\mathrm{c}\alpha}^2$ in (3.92) and (3.93), we get the old results (3.19) and (3.20). *Note that here and in the following derivations, when we write*

$$\left(1+\frac{\partial^2}{\partial r^2}\frac{v_\perp^2}{4\omega_{\mathrm{c}\alpha}^2}\right), \tag{3.94}$$

the derivative is intended to act on the terms to the right of the closing parenthesis as well.

Note that the first order perturbation is contained not only in $\langle\delta f^\alpha\rangle_\phi$, but also in the Boltzmann distribution which we expand as

$$f_\mathrm{B}^\alpha \approx \left(1-\frac{e_\alpha\delta\Phi}{T_\alpha}\right)f_0^\alpha. \tag{3.95}$$

Here, the perturbation potential $\delta\Phi$ appears as is, without gyroaveraging so that the last term in (3.20) stays the same even if FLR efects are taken into account. Thus, a complete first order perturbation of the distribution function is

$$f_1^\alpha(r,\theta,z) = \left\langle\delta f^\alpha(r_\mathrm{g},\theta,z)\right\rangle_\phi - \frac{e_\alpha\delta\Phi(r,\theta,z)}{T_\alpha}f_0^\alpha. \tag{3.96}$$

Assuming as before that perturbations are given as a single Fourier harmonic,

$$f_1^\alpha(r,\theta,z) = f_{1,\boldsymbol{m}}^\alpha(r)\mathrm{e}^{\mathrm{i}m\theta+\mathrm{i}k_z z}, \tag{3.97}$$

$$\left\langle\delta f^\alpha\right\rangle_\phi(r_\mathrm{g},\theta,z) = f_{\boldsymbol{m}}^\alpha(r_\mathrm{g})\mathrm{e}^{\mathrm{i}m\theta+\mathrm{i}k_z z}, \tag{3.98}$$

$$\delta\Phi(r,\theta,z) = \Phi_{\boldsymbol{m}}(r)\mathrm{e}^{\mathrm{i}m\theta+\mathrm{i}k_z z}, \tag{3.99}$$

the Fourier amplitude of the complete first order perturbation of the distribution function (3.13) is modified by FLR effects to

$$f^{\alpha}_{1,m}(r) = f^{\alpha}_{m}(r_{\mathrm{g}}) - \frac{e_\alpha \Phi_m(r)}{T_\alpha} f^{\alpha}_0. \tag{3.100}$$

Formally, this expression is the same as (3.13), except that we distinguish now the guiding center radius r_{g} from the actual radius r (but we ignore this difference in the angles θ and z). When computing the moments of the first term $f^{\alpha}_{m}(r_{\mathrm{g}})$, we have to transform it back to the actual position r, which we do to the same accuracy in Larmor radius as we did for the gyroaverges. Thus, for the charge density perturbation we get

$$\begin{aligned}
\varrho_m &= \sum_\alpha e_\alpha \int \mathrm{d}^3p\, f^{\alpha}_{1,m}(r) = \sum_\alpha e_\alpha \int \mathrm{d}^3p\, f^{\alpha}_{m}(r_{\mathrm{g}}) - \sum_\alpha \frac{e_\alpha^2 n_\alpha}{T_\alpha}\Phi_m(r) \\
&= \sum_\alpha e_\alpha \int \mathrm{d}^3p\, f^{\alpha}_{m}\left(r - \varrho^r\right) - \sum_\alpha \frac{e_\alpha^2 n_\alpha}{T_\alpha}\Phi_m(r) \\
&\approx \sum_\alpha e_\alpha \int \mathrm{d}^3p \left(1 + \frac{\left(\varrho^r\right)^2}{2}\frac{\partial^2}{\partial r^2}\right) f^{\alpha}_{m}(r) - \sum_\alpha \frac{e_\alpha^2 n_\alpha}{T_\alpha}\Phi_m(r) \\
&= \sum_\alpha e_\alpha \int \mathrm{d}^3p \left(1 + \frac{\partial^2}{\partial r^2}\frac{v_\perp^2}{4\omega_{\mathrm{c}\alpha}^2}\right) f^{\alpha}_{m}(r) - \sum_\alpha \frac{e_\alpha^2 n_\alpha}{T_\alpha}\Phi_m(r).
\end{aligned} \tag{3.101}$$

Similarly, for the parallel current density perturbation we get

$$\begin{aligned}
J_{\parallel m} &= \sum_\alpha e_\alpha \int \mathrm{d}^3p\, v_\parallel f^{\alpha}_{1,m}(r) = \sum_\alpha e_\alpha \int \mathrm{d}^3p\, v_\parallel f^{\alpha}_{m}(r_{\mathrm{g}}) \\
&= \sum_\alpha e_\alpha \int \mathrm{d}^3p \left(1 + \frac{\partial^2}{\partial r^2}\frac{v_\perp^2}{4\omega_{\mathrm{c}\alpha}^2}\right) v_\parallel f^{\alpha}_{m}(r).
\end{aligned} \tag{3.102}$$

We express the solution of the gyrokinetic equation (3.91) in terms of Green's functions as before,

$$\begin{aligned}
f^{\alpha}_{m}(r_{\mathrm{g}}) &= -\int_{-\infty}^{\infty} \mathrm{d}v'_\parallel\, G_m(v_\parallel, v'_\parallel) \left(A^\alpha_1 + \frac{m_\alpha\left(v_\perp^2 + {v'_\parallel}^2\right)}{2T_\alpha} A^\alpha_2\right) f^{\alpha}_0(v_\perp, v'_\parallel) \times \\
&\quad \times \left(\frac{v'_\parallel}{B_0}\left\langle B^r_m\right\rangle_\phi + \frac{c}{B_0}\left\langle E_{\perp m}\right\rangle_\phi\right) \\
&\approx -\int_{-\infty}^{\infty} \mathrm{d}v'_\parallel\, G_m(v_\parallel, v'_\parallel) \left(A^\alpha_1 + \frac{m_\alpha\left(v_\perp^2 + {v'_\parallel}^2\right)}{2T_\alpha} A^\alpha_2\right) f^{\alpha}_0(v_\perp, v'_\parallel) \times \\
&\quad \times \frac{1}{B_0}\left(1 + \frac{v_\perp^2}{4\omega_{\mathrm{c}\alpha}^2}\frac{\partial^2}{\partial r_{\mathrm{g}}^2}\right)\left(v'_\parallel B^r_m(r_{\mathrm{g}}) + cE_{\perp m}(r_{\mathrm{g}})\right),
\end{aligned} \tag{3.103}$$

where we substituted the FLR expansion (3.92) for gyroaverages. Substituting (3.103) in the

charge density perturbation (3.101) we get

$$
\begin{aligned}
&\varrho_{\boldsymbol{m}} + \sum_{\alpha} \frac{e_\alpha^2 n_\alpha}{T_\alpha} \Phi_{\boldsymbol{m}}(r) = \sum_{\alpha} e_\alpha \int \mathrm{d}^3 p \left(1 + \frac{\partial^2}{\partial r^2} \frac{v_\perp^2}{4\omega_{\mathrm{c}\alpha}^2}\right) f_{\boldsymbol{m}}^\alpha(r) \\
&\quad = 2\pi \sum_{\alpha} e_\alpha m_\alpha^3 \int\limits_0^\infty \mathrm{d}v_\perp \, v_\perp \int\limits_{-\infty}^\infty \mathrm{d}v_\parallel \left(1 + \frac{\partial^2}{\partial r^2} \frac{v_\perp^2}{4\omega_{\mathrm{c}\alpha}^2}\right) f_{\boldsymbol{m}}^\alpha(r) \\
&\quad = -2\pi \sum_{\alpha} e_\alpha m_\alpha^3 \int\limits_0^\infty \mathrm{d}v_\perp \, v_\perp \int\limits_{-\infty}^\infty \mathrm{d}v_\parallel \left(1 + \frac{\partial^2}{\partial r^2} \frac{v_\perp^2}{4\omega_{\mathrm{c}\alpha}^2}\right) \frac{1}{B_0} \int\limits_{-\infty}^\infty \mathrm{d}v'_\parallel \, G_{\boldsymbol{m}}(v_\parallel, v'_\parallel) \times \\
&\qquad \times \left(A_1^\alpha + \frac{m_\alpha \left(v_\perp^2 + v_\parallel'^2\right)}{2T_\alpha} A_2^\alpha\right) f_0^\alpha(v_\perp, v'_\parallel) \left(1 + \frac{v_\perp^2}{4\omega_{\mathrm{c}\alpha}^2} \frac{\partial^2}{\partial r^2}\right) \left(v'_\parallel B_{\boldsymbol{m}}^r(r) + cE_{\perp \boldsymbol{m}}(r)\right) \\
&\quad = -\sum_{\alpha} e_\alpha \int\limits_0^\infty \mathrm{d}v_\perp \, v_\perp \int\limits_{-\infty}^\infty \mathrm{d}v_\parallel \left(1 + \frac{\partial^2}{\partial r^2} \frac{v_\perp^2}{4\omega_{\mathrm{c}\alpha}^2}\right) \frac{n_\alpha}{\sqrt{2\pi} v_{T\alpha}^3 B_0} \exp\left(-\frac{v_\perp^2}{2v_{T\alpha}^2}\right) \int\limits_{-\infty}^\infty \mathrm{d}v'_\parallel \, G_{\boldsymbol{m}}(v_\parallel, v'_\parallel) \times \\
&\qquad \times \left(A_1^\alpha + \frac{m_\alpha \left(v_\perp^2 + v_\parallel'^2\right)}{2T_\alpha} A_2^\alpha\right) \exp\left(-\frac{v_\parallel'^2}{2v_{T\alpha}^2}\right) \left(1 + \frac{v_\perp^2}{4\omega_{\mathrm{c}\alpha}^2} \frac{\partial^2}{\partial r^2}\right) \left(v'_\parallel B_{\boldsymbol{m}}^r(r) + cE_{\perp \boldsymbol{m}}(r)\right) \\
&\quad \approx -\sum_{\alpha} e_\alpha \int\limits_0^\infty \mathrm{d}v_\perp \, v_\perp \int\limits_{-\infty}^\infty \mathrm{d}v_\parallel \frac{n_\alpha}{\sqrt{2\pi} v_{T\alpha}^3 B_0} \exp\left(-\frac{v_\perp^2}{2v_{T\alpha}^2}\right) \int\limits_{-\infty}^\infty \mathrm{d}v'_\parallel \, G_{\boldsymbol{m}}(v_\parallel, v'_\parallel) \times \\
&\qquad \times \left(A_1^\alpha + \frac{m_\alpha \left(v_\perp^2 + v_\parallel'^2\right)}{2T_\alpha} A_2^\alpha\right) \exp\left(-\frac{v_\parallel'^2}{2v_{T\alpha}^2}\right) \left(v'_\parallel B_{\boldsymbol{m}}^r(r) + cE_{\perp \boldsymbol{m}}(r)\right) - \\
&\qquad - \frac{\partial^2}{\partial r^2} \sum_{\alpha} e_\alpha \int\limits_0^\infty \mathrm{d}v_\perp \, v_\perp \int\limits_{-\infty}^\infty \mathrm{d}v_\parallel \frac{v_\perp^2}{4\omega_{\mathrm{c}\alpha}^2} \frac{n_\alpha}{\sqrt{2\pi} v_{T\alpha}^3 B_0} \exp\left(-\frac{v_\perp^2}{2v_{T\alpha}^2}\right) \int\limits_{-\infty}^\infty \mathrm{d}v'_\parallel \, G_{\boldsymbol{m}}(v_\parallel, v'_\parallel) \times \\
&\qquad \times \left(A_1^\alpha + \frac{m_\alpha \left(v_\perp^2 + v_\parallel'^2\right)}{2T_\alpha} A_2^\alpha\right) \exp\left(-\frac{v_\parallel'^2}{2v_{T\alpha}^2}\right) \left(v'_\parallel B_{\boldsymbol{m}}^r(r) + cE_{\perp \boldsymbol{m}}(r)\right) - \\
&\qquad - \sum_{\alpha} e_\alpha \int\limits_0^\infty \mathrm{d}v_\perp \, v_\perp \int\limits_{-\infty}^\infty \mathrm{d}v_\parallel \frac{v_\perp^2}{4\omega_{\mathrm{c}\alpha}^2} \frac{n_\alpha}{\sqrt{2\pi} v_{T\alpha}^3 B_0} \exp\left(-\frac{v_\perp^2}{2v_{T\alpha}^2}\right) \int\limits_{-\infty}^\infty \mathrm{d}v'_\parallel \, G_{\boldsymbol{m}}(v_\parallel, v'_\parallel) \times \\
&\qquad \times \left(A_1^\alpha + \frac{m_\alpha \left(v_\perp^2 + v_\parallel'^2\right)}{2T_\alpha} A_2^\alpha\right) \exp\left(-\frac{v_\parallel'^2}{2v_{T\alpha}^2}\right) \frac{\partial^2}{\partial r^2} \left(v'_\parallel B_{\boldsymbol{m}}^r(r) + cE_{\perp \boldsymbol{m}}(r)\right),
\end{aligned}
$$

where we retained in the last expression only the lowest order non-vanishing correction in Larmor radius which scales as $v_\perp^2/\omega_{\mathrm{c}\alpha}^2$ and, respectively, ignored the fourth derivative over radius keeping only the second derivatives. Evaluating the integrals over $v_\perp$, we get

$$
\varrho_{\boldsymbol{m}} + \sum_{\alpha} \frac{e_\alpha^2 n_\alpha}{T_\alpha} \Phi_{\boldsymbol{m}}(r)
$$

$$
\begin{aligned}
&= -\sum_\alpha \frac{e_\alpha n_\alpha}{\sqrt{2\pi} v_{T\alpha} B_0} \int_{-\infty}^{\infty} \mathrm{d}v_\parallel \int_{-\infty}^{\infty} \mathrm{d}v'_\parallel \, G_{\boldsymbol{m}}(v_\parallel, v'_\parallel) \times \\
&\times \left(A_1^\alpha + A_2^\alpha + \frac{{v'_\parallel}^2}{2v_{T\alpha}^2} A_2^\alpha \right) \exp\left(-\frac{{v'_\parallel}^2}{2v_{T\alpha}^2} \right) \left(v'_\parallel B^r_{\boldsymbol{m}}(r) + cE_{\perp \boldsymbol{m}}(r) \right) - \\
&- \frac{\partial^2}{\partial r^2} \sum_\alpha \frac{e_\alpha n_\alpha \varrho_{\mathrm{L}\alpha}^2}{2\sqrt{2\pi} v_{T\alpha} B_0} \int_{-\infty}^{\infty} \mathrm{d}v_\parallel \int_{-\infty}^{\infty} \mathrm{d}v'_\parallel \, G_{\boldsymbol{m}}(v_\parallel, v'_\parallel) \times \\
&\times \left(A_1^\alpha + 2A_2^\alpha + \frac{{v'_\parallel}^2}{2v_{T\alpha}^2} A_2^\alpha \right) \exp\left(-\frac{{v'_\parallel}^2}{2v_{T\alpha}^2} \right) \left(v'_\parallel B^r_{\boldsymbol{m}}(r) + cE_{\perp \boldsymbol{m}}(r) \right) - \\
&- \sum_\alpha \frac{e_\alpha n_\alpha \varrho_{\mathrm{L}\alpha}^2}{2\sqrt{2\pi} v_{T\alpha} B_0} \int_{-\infty}^{\infty} \mathrm{d}v_\parallel \int_{-\infty}^{\infty} \mathrm{d}v'_\parallel \, G_{\boldsymbol{m}}(v_\parallel, v'_\parallel) \times \\
&\times \left(A_1^\alpha + 2A_2^\alpha + \frac{{v'_\parallel}^2}{2v_{T\alpha}^2} A_2^\alpha \right) \exp\left(-\frac{{v'_\parallel}^2}{2v_{T\alpha}^2} \right) \frac{\partial^2}{\partial r^2} \left(v'_\parallel B^r_{\boldsymbol{m}}(r) + cE_{\perp \boldsymbol{m}}(r) \right). \qquad (3.104)
\end{aligned}
$$

Note that if we set $\varrho_{\mathrm{L}\alpha} = 0$ in this expression, we recover the old result (3.20). Expressing the double integrals via susceptibility functions, this perturbation of charge density is

$$
\begin{aligned}
\varrho_{\boldsymbol{m}} + \sum_\alpha \frac{e_\alpha^2 n_\alpha}{T_\alpha} \Phi_{\boldsymbol{m}}(r) = &- \sum_\alpha \frac{e_\alpha n_\alpha}{\nu_\alpha B_0} \left[\left(\left(A_1^\alpha + A_2^\alpha \right) I^{01} + \frac{1}{2} A_2^\alpha I^{03} \right) v_{T\alpha} B^r_{\boldsymbol{m}} + \right. \\
&\left. + \left(\left(A_1^\alpha + A_2^\alpha \right) I^{00} + \frac{1}{2} A_2^\alpha I^{02} \right) cE_{\perp \boldsymbol{m}} \right] - \\
&- \frac{\partial^2}{\partial r^2} \sum_\alpha \frac{e_\alpha n_\alpha \varrho_{\mathrm{L}\alpha}^2}{2\nu_\alpha B_0} \left[\left(\left(A_1^\alpha + 2A_2^\alpha \right) I^{01} + \frac{1}{2} A_2^\alpha I^{03} \right) v_{T\alpha} B^r_{\boldsymbol{m}} + \right. \\
&\left. + \left(\left(A_1^\alpha + 2A_2^\alpha \right) I^{00} + \frac{1}{2} A_2^\alpha I^{02} \right) cE_{\perp \boldsymbol{m}} \right] - \\
&- \sum_\alpha \frac{e_\alpha n_\alpha \varrho_{\mathrm{L}\alpha}^2}{2\nu_\alpha B_0} \left[\left(\left(A_1^\alpha + 2A_2^\alpha \right) I^{01} + \frac{1}{2} A_2^\alpha I^{03} \right) v_{T\alpha} \frac{\partial^2}{\partial r^2} B^r_{\boldsymbol{m}} + \right. \\
&\left. + \left(\left(A_1^\alpha + 2A_2^\alpha \right) I^{00} + \frac{1}{2} A_2^\alpha I^{02} \right) c \frac{\partial^2}{\partial r^2} E_{\perp \boldsymbol{m}} \right]. \qquad (3.105)
\end{aligned}
$$

Similarly, we obtain the parallel current density perturbation as

$$
\begin{aligned}
J_{\parallel \boldsymbol{m}} = &- \sum_\alpha \frac{e_\alpha n_\alpha v_{T\alpha}}{\nu_\alpha B_0} \left[\left(\left(A_1^\alpha + A_2^\alpha \right) I^{11} + \frac{1}{2} A_2^\alpha I^{13} \right) v_{T\alpha} B^r_{\boldsymbol{m}} + \right. \\
&\left. + \left(\left(A_1^\alpha + A_2^\alpha \right) I^{10} + \frac{1}{2} A_2^\alpha I^{12} \right) cE_{\perp \boldsymbol{m}} \right] - \\
&- \frac{\partial^2}{\partial r^2} \sum_\alpha \frac{e_\alpha n_\alpha v_{T\alpha} \varrho_{\mathrm{L}\alpha}^2}{2\nu_\alpha B_0} \left[\left(\left(A_1^\alpha + 2A_2^\alpha \right) I^{11} + \frac{1}{2} A_2^\alpha I^{13} \right) v_{T\alpha} B^r_{\boldsymbol{m}} + \right.
\end{aligned}
$$

$$+\left(\left(A_1^\alpha+2A_2^\alpha\right)I^{10}+\frac{1}{2}A_2^\alpha I^{12}\right)cE_{\perp m}\Bigg]-$$
$$-\sum_\alpha\frac{e_\alpha n_\alpha v_{T\alpha}\varrho_{\mathrm{L}\alpha}^2}{2\nu_\alpha B_0}\left[\left(\left(A_1^\alpha+2A_2^\alpha\right)I^{11}+\frac{1}{2}A_2^\alpha I^{13}\right)v_{T\alpha}\frac{\partial^2}{\partial r^2}B_m^r+\right.$$
$$\left.+\left(\left(A_1^\alpha+2A_2^\alpha\right)I^{10}+\frac{1}{2}A_2^\alpha I^{12}\right)c\frac{\partial^2}{\partial r^2}E_{\perp m}\right]. \tag{3.106}$$

Now, we repeat the transformations from previous sections for the newly derived FLR terms. First, we transform the charge density perturbation (3.105) using the recurrence relations (3.26) and (3.28) to express I^{00} and I^{02} as follows

$$I^{00}=\frac{x_1I^{10}+\mathrm{i}}{x_2}=-\frac{k_\parallel v_{T\alpha}}{\omega_E}I^{10}+\frac{\mathrm{i}\nu_\alpha}{\omega_E},\qquad I^{02}=\frac{x_1I^{12}+\mathrm{i}}{x_2}=-\frac{k_\parallel v_{T\alpha}}{\omega_E}I^{12}+\frac{\mathrm{i}\nu_\alpha}{\omega_E}. \tag{3.107}$$

Using (3.6) and treating as constant all functions of radius except Φ_m, B_m^r and $k_\parallel$, we get

$$\begin{aligned}
&\varrho_m+\sum_\alpha\frac{e_\alpha^2n_\alpha}{T_\alpha}\Phi_m(r)\\
&\quad=-\sum_\alpha\frac{e_\alpha n_\alpha v_{T\alpha}}{\nu_\alpha}\left((A_1^\alpha+A_2^\alpha)I^{01}+\frac{1}{2}A_2^\alpha I^{03}\right)\left(\frac{B_m^r}{B_0}-\frac{\mathrm{i}k_\parallel\Phi_m}{E_{0r}}\right)-\\
&\quad-\sum_\alpha\frac{e_\alpha n_\alpha}{E_{0r}}\left(A_1^\alpha+\frac{3}{2}A_2^\alpha\right)\Phi_m-\\
&\quad-\frac{\partial^2}{\partial r^2}\sum_\alpha\frac{e_\alpha n_\alpha v_{T\alpha}\varrho_{\mathrm{L}\alpha}^2}{2\nu_\alpha}\left((A_1^\alpha+2A_2^\alpha)I^{01}+\frac{1}{2}A_2^\alpha I^{03}\right)\left(\frac{B_m^r}{B_0}-\frac{\mathrm{i}k_\parallel\Phi_m}{E_{0r}}\right)-\\
&\quad-\frac{\partial^2}{\partial r^2}\sum_\alpha\frac{e_\alpha n_\alpha\varrho_{\mathrm{L}\alpha}^2}{2E_{0r}}\left(A_1^\alpha+\frac{5}{2}A_2^\alpha\right)\Phi_m-\\
&\quad-\sum_\alpha\frac{e_\alpha n_\alpha v_{T\alpha}\varrho_{\mathrm{L}\alpha}^2}{2\nu_\alpha}\left((A_1^\alpha+2A_2^\alpha)I^{01}+\frac{1}{2}A_2^\alpha I^{03}\right)\left(\frac{\partial^2}{\partial r^2}\frac{B_m^r}{B_0}-\frac{\mathrm{i}k_\parallel}{E_{0r}}\frac{\partial^2}{\partial r^2}\Phi_m\right)-\\
&\quad-\sum_\alpha\frac{e_\alpha n_\alpha\varrho_{\mathrm{L}\alpha}^2}{2E_{0r}}\left(A_1^\alpha+\frac{5}{2}A_2^\alpha\right)\frac{\partial^2}{\partial r^2}\Phi_m.
\end{aligned}$$

As we have already shown previously via (3.30), the second term in the first line is cancelled by the expression in the third line.

$$\begin{aligned}
\varrho_m=&-\sum_\alpha\frac{e_\alpha n_\alpha v_{T\alpha}}{\nu_\alpha}\left((A_1^\alpha+A_2^\alpha)I^{01}+\frac{1}{2}A_2^\alpha I^{03}\right)\left(\frac{B_m^r}{B_0}-\frac{\mathrm{i}k_\parallel\Phi_m}{E_{0r}}\right)-\\
&-\frac{\partial^2}{\partial r^2}\sum_\alpha\frac{e_\alpha n_\alpha v_{T\alpha}\varrho_{\mathrm{L}\alpha}^2}{2\nu_\alpha}\left((A_1^\alpha+2A_2^\alpha)I^{01}+\frac{1}{2}A_2^\alpha I^{03}\right)\left(\frac{B_m^r}{B_0}-\frac{\mathrm{i}k_\parallel\Phi_m}{E_{0r}}\right)-\\
&-\sum_\alpha\frac{e_\alpha n_\alpha v_{T\alpha}\varrho_{\mathrm{L}\alpha}^2}{2\nu_\alpha}\left((A_1^\alpha+2A_2^\alpha)I^{01}+\frac{1}{2}A_2^\alpha I^{03}\right)\left(\frac{\partial^2}{\partial r^2}\frac{B_m^r}{B_0}-\frac{\mathrm{i}k_\parallel}{E_{0r}}\frac{\partial^2}{\partial r^2}\Phi_m\right)-\\
&-\frac{\partial^2}{\partial r^2}\sum_\alpha\frac{e_\alpha n_\alpha\varrho_{\mathrm{L}\alpha}^2}{2E_{0r}}\left(A_1^\alpha+\frac{5}{2}A_2^\alpha\right)\Phi_m-\sum_\alpha\frac{e_\alpha n_\alpha\varrho_{\mathrm{L}\alpha}^2}{2E_{0r}}\left(A_1^\alpha+\frac{5}{2}A_2^\alpha\right)\frac{\partial^2}{\partial r^2}\Phi_m.
\end{aligned} \tag{3.108}$$

In the zero Larmor radius limit where only the first line is retained, this expression coincides with (3.32). Using now relations (3.51) we can express charge density (3.108) via susceptibility functions I^{11} and I^{13} which stay finite at the resonant surface and decay as $1/k_\parallel^2$ away from it,

$$\begin{aligned}\varrho_{\boldsymbol{m}} = {}& \frac{k_\parallel}{\omega_E}\sum_\alpha \frac{e_\alpha n_\alpha v_{T\alpha}^2}{\nu_\alpha}\left((A_1^\alpha + A_2^\alpha)I^{11} + \frac{1}{2}A_2^\alpha I^{13}\right)\left(\frac{B_{\boldsymbol{m}}^r}{B_0} - \frac{\mathrm{i}k_\parallel \Phi_{\boldsymbol{m}}}{E_{0r}}\right) + \\ &+ \frac{\partial^2}{\partial r^2}\frac{k_\parallel}{\omega_E}\sum_\alpha \frac{e_\alpha n_\alpha v_{T\alpha}^2 \varrho_{\mathrm{L}\alpha}^2}{2\nu_\alpha}\left((A_1^\alpha + 2A_2^\alpha)I^{11} + \frac{1}{2}A_2^\alpha I^{13}\right)\left(\frac{B_{\boldsymbol{m}}^r}{B_0} - \frac{\mathrm{i}k_\parallel \Phi_{\boldsymbol{m}}}{E_{0r}}\right) + \\ &+ \frac{k_\parallel}{\omega_E}\sum_\alpha \frac{e_\alpha n_\alpha v_{T\alpha}^2 \varrho_{\mathrm{L}\alpha}^2}{2\nu_\alpha}\left((A_1^\alpha + 2A_2^\alpha)I^{11} + \frac{1}{2}A_2^\alpha I^{13}\right)\left(\frac{\partial^2}{\partial r^2}\frac{B_{\boldsymbol{m}}^r}{B_0} - \frac{\mathrm{i}k_\parallel}{E_{0r}}\frac{\partial^2}{\partial r^2}\Phi_{\boldsymbol{m}}\right) - \\ &- \frac{\partial^2}{\partial r^2}\sum_\alpha \frac{e_\alpha n_\alpha \varrho_{\mathrm{L}\alpha}^2}{2E_{0r}}\left(A_1^\alpha + \frac{5}{2}A_2^\alpha\right)\Phi_{\boldsymbol{m}} - \sum_\alpha \frac{e_\alpha n_\alpha \varrho_{\mathrm{L}\alpha}^2}{2E_{0r}}\left(A_1^\alpha + \frac{5}{2}A_2^\alpha\right)\frac{\partial^2}{\partial r^2}\Phi_{\boldsymbol{m}}. \end{aligned} \tag{3.109}$$

The parallel current density (3.106) is expressed via functions I^{11} and I^{13} in a similar manner,

$$\begin{aligned}J_{\parallel\boldsymbol{m}} = {}& -\sum_\alpha \frac{e_\alpha n_\alpha v_{T\alpha}^2}{\nu_\alpha}\left(\left(A_1^\alpha + A_2^\alpha\right)I^{11} + \frac{1}{2}A_2^\alpha I^{13}\right)\left(\frac{B_{\boldsymbol{m}}^r}{B_0} - \frac{\mathrm{i}k_\parallel \Phi_{\boldsymbol{m}}}{E_{0r}}\right) - \\ &- \frac{\partial^2}{\partial r^2}\sum_\alpha \frac{e_\alpha n_\alpha v_{T\alpha}^2 \varrho_{\mathrm{L}\alpha}^2}{2\nu_\alpha}\left(\left(A_1^\alpha + 2A_2^\alpha\right)I^{11} + \frac{1}{2}A_2^\alpha I^{13}\right)\left(\frac{B_{\boldsymbol{m}}^r}{B_0} - \frac{\mathrm{i}k_\parallel \Phi_{\boldsymbol{m}}}{E_{0r}}\right) - \\ &- \sum_\alpha \frac{e_\alpha n_\alpha v_{T\alpha}^2 \varrho_{\mathrm{L}\alpha}^2}{2\nu_\alpha}\left(\left(A_1^\alpha + 2A_2^\alpha\right)I^{11} + \frac{1}{2}A_2^\alpha I^{13}\right)\left(\frac{\partial^2}{\partial r^2}\frac{B_{\boldsymbol{m}}^r}{B_0} - \frac{\mathrm{i}k_\parallel}{E_{0r}}\frac{\partial^2}{\partial r^2}\Phi_{\boldsymbol{m}}\right). \end{aligned} \tag{3.110}$$

For a more compact notation, we introduce

$$G_{\boldsymbol{m}} = \sum_\alpha \frac{e_\alpha n_\alpha v_{T\alpha}^2 \varrho_{\mathrm{L}\alpha}^2}{2\nu_\alpha}\left((A_1^\alpha + 2A_2^\alpha)I^{11} + \frac{1}{2}A_2^\alpha I^{13}\right), \tag{3.111}$$

which should not be confused with the Green's function of (3.13). We furthermore use the *perpendicular fluid velocity* given by (13) of [13],

$$V_{\alpha\perp} = \frac{c}{e_\alpha n_\alpha B_0}\frac{\partial(n_\alpha T_\alpha)}{\partial r} - \frac{cE_{0r}}{B_0} = \frac{cT_\alpha}{e_\alpha B_0}\left(A_1^\alpha + \frac{5}{2}A_2^\alpha\right), \tag{3.112}$$

as well as (3.12) and (3.38), to rewrite the coefficient in the last two terms in (3.108) succinctly as

$$H = -\sum_\alpha \frac{e_\alpha n_\alpha \varrho_{\mathrm{L}\alpha}^2}{2E_{0r}}\left(A_1^\alpha + \frac{5}{2}A_2^\alpha\right) = \frac{1}{8\pi}\sum_\alpha \frac{\varrho_{\mathrm{L}\alpha}^2 V_{\alpha\perp}}{\lambda_{\mathrm{D}\alpha}^2 v_E}, \tag{3.113}$$

which in turn should not be confused with the total energy in the Boltzmann distribution (3.74). With (3.53), (3.111), and (3.113), the perturbations of charge density and current density can

be compactly written as

$$\varrho_m = \frac{k_\parallel}{\omega_E} F_m \left(\frac{B^r_m}{B_0} - \frac{\mathrm{i}k_\parallel \Phi_m}{E_{0r}} \right) + \frac{\partial^2}{\partial r^2} \frac{k_\parallel}{\omega_E} G_m \left(\frac{B^r_m}{B_0} - \frac{\mathrm{i}k_\parallel \Phi_m}{E_{0r}} \right) + \\ + \frac{k_\parallel}{\omega_E} G_m \left(\frac{\partial^2}{\partial r^2} \frac{B^r_m}{B_0} - \frac{\mathrm{i}k_\parallel}{E_{0r}} \frac{\partial^2}{\partial r^2} \Phi_m \right) + \frac{\partial^2}{\partial r^2} H \Phi_m + H \frac{\partial^2}{\partial r^2} \Phi_m, \tag{3.114}$$

$$J_{\parallel m} = -F_m \left(\frac{B^r_m}{B_0} - \frac{\mathrm{i}k_\parallel \Phi_m}{E_{0r}} \right) - \frac{\partial^2}{\partial r^2} G_m \left(\frac{B^r_m}{B_0} - \frac{\mathrm{i}k_\parallel \Phi_m}{E_{0r}} \right) - \\ - G_m \left(\frac{\partial^2}{\partial r^2} \frac{B^r_m}{B_0} - \frac{\mathrm{i}k_\parallel}{E_{0r}} \frac{\partial^2}{\partial r^2} \Phi_m \right). \tag{3.115}$$

In the limit of vanishing Larmor radius, $\varrho_{\mathrm{L}\alpha} \to 0$, we have $G_m \to 0$ and $H \to 0$. Thus only the first terms on the right-hand sides of (3.114) and (3.115) remain, and these expressions are reduced to (3.52) and (3.56), respectively.

3.3.1 Repeating Recurrence Relations and Limiting Cases

Now we check the perturbation of charge density (3.114) far away from the resonant surface in the collisionless case where $z_\alpha \ll 1$. We retain the first-order correction in z_α to the susceptibility functions in (A22) of [13], resulting in the approximation

$$I^{11} \approx -\frac{\mathrm{i}x_2}{x_1^2} + \sqrt{\frac{\pi}{2}} \frac{x_2^2}{|x_1|^3}, \qquad I^{31} \approx -\frac{\mathrm{i}x_2}{x_1^2}. \tag{3.116}$$

For the term involving F_m, we retain only the leading order in I^{11},

$$\frac{\mathrm{i}k_\parallel^2}{\omega_E E_{0r}} F_m \approx \frac{k_\parallel^2}{\omega_E E_{0r}} \sum_\alpha \frac{e_\alpha n_\alpha v_{T\alpha}^2}{\nu_\alpha} \frac{x_2}{x_1^2} \left(A_1^\alpha + \frac{3}{2} A_2^\alpha \right) = -\sum_\alpha \frac{e_\alpha n_\alpha}{E_{0r}} \left(A_1^\alpha + \frac{3}{2} A_2^\alpha \right) \\ = \sum_\alpha \frac{e_\alpha^2 n_\alpha}{T_\alpha} = \frac{1}{4\pi} \sum_\alpha \frac{1}{\lambda_{\mathrm{D}\alpha}^2}. \tag{3.117}$$

For the term involving G_m, we keep the first correction in I^{11},

$$\frac{\mathrm{i}k_\parallel^2}{\omega_E E_{0r}} G_m \approx \frac{k_\parallel^2}{\omega_E E_{0r}} \sum_\alpha \frac{e_\alpha n_\alpha v_{T\alpha}^2 \varrho_{\mathrm{L}\alpha}^2}{2\nu_\alpha} \frac{x_2}{x_1^2} \left(A_1^\alpha + \frac{5}{2} A_2^\alpha + \mathrm{i} \sqrt{\frac{\pi}{2}} \frac{x_2}{|x_1|} (A_1^\alpha + 2A_2^\alpha) \right) \\ = \frac{1}{2} H - \mathrm{i} \sqrt{\frac{\pi}{2}} \frac{ck_\perp}{B_0 |k_\parallel|} \sum_\alpha \frac{e_\alpha n_\alpha \varrho_{\mathrm{L}\alpha}^2}{2v_{T\alpha}} (A_1^\alpha + 2A_2^\alpha) \\ = \frac{1}{2} H - \frac{\mathrm{i}}{8\pi} \sqrt{\frac{\pi}{2}} \frac{k_\perp}{|k_\parallel|} \sum_\alpha \frac{\varrho_{\mathrm{L}\alpha}^3}{\lambda_{\mathrm{D}\alpha}^2} (A_1^\alpha + 2A_2^\alpha). \tag{3.118}$$

Since $H \sim \varrho_{\mathrm{L}i}^2 / \lambda_{\mathrm{D}i}^2$, the second term is a correction of the order $\varrho_{\mathrm{L}i}/L_\mathrm{p}$ where L_p is a typical gradient length of plasma parameters. Keeping this correction only for the terms with Φ_m

where a cancellation occurs, the perturbed charge density is

$$4\pi\varrho_{\boldsymbol{m}} \approx -\sum_{\alpha}\frac{1}{\lambda_{\mathrm{D}\alpha}^2}\left(\Phi_{\boldsymbol{m}}+\frac{\mathrm{i}E_{0r}B_{\boldsymbol{m}}^r}{k_\parallel B_0}\right)-\sum_{\alpha}\frac{\varrho_{\mathrm{L}\alpha}^2 V_{\alpha\perp}}{\lambda_{\mathrm{D}\alpha}^2 v_E}\frac{\partial^2}{\partial r^2}\frac{\mathrm{i}E_{0r}B_{\boldsymbol{m}}^r}{k_\parallel B_0}+ \\ +\mathrm{i}\sqrt{\frac{\pi}{8}}\frac{k_\perp}{|k_\parallel|}\sum_{\alpha}\frac{\varrho_{\mathrm{L}\alpha}^3}{\lambda_{\mathrm{D}\alpha}^2}(A_1^\alpha+2A_2^\alpha)\frac{\partial^2}{\partial r^2}\Phi_{\boldsymbol{m}}, \tag{3.119}$$

where we ignored derivatives of the equilibrium field and of $k_\parallel$. We see that the last term may exceed the Laplacian term in the Poisson equation, but it cannot produce a running wave because it is purely imaginary. Then, radial derivatives of the potential perturbation can be estimated as $1/L_\mathrm{p}$, and this term is a correction of the order $\varrho_{\mathrm{L}i}^3/L_\mathrm{p}^3 \ll 1$. Similarly, we get that terms with magnetic field derivatives estimated in the same manner produce a correction of the order of $\varrho_{\mathrm{L}i}^2/L_\mathrm{p}^2 \ll 1$. Thus, the Poisson equation in the ideal region still reduces to the charge neutrality condition which aligns the potential with perturbed flux surfaces.

3.3.2 Extension to Toroidal Geometry

In order to accomodate toroidal geometry, we include FLR effects in the extended formula (3.63) for the parallel current density which was obtained via the cylindrical expression (3.56). Using now formula (3.115), which includes the FLR effects, we approximately get

$$\left(\frac{J_{1\parallel}}{B_0}\right)_{\boldsymbol{m}} = -\frac{F_{\boldsymbol{m}}}{B_{0\varphi}}\left(\left(\frac{B_1^r}{B_0^\varphi}\right)_{\boldsymbol{m}}-\mathrm{i}\frac{m+nq}{qE_{0r}}\Phi_{\boldsymbol{m}}\right)- \\ -\frac{\partial^2}{\partial r^2}\left\langle R^2|\nabla r|^2\right\rangle_\theta\frac{G_{\boldsymbol{m}}^{\mathrm{tor}}}{B_{0\varphi}}\left(\left(\frac{B_1^r}{B_0^\varphi}\right)_{\boldsymbol{m}}-\mathrm{i}\frac{m+nq}{qE_{0r}}\Phi_{\boldsymbol{m}}\right)- \\ -\left\langle R^2|\nabla r|^2\right\rangle_\theta\frac{G_{\boldsymbol{m}}^{\mathrm{tor}}}{B_{0\varphi}}\left(\frac{\partial^2}{\partial r^2}\left(\frac{B_1^r}{B_0^\varphi}\right)_{\boldsymbol{m}}-\mathrm{i}\frac{m+nq}{qE_{0r}}\frac{\partial^2}{\partial r^2}\Phi_{\boldsymbol{m}}\right). \tag{3.120}$$

Here, we extended the definition of $G_{\boldsymbol{m}}$ to $G_{\boldsymbol{m}}^{\mathrm{tor}}$,

$$G_{\boldsymbol{m}}^{\mathrm{tor}} = \frac{B_0^2}{B_{0\varphi}^2}G_{\boldsymbol{m}} = \sum_{\alpha}\frac{e_\alpha n_\alpha v_{T\alpha}^2\varrho_{\mathrm{L}\alpha}^2 B_0^2}{2\nu_\alpha B_{0\varphi}^2}\left((A_1^\alpha+2A_2^\alpha)I^{11}+\frac{1}{2}A_2^\alpha I^{13}\right), \tag{3.121}$$

so that the common factor here is flux a function, as $\varrho_{\mathrm{L}\alpha}B_0$ does not depend on angles. Next, we extend the definition of charge density (3.114), as we did from (3.52) to (3.73),

$$\frac{B_{0\varphi}}{B_0^\varphi}\varrho_{\boldsymbol{m}} = \frac{m+nq}{q\omega_E}F_{\boldsymbol{m}}\left(\left(\frac{B_1^r}{B_0^\varphi}\right)_{\boldsymbol{m}}-\mathrm{i}\frac{m+nq}{qE_{0r}}\Phi_{\boldsymbol{m}}\right)+ \\ +\left\langle R^2|\nabla r|^2\right\rangle_\theta\frac{\partial^2}{\partial r^2}\frac{m+nq}{q\omega_E}G_{\boldsymbol{m}}^{\mathrm{tor}}\left(\left(\frac{B_1^r}{B_0^\varphi}\right)_{\boldsymbol{m}}-\mathrm{i}\frac{m+nq}{qE_{0r}}\Phi_{\boldsymbol{m}}\right)+$$

$$+\left\langle R^2|\nabla r|^2\right\rangle_\theta \frac{m+nq}{q\omega_E} G_m^{\mathrm{tor}} \left(\frac{\partial^2}{\partial r^2} \left(\frac{B_1^r}{B_0^\varphi} \right)_m - \mathrm{i} \frac{m+nq}{qE_{0r}} \frac{\partial^2}{\partial r^2} \Phi_m \right) +$$
$$+\left\langle R^2|\nabla r|^2\right\rangle_\theta \left(\frac{\partial^2}{\partial r^2} H^{\mathrm{tor}} \Phi_m + H^{\mathrm{tor}} \frac{\partial^2}{\partial r^2} \Phi_m \right). \tag{3.122}$$

In order to make it a flux function, we extended the definition (3.113) as follows:

$$H^{\mathrm{tor}} = \frac{B_0^2 R_0^2}{B_{0\varphi}^2} H = -\sum_\alpha \frac{e_\alpha n_\alpha \varrho_{\mathrm{L}\alpha}^2 B_0^2 R_0^2}{2E_{0r} B_{0\varphi}^2} \left(A_1^\alpha + \frac{5}{2} A_2^\alpha \right). \tag{3.123}$$

This definition is consistent with the postulation (3.67) for x_1 in the sense that cancellation of the leading order term in the factor of the derivative of Φ_m still occurs in the ideal region. Finally, the Poisson equation (3.73) is extended to

$$\begin{aligned}
\frac{\partial^2}{\partial r^2}\Phi_m = &-\frac{4\pi(m+nq)}{q\omega_E \left\langle R^2|\nabla r|^2\right\rangle_\theta} F_m \left(\left(\frac{B_1^r}{B_0^\varphi} \right)_m - \mathrm{i} \frac{m+nq}{qE_{0r}} \Phi_m \right) - \\
&-\frac{\partial^2}{\partial r^2} \frac{4\pi(m+nq)}{q\omega_E} G_m^{\mathrm{tor}} \left(\left(\frac{B_1^r}{B_0^\varphi} \right)_m - \mathrm{i} \frac{m+nq}{qE_{0r}} \Phi_m \right) - \\
&-\frac{4\pi(m+nq)}{q\omega_E} G_m^{\mathrm{tor}} \left(\frac{\partial^2}{\partial r^2} \left(\frac{B_1^r}{B_0^\varphi} \right)_m - \mathrm{i} \frac{m+nq}{qE_{0r}} \frac{\partial^2}{\partial r^2} \Phi_m \right) - \\
&-4\pi \left(\frac{\partial^2}{\partial r^2} H^{\mathrm{tor}} \Phi_m + H^{\mathrm{tor}} \frac{\partial^2}{\partial r^2} \Phi_m \right).
\end{aligned} \tag{3.124}$$

The straight-cylinder limit is recovered from (3.120) and (3.124) by choosing r to be the minor radius and setting $\langle R^2|\nabla r|^2\rangle_\theta = R_0^2$, $B_0^\varphi = B_0/R_0$, and $B_{0\varphi} = B_0 R_0$.

3.3.3 Representation for the Finite Difference Method

To solve the Poisson equation (3.124) using a lowest-order finite difference representation, it is convenient to re-notate it as

$$a_2^{\mathrm{out}} \frac{\partial^2}{\partial r^2}\Phi_m + \frac{\partial^2}{\partial r^2} a_2^{\mathrm{in}} \Phi_m + a_0 \Phi_m = b_2^{\mathrm{out}} \frac{\partial^2}{\partial r^2} \left(\frac{B_1^r}{B_0^\varphi} \right)_m + \frac{\partial^2}{\partial r^2} b_2^{\mathrm{in}} \left(\frac{B_1^r}{B_0^\varphi} \right)_m + b_0 \left(\frac{B_1^r}{B_0^\varphi} \right)_m \tag{3.125}$$

where

$$a_2^{\mathrm{in}} = -\frac{4\pi\mathrm{i}(m+nq)^2 G_m^{\mathrm{tor}}}{q^2\omega_E E_{0r}} + 4\pi H^{\mathrm{tor}}, \quad a_2^{\mathrm{out}} = 1 + a_2^{\mathrm{in}}, \quad a_0 = -\frac{4\pi\mathrm{i}(m+nq)^2 F_m}{q^2\omega_E E_{0r} \left\langle R^2|\nabla r|^2\right\rangle_\theta}, \tag{3.126}$$

$$b_2^{\mathrm{in}} = -\frac{4\pi(m+nq)G_m^{\mathrm{tor}}}{q\omega_E}, \qquad b_2^{\mathrm{out}} = b_2^{\mathrm{in}}, \qquad b_0 = -\frac{4\pi(m+nq)F_m}{q\omega_E \left\langle R^2|\nabla r|^2\right\rangle_\theta}. \tag{3.127}$$

The expression for the current density (3.120) is compacted similarly to

$$\left(\frac{J_{1\parallel}}{B_0}\right)_{\boldsymbol{m}} = c_2^{\text{out}}\frac{\partial^2}{\partial r^2}\Phi_{\boldsymbol{m}} + \frac{\partial^2}{\partial r^2}c_2^{\text{in}}\Phi_{\boldsymbol{m}} + c_0\Phi_{\boldsymbol{m}} + \\ + d_2^{\text{out}}\frac{\partial^2}{\partial r^2}\left(\frac{B_1^r}{B_0^\varphi}\right)_{\boldsymbol{m}} + \frac{\partial^2}{\partial r^2}d_2^{\text{in}}\left(\frac{B_1^r}{B_0^\varphi}\right)_{\boldsymbol{m}} + d_0\left(\frac{B_1^r}{B_0^\varphi}\right)_{\boldsymbol{m}} \tag{3.128}$$

where

$$c_2^{\text{in}} = \frac{\mathrm{i}(m+nq)G_{\boldsymbol{m}}^{\text{tor}}\left\langle R^2|\nabla r|^2\right\rangle_\theta}{qE_{0r}B_{0\varphi}}, \qquad c_2^{\text{out}} = c_2^{\text{in}}, \qquad c_0 = \frac{\mathrm{i}(m+nq)F_{\boldsymbol{m}}}{qE_{0r}B_{0\varphi}}, \tag{3.129}$$

$$d_2^{\text{in}} = -\frac{G_{\boldsymbol{m}}^{\text{tor}}\left\langle R^2|\nabla r|^2\right\rangle_\theta}{B_{0\varphi}}, \qquad d_2^{\text{out}} = d_2^{\text{in}}, \qquad d_0 = -\frac{F_{\boldsymbol{m}}}{B_{0\varphi}}. \tag{3.130}$$

For an efficient implementation, the following relations are useful:

$$a_0 = \mathrm{i}\frac{m+nq}{qE_{0r}}b_0, \qquad a_2^{\text{in}} = \mathrm{i}\frac{m+nq}{qE_{0r}}b_2^{\text{in}} + 4\pi H^{\text{tor}}, \tag{3.131}$$

$$c_0 = -\mathrm{i}\frac{m+nq}{qE_{0r}}d_0, \qquad c_2^{\text{in}} = -\mathrm{i}\frac{m+nq}{qE_{0r}}d_2^{\text{in}}. \tag{3.132}$$

Chapter 4

Numerical Treatment

On the highest level, the simulation underlying MEPHIT proceeds via the follow steps.

1. Field-line integration of the equilibrium magnetic field $\boldsymbol{B}_0$ yields (R, Z) coordinates of points of constant ψ with high resolution, i.e., flux surface cross-sections. This procedure, as well as the retrieval of various other equilibrium quantities is described in section 4.1.
2. From these, a coarser, but still field-aligned grid, i.e., a structured mesh, is constructed according to section 4.4. This triangulation serves as a basis for the finite elements described in section 4.3.
3. The vacuum perturbation field $\delta\boldsymbol{B}_\mathrm{v}$ is calculated from the external coil currents by the Biot–Savart law as described in section 4.2. For the selected toroidal mode number n, $\boldsymbol{B}_n$ is then projected onto the finite element basis.
4. The iterations steps are performed according to chapter 2, with implementation details given in sections 4.5 and 4.6.
5. The results are post-processed and possibly converted as discussed in section 4.7.

The results of this procedure are shown in section 5.2.

4.1 Equilibrium Quantities

The equilibrium quantities are assumed to be available in GEQDSK format, shortly summarized by Lao [15] and commonly created with codes like EFIT and CLISTE. It consists of

- ψ data points given on a rectangular (R, Z) grid, which we interpolate with quintic splines in R and Z,
- *profiles*, i.e., flux surface quantities $F(\psi)$, $p_0(\psi)$, $FF'(\psi)$, $p_0'(\psi)$, $q(\psi)$ given for equidistant values of ψ, which we interpolate with Lagrange polynomials of fourth order,
- geometric data: the position $(R_\mathrm{O}, Z_\mathrm{O})$ of the magnetic axis, points on the separatrix, a polygon approximating the vacuum vessel, all of which are displayed in figure 1.1,
- the toroidal current, and the magnetic field at the center, which are relevant for the sign conventions covered in section 4.7.

Note that the code to handle these equilibrium quantities is shared with Gorilla [16], but the latter assumes $F = B_{0\varphi}$ to be constant. Furthermore, alternative values for p_0 may be supplied, and q computed from the field-line integration described further below is usually more reliable than the values supplied by the GEQDSK file. The toroidal equilibrium current density J_0^{tor} may be computed by Ampère's law,

$$J_0^{\text{tor}} = \frac{c}{4\pi}\left(\frac{\partial B_0^R}{\partial Z} - \frac{\partial B_0^Z}{\partial R}\right). \tag{4.1}$$

This reduces to the second derivative of a spline in ψ, which may result in unacceptable amplification of any noise present in the input data or introduced by spline interpolation. One solution to this problem is to smooth out input data by averaging over a given number of neighbouring data points. Alternatively, the toroidal equilibrium current may be recovered from the solution of the Grad–Shafranov equation, the necessary data being contained in the GEQDSK file, as discussed near equation (1.1). Lao [15] includes the corresponding formula, but note that a factor of μ_0 is missing in the denominator of the second term on the right-hand side. The relation in Gaussian units is given by

$$J_0^{\text{tor}} = cRp_0'(\psi) + \frac{c}{4\pi R}FF'(\psi). \tag{4.2}$$

With the equilibrium magnetic field available via spline evaluation, we can perform field-line integration. Using the relation between coordinates and magnetic field components from D'haeseleer et al. [5], we can write the equations for a magnetic field line as

$$\frac{\mathrm{d}R}{\mathrm{d}\varphi} = \frac{B_0^R}{B_0^\varphi} = \frac{\hat{B}_{0R}}{\hat{B}_{0\varphi}}R, \qquad \frac{\mathrm{d}Z}{\mathrm{d}\varphi} = \frac{B_0^Z}{B_0^\varphi} = \frac{\hat{B}_{0Z}}{\hat{B}_{0\varphi}}R. \tag{4.3}$$

These $y_1'(\varphi), y_2'(\varphi)$ can be integrated along the curve parameter φ with standard Runge–Kutta methods, yielding the poloidal position $(y_1, y_2) = (R, Z)$, which in turn is used in spline evaluation of the magnetic field. Projected onto the poloidal cross-section, this position will move along the contours depicted in figure 1.1, and $|q|$ toroidal turns are necessary to complete one poloidal turn. By adding further y_k', we can determine the position of the magnetic axis and the X point, as well as various flux functions and the symmetry flux coordinates. To find the magnetic axis, we use

$$y_3' = R, \qquad y_3 = \langle R\rangle\,\Delta\varphi, \tag{4.4}$$

$$y_4' = Z, \qquad y_4 = \langle Z\rangle\,\Delta\varphi, \tag{4.5}$$

where $\Delta\varphi$ is the integration interval, here some multiple of 2π, and $\langle\cdot\rangle$ denotes the flux surface average. For nested elliptical cross-sections without Shafranov shift, $\langle R\rangle$ and $\langle Z\rangle$ would already correspond to the position of the magnetic axis, but even in the general case they lie on a flux surface inside the one we averaged over. Using $\langle R\rangle$ and $\langle Z\rangle$ as new initial values for

y_1' and y_2', and repeating the process draws ever smaller contours, approaching the magnetic axis at $(R_\mathrm{O}, Z_\mathrm{O})$ arbitrarily close.

To find the separatrix, we start the field-line integration at $(R_\mathrm{O} + \Delta R, Z_\mathrm{O})$ with ΔR gradually increasing, i.e., we move in outboard direction. For each ΔR, we repeatedly take small steps in $\Delta\varphi$ in order to take note of the sign of $Z - Z_\mathrm{O}$. After the sign changes a second time, one poloidal turn is completed. If at any intermediate step the resulting (R, Z) is located outside the rectangular grid, we followed a non-closed flux surface and thus bracketed the separatrix; otherweise we proceed with larger ΔR until this is the case.

One step further inside lies the last closed flux surface for the chosen resolution. Starting again at $(R_\mathrm{O} + \Delta R, Z_\mathrm{O})$, we save the current and previous (R, Z) position of each step in order to determine the distance in the poloidal plane covered by the current integration step. Close to the X point, a poloidal null, this distance will be lowest, thus we save the associated position (R_X, Z_X) as the approximate X point. Again, by tracking the sign of $Z - Z_\mathrm{O}$, we ensure that we stop after one poloidal turn.

To calculate the flux functions, we need to determine the $\Delta\varphi$ for which exactly one poloidal turn is completed. We start at the $\theta = 0$ line, which lies at an angle θ_0 relative to the horizontal line extending from the magnetic axis in outboard direction, i.e., the initial position is now $(R_0 + \Delta R\, \cos\theta_0, Z_0 + \Delta R\, \sin\theta_0)$. The method used already twice above stops after surpassing the starting position (now at θ_0), but it depends on the chosen step size by how much. To improve upon this estimate, we use Newton's method as follows. Consider the vector from the magnetic axis to the current poloidal position, and the tangent vector of the magnetic field line in the poloidal plane, i.e.,

$$\boldsymbol{r} = (R - R_0)\hat{\boldsymbol{e}}_R + (Z - Z_0)\hat{\boldsymbol{e}}_Z = (y_1 - R_0)\hat{\boldsymbol{e}}_R + (y_2 - Z_0)\hat{\boldsymbol{e}}_Z, \tag{4.6}$$

$$\boldsymbol{s} = \frac{\mathrm{d}R}{\mathrm{d}\varphi}\hat{\boldsymbol{e}}_R + \frac{\mathrm{d}Z}{\mathrm{d}\varphi}\hat{\boldsymbol{e}}_Z = y_1'\hat{\boldsymbol{e}}_R + y_2'\hat{\boldsymbol{e}}_Z, \tag{4.7}$$

as well as the angles between them and the $\theta = 0$ line,

$$\theta_{\boldsymbol{r}} = \arctan\frac{Z - Z_\mathrm{O}}{R - R_0} - \theta_0 = \arctan\frac{y_2 - Z_\mathrm{O}}{y_1 - R_0} - \theta_0, \tag{4.8}$$

$$\theta_{\boldsymbol{s}} = \arctan\frac{\frac{\mathrm{d}Z}{\mathrm{d}\varphi}}{\frac{\mathrm{d}R}{\mathrm{d}\varphi}} - \theta_0 = \arctan\frac{y_2'}{y_1'} - \theta_0. \tag{4.9}$$

We project both vectors onto the tangential direction at θ_0, i.e., $\hat{\boldsymbol{e}}_\theta$. This is the distance $|\boldsymbol{r}|\sin\theta_{\boldsymbol{r}}$ of which we want to find the zero position, and its derivative is $|\boldsymbol{s}|\sin\theta_{\boldsymbol{s}}$. Now we only need to take care of the sign of $\theta'(\varphi)$, which is just the sign of the safety factor q. This is easily determined by evaluating $\sigma_q = \operatorname{sgn}\hat{B}_{0Z}\hat{B}_{0\varphi}$ at $(R_\mathrm{O} + \Delta R, Z_\mathrm{O})$. Putting everything together,

we update the integration interval as follows:

$$\Delta\varphi \to \Delta\varphi - \frac{|\boldsymbol{r}| \sin\theta_{\boldsymbol{r}}}{|\boldsymbol{s}| \sin\theta_{\boldsymbol{s}}}\sigma_q. \tag{4.10}$$

With $\Delta\varphi$ thus determined, we can immediately compute the safety factor on this flux surface in analogy to (1.6) as

$$q = \frac{2\pi}{\Delta\varphi}\sigma_q. \tag{4.11}$$

Spline evaluation at (R, Z) yields the poloidal flux, while the flux surface area A and the circumference C are obtained from field line integration:

$$y_5' = R\frac{\mathrm{d}Z}{\mathrm{d}\varphi}, \qquad y_5 = A, \tag{4.12}$$

$$y_6' = \sqrt{\left(\frac{\mathrm{d}R}{\mathrm{d}\varphi}\right)^2 + \left(\frac{\mathrm{d}Z}{\mathrm{d}\varphi}\right)^2}, \qquad y_6 = C. \tag{4.13}$$

Finally, with q known, we can take integration steps at $\Delta\vartheta = q\,\Delta\varphi$. We save the corresponding values of $R(\psi, \vartheta)$ and $Z(\psi, \vartheta)$ and interpolate them with splines, which allows us to transform symmetry flux coordinates to cylindrical coordinates. Evaluating (1.7) yields the associated metric determinant, and y_6 from (4.13) contains the equal-arclength poloidal angle.

Some of the above quantities and partial derivatives are also cached at certain evaluation points, e.g., in regards to the flux surface cross-sections described in further detail in section 4.4. For the profiles, there is one value *on* each flux surface, referred to as *full-grid* value, and one value *between* flux surfaces, referred to as *half-grid* value. The poloidal Fourier series expansion serves as an example. As discussed in section 4.3, the pressure perturbation is represented by values on the flux surface, so the associated poloidal Fourier amplitudes are full-grid values. On the other hand, the reperesentation of the magnetic field and current density perturbations is discontinuous along triangle edges, so interpolation is performed between flux surfaces, resulting in half-grid values for the associated poloidal Fourier amplitudes.

4.2 Magnetic Field Perturbation in Vacuum

Assuming coils of infinitesimal width, the vacuum perturbation field $\delta\boldsymbol{B}_{\mathrm{v}}$ of chapter 2, which we simplify to $\delta\boldsymbol{B}$ for the remainder of this section, is computed from the current I_k flowing in the closed contour C_k of the coil k via the Biot-Savart law evaluated at position $\boldsymbol{x}$,

$$\delta\boldsymbol{B}(\boldsymbol{x}) = c_0 \sum_k I_k \int_{C_k} \mathrm{d}\boldsymbol{l}_k \times \frac{\boldsymbol{x} - \boldsymbol{l}_k}{|\boldsymbol{x} - \boldsymbol{l}_k|^3} =: \frac{c_0}{I_0} \sum_k I_k\, \delta\boldsymbol{B}_k(\boldsymbol{x}). \tag{4.14}$$

As the last step already suggests, we compute the magnetic field $\delta \boldsymbol{B}_k$ of each coil k separately for unit current I_0, and only take the sum over the coils and their currents at the very end, which is allowed because the summation and integration are linear and exchangeable. This way, the computationally expensive Biot-Savart integral, which only depends on the coil geometry and not on the changing coil currents, needs only be evaluated once per *device* instead of once per *shot* or even time slice.

Furthermore, we are interested in the toroidal Fourier modes $\boldsymbol{B}_n$ of $\delta \boldsymbol{B}$. The discrete Fourier transform of the three-dimensional field is also a linear operation, so we can compute $\boldsymbol{B}_{n,k}$ from $\delta \boldsymbol{B}_k$ and save the former for later retrieval, i.e., for the linear combination with I_k for the specific shot or time slice. Since the actual evaluation points depend on the mesh and thus on the specific equilibrium and configuration values, and the discrete Fourier transform is computed numerically instead of analytically, interpolation is necessary. Thus we use the same bivariate fifth-order splines as in section 4.1, albeit for the vector potential $\boldsymbol{A}_n$ to ensure zero divergence for interpolated $\boldsymbol{B}_n$. For toroidal mode numbers $n \neq 0$, the magnetic vector potential can be gauged such that $\hat{A}_{n\varphi} = 0$, as discussed in section 2.1. Note that the contribution from $n = 0$ is assumed to be contained in the equilibriu $\boldsymbol{B}_0$ already and does not need to be considered here. This results in the following expressions for the magnetic field in cylindrical coordinates:

$$\hat{B}_{nR} = \frac{\mathrm{i}n}{R}\hat{A}_{nZ}, \qquad \hat{B}_{n\varphi} = \frac{\partial}{\partial Z}\hat{A}_{nR} - \frac{\partial}{\partial R}\hat{A}_{nZ}, \qquad \hat{B}_{nZ} = -\frac{\mathrm{i}n}{R}\hat{A}_{nR}. \tag{4.15}$$

With this gauge, only a simple algebraic transformation is needed to obtain $\boldsymbol{A}_n$ from $\boldsymbol{B}_n$. Note that $\hat{B}_{n\varphi}$ is not used in construction of the splines even though it is easily available from the Biot-Savart law.

This ansatz has one disadvantage: the magnetic field diverges towards the coils, which are generally located inside the rectangular computational domain, and trying to resolve such a field results in spline oscillation. The current approach to alleviate this is by "contracting" the coordinates: any evaluation point outside a defined convex polygon modelled on the vacuum vessel cross-section is smoothly mapped to a point closer to the convex polygon, thus avoiding the singularity near the coils. This requires manual definition of the convex polygon fitting the device for which simulations are performed. Another approach under investigation is to avoid the singularity during the evaluation of the Biot-Savart integral, which is discussed in further detail below.

Coil geometries are commonly given as filamentary segments, i.e., a list of points on each coil which are connected by straight lines. Hanson and Hirshman [17] derive a closed-form expression of the Biot-Savart integral over such a line segment and discuss how to handle the singularity, and application of the resulting formula for $\delta \boldsymbol{B}$ is straightforward. Seeing how we ignore the toroidal component near (4.15), we consider computing the gauged vector potential directly, which does not ignore part of the computation and turns out to improve the spline behaviour somewhat. The simplest representation of the gauge potential for (4.15)

is in Fourier space,

$$\chi_n = \frac{\mathrm{i}R}{n}\hat{A}_{n\varphi}, \tag{4.16}$$

so the calculation steps are:

1. from the Biot-Savart law, calculate the Cartesian components of $\boldsymbol{A}, \nabla\hat{A}_X, \nabla\hat{A}_Y$,
2. by coordinate transform, calculate the cylindrical components of $\boldsymbol{A}, \partial_R\hat{A}_\varphi, \partial_Z\hat{A}_\varphi$,
3. by discrete Fourier transform, calculate the Fourier amplitudes of $\boldsymbol{A}_n, \partial_R\hat{A}_{n\varphi}, \partial_Z\hat{A}_{n\varphi}$,
4. calculate bivariate splines of the gauged components $\hat{A}_{nR} + \partial_R\chi_n$ and $\hat{A}_{nZ} + \partial_Z\chi_n$.

For a current I along a line segment beginning at $\boldsymbol{x}_\mathrm{i}$ and ending at $\boldsymbol{x}_\mathrm{f}$, Hanson and Hirshman [17] give the following expression for the magnetic vector potential at evaluation point $\boldsymbol{x}$, transformed to Gaussian units,

$$\boldsymbol{A}(\boldsymbol{x}) = \frac{I}{c}\frac{\boldsymbol{L}}{L}\ln\frac{R_\mathrm{i} + R_\mathrm{f} + L}{R_\mathrm{i} + R_\mathrm{f} - L}, \tag{4.17}$$

where $\boldsymbol{L} = \boldsymbol{x}_\mathrm{f} - \boldsymbol{x}_\mathrm{i}$, $\boldsymbol{R}_\mathrm{i} = \boldsymbol{x} - \boldsymbol{x}_\mathrm{i}$, $\boldsymbol{R}_\mathrm{f} = \boldsymbol{x} - \boldsymbol{x}_\mathrm{f}$. They further introduce a parameter

$$\varepsilon = \frac{L}{R_\mathrm{i} + R_\mathrm{f}}, \tag{4.18}$$

whose geometric interpretation is the eccentrity of an ellipse with focal points $\boldsymbol{x}_\mathrm{i}$ and $\boldsymbol{x}_\mathrm{f}$ passing through $\boldsymbol{x}$. This is useful when introducing a cutoff to avoid the singularity at the infinitesimally thin wire as $\varepsilon \to 1$, which can be seen from the expression

$$\ln\frac{R_\mathrm{i} + R_\mathrm{f} + L}{R_\mathrm{i} + R_\mathrm{f} - L} = \ln\frac{1+\varepsilon}{1-\varepsilon} =: f(\varepsilon). \tag{4.19}$$

As an option to avoid the singularity, we implement a maximum value for ε and a minimum value for R_i and R_f. Setting the former to 1 and the latter to 0 effectively applies no cutoff. Next, to calculate the gradient of the Cartesian components, we only need to consider the gradient of this function,

$$\begin{aligned}\nabla f(\varepsilon) = f'(\varepsilon)\nabla\varepsilon = \frac{2}{1-\varepsilon^2}\nabla\frac{L}{R_\mathrm{i}+R_\mathrm{f}} = \frac{2(R_\mathrm{i}+R_\mathrm{f})^2}{(R_\mathrm{i}+R_\mathrm{f})^2 - L^2}\frac{-L}{(R_\mathrm{i}+R_\mathrm{f})^2}(\nabla R_\mathrm{i} + \nabla R_\mathrm{f}) = \\ = \frac{2L}{L^2 - (R_\mathrm{i}+R_\mathrm{f})^2}\left(\frac{\boldsymbol{R}_\mathrm{i}}{R_\mathrm{i}} + \frac{\boldsymbol{R}_\mathrm{f}}{R_\mathrm{f}}\right) = -\frac{L}{R_\mathrm{i}R_\mathrm{f} + \boldsymbol{R}_\mathrm{i}\cdot\boldsymbol{R}_\mathrm{f}}\left(\frac{\boldsymbol{R}_\mathrm{i}}{R_\mathrm{i}} + \frac{\boldsymbol{R}_\mathrm{f}}{R_\mathrm{f}}\right),\end{aligned} \tag{4.20}$$

where in the last step, we used $\boldsymbol{L} = \boldsymbol{R}_\mathrm{f} - \boldsymbol{R}_\mathrm{i}$. The Cartesian components and their gradients then are

$$\hat{A}_k = \frac{I}{c}\frac{\hat{L}_k}{L}\ln\frac{R_\mathrm{i} + R_\mathrm{f} + L}{R_\mathrm{i} + R_\mathrm{f} - L}, \qquad \nabla\hat{A}_k = -\frac{I}{c}\frac{\hat{L}_k}{R_\mathrm{i}R_\mathrm{f} + \boldsymbol{R}_\mathrm{i}\cdot\boldsymbol{R}_\mathrm{f}}\left(\frac{\boldsymbol{R}_\mathrm{i}}{R_\mathrm{i}} + \frac{\boldsymbol{R}_\mathrm{f}}{R_\mathrm{f}}\right). \tag{4.21}$$

The remaining cylindrical components and partial derivatives are

$$\hat{A}_R = \hat{A}_X \cos\varphi + \hat{A}_Y \sin\varphi = \frac{I}{c}\frac{\hat{L}_X \cos\varphi + \hat{L}_Y \sin\varphi}{L} \ln\frac{R_\mathrm{i} + R_\mathrm{f} + L}{R_\mathrm{i} + R_\mathrm{f} - L}, \tag{4.22}$$

$$\hat{A}_\varphi = \hat{A}_Y \cos\varphi - \hat{A}_X \sin\varphi = \frac{I}{c}\frac{\hat{L}_Y \cos\varphi - \hat{L}_X \sin\varphi}{L} \ln\frac{R_\mathrm{i} + R_\mathrm{f} + L}{R_\mathrm{i} + R_\mathrm{f} - L}, \tag{4.23}$$

$$\partial_Z \hat{A}_\varphi = \partial_Z \hat{A}_Y \cos\varphi - \partial_Z \hat{A}_X \sin\varphi = -\frac{I}{c}\frac{\hat{L}_Y \cos\varphi - \hat{L}_X \sin\varphi}{R_\mathrm{i} R_\mathrm{f} + \boldsymbol{R}_\mathrm{i} \cdot \boldsymbol{R}_\mathrm{f}} \left(\frac{\hat{R}_{\mathrm{i},Z}}{R_\mathrm{i}} + \frac{\hat{R}_{\mathrm{f},Z}}{R_\mathrm{f}} \right), \tag{4.24}$$

$$\begin{aligned} \partial_R \hat{A}_\varphi &= \partial_X \hat{A}_Y \cos^2\varphi + (\partial_Y \hat{A}_Y - \partial_X \hat{A}_X) \sin\varphi\cos\varphi - \partial_Y \hat{A}_X \sin^2\varphi = \\ &= -\frac{I}{c}\frac{\hat{L}_Y \cos\varphi - \hat{L}_X \sin\varphi}{R_\mathrm{i} R_\mathrm{f} + \boldsymbol{R}_\mathrm{i} \cdot \boldsymbol{R}_\mathrm{f}} \left(\frac{\hat{R}_{\mathrm{i},X} \cos\varphi + \hat{R}_{\mathrm{i},Y} \sin\varphi}{R_\mathrm{i}} + \frac{\hat{R}_{\mathrm{f},X} \cos\varphi + \hat{R}_{\mathrm{f},Y} \sin\varphi}{R_\mathrm{f}} \right). \end{aligned} \tag{4.25}$$

The Fourier amplitudes of these quantities are then used for the gauged magnetic vector potential,

$$\hat{A}_{nR} \to \hat{A}_{nR} + \frac{\mathrm{i}R}{n} \left(\partial_R \hat{A}_\varphi \right)_n + \frac{\mathrm{i}}{n} \hat{A}_{n\varphi}, \tag{4.26}$$

$$\hat{A}_{nZ} \to \hat{A}_{nZ} + \frac{\mathrm{i}R}{n} \left(\partial_Z \hat{A}_\varphi \right)_n. \tag{4.27}$$

4.3 Finite Elements

The finite element method described in section 2.1, specifically (2.93), yields the contravariant density components of $\boldsymbol{B}_n^\mathrm{pol}$ represented in a finite element basis of $H^{\mathrm{div}_\mathrm{t}}$, such as Raviart–Thomas elements on triangles. Due to an error in the derivation in [18], the original method impemented in MEPHIT was only applicable to lowest-order (i.e., linear) Raviart–Thomas elements. While higher-order elements show a lower approximation error (see section 5.1.1), a more generic re-implementation is not trivial at this point. Furthermore, MEPHIT is intended to interface with Gorilla [16], which uses linearised perturbation quantities to reduce sensitivity to statistical noise. However, a comprehensive comparison of the effects resulting from different orders of finite elements is reserved for future work, thus linear interpolation is used for perturbation quantities.

As mentioned in section 1.1, cylindrical coordinates (R, φ, Z) have no singularity at the magnetic axis and are more easily extended beyond the separatrix, which simplifies the imposition of boundary conditions. Computations are thus performed in the poloidal plane spanned by R and Z and with a density $\sqrt{g_\mathrm{cyl}} = R$. For any triangle Ω in the poloidal plane, evaluation of the lowest-order Raviart–Thomas element at a point $\boldsymbol{r} = R\hat{\boldsymbol{e}}_R + Z\hat{\boldsymbol{e}}_Z$ within the triangle yields the magnetic field perturbation as

$$R\boldsymbol{B}_n^\mathrm{pol} = \frac{1}{2A_\Omega} \sum_{k=1}^{3} (\boldsymbol{r} - \boldsymbol{r}_k)\, \Psi_k. \tag{4.28}$$

Here, A_Ω is the area of the triangle Ω, Ψ_k is the scalar complex-valued *degree of freedom* associated with edge Γ_k, and $\boldsymbol{r}_k = R_k\hat{\boldsymbol{e}}_R + Z_k\hat{\boldsymbol{e}}_Z$ is the coordinate vector of the triangle vertex opposite edge Γ_k, as illustrated in figure 4.1a. Inversely, the degree of freedom can be determined from a given magnetic field perturbation as the integral along the associated edge Γ_k, with $\boldsymbol{n}_k$ the normal vector pointing outwards of the triangle:

$$\Psi_k = \int_{\Gamma_k} R\boldsymbol{B}_n^{\mathrm{pol}} \cdot \hat{\boldsymbol{n}}_k \, \mathrm{d}\Gamma_k. \tag{4.29}$$

Note that Ψ_k has the physical dimension of a magnetic flux and the symbol is chosen to reflect that, but it does not have a simple, direct physical interpretation — it does not result from the area integral of a three-dimensional magnetic flux density after the Fourier transform. This is in contrast to the three-dimensional case without Fourier series expansion, i.e., Raviart–Thomas elements defined on tetrahedra, where the degree of freedom for the lowest order is indeed the magnetic flux through the associated face of the tetrahedron. Further note that, with regard to two adjacent elements (triangles/tetrahedra), interpolation via (4.28) is generally discontinuous *along* edges/faces, but the perpendicular component *across* edges/faces is continuous, as can be seen from (4.29) yielding the same result for both triangles sharing that particular edge.

Next, as another consequence of the Fourier transform, consider the divergence, which consists of a poloidal contribution from (4.28) that is constant on each triangle, and an independent toroidal contribution:

$$\partial_k\left(\sqrt{g}\delta B^k\right) \to \partial_R\left(RB_n^R\right) + \partial_Z\left(RB_n^Z\right) + \mathrm{i}nRB_n^\varphi = \frac{1}{A_\Omega}\sum_{k=1}^{3}\Psi_k + \mathrm{i}nB_n^{\mathrm{tor}}. \tag{4.30}$$

To impose zero divergence, B_n^{tor} must also be constant on each triangle, corresponding to lowest-order Lagrange elements, and for this case, the toroidal component is determined as

$$B_n^{\mathrm{tor}} = \frac{\mathrm{i}}{nA_\Omega}\sum_{k=1}^{3}\Psi_k. \tag{4.31}$$

Using (4.31) and (4.29) together has one caveat regarding numerical accuracy. When solving the integral along the edge in (4.29) with Gauss–Legendre quadrature, one evaluation point should be sufficient to exactly integrate a linear function. This reduces the integral to a single term, the evaluation of the integrand at the mid-point of the edge multiplied by the length of the edge. The "inverse" operation, in a sense, is to evaluate (4.28) at the edge mid-point and multiply by the edge normal vector. This even reproduces the associated degree of freedom exactly, which can be seen by inserting, e.g. $\boldsymbol{r} = \frac{1}{2}(\boldsymbol{r}_1 + \boldsymbol{r}_2)$ and multiplying with $\boldsymbol{n}_3 = (Z_2 - Z_1)\hat{\boldsymbol{e}}_R - (R_2 - R_1)\hat{\boldsymbol{e}}_Z$, which yields Ψ_3. So it seems justified, and it appears that FreeFem++ [19] employs this one-point quadrature. However, comparing the result of (4.31) with the exact values for typical $\boldsymbol{B}_{n\mathrm{v}}$ shows large deviations even across neighbouring

triangles. Using higher orders in the Gauss–Legendre quadrature reduces these deviations considerably, and in fact, two evaluation points are already sufficient and higher orders show no further improvement.

Alternatively, the divergence in (4.30) can be computed from the toroidal component, effectively shifting the numerical error from the latter to the former. To this end, B_n^{tor} has to be averaged over the area of the triangle. Cowper [20] lists quadrature schemes of various orders, approximating the integral of a function f over a triangle Ω as

$$\iint_\Omega f(R,Z)\ \mathrm{d}R\,\mathrm{d}Z \approx A_\Omega \sum_{i=1}^{N} w_i f(R_i,Z_i). \tag{4.32}$$

Since second-order quadrature appears to be sufficient for (4.29), we use a fourth-order scheme for the area integral, i.e., second-order in both R and Z. One such scheme with $N = 6$ evaluation points, tabulated in table 4.1, is given by two sets of weights and barycentric coordinates λ_i, the latter of which are permuted to form triplets of distinct points, as indicated in figure 4.1d.

Table 4.1: Weights and evaluation points for fourth-order area integral approximation by Cowper [20]. The barycentric coordinates λ_i are permuted to form triplets of distinct points, i.e., (R_i, Z_i) in (4.32).

w_i	λ_1	λ_2	λ_3
0.109 951 743 655 322	0.816 847 572 980 459	0.091 576 213 509 771	0.091 576 213 509 771
0.223 381 589 678 011	0.108 103 018 168 070	0.445 948 490 915 965	0.445 948 490 915 965

The L^2 norm of the finite element function over one triangle Ω is also an area integral. As such, it could be computed via (4.32), but an analytic solution is also possible and turns out to be faster[1]. It involves multiplication of a 1×3 matrix containing edge vectors $\boldsymbol{l}_k$ as indicated in figure 4.1c, two constant 3×3 centrosymmetric matrices, and two 3×1 matrices constructed from the degrees of freedom Ψ_k as shown in figure 4.1a. The square of the norm is then

$$\left\|R\boldsymbol{B}_n^{\mathrm{pol}}\right\|_2^2 = \iint_\Omega \left|R\boldsymbol{B}_n^{\mathrm{pol}}\right|^2 \mathrm{d}R\,\mathrm{d}Z = \frac{1}{24A_\Omega}\begin{bmatrix}\boldsymbol{l}_3\cdot\boldsymbol{l}_3 & \boldsymbol{l}_3\cdot\boldsymbol{l}_1 & \boldsymbol{l}_1\cdot\boldsymbol{l}_1\end{bmatrix} \left(\begin{bmatrix}3 & 1 & 1\\ 3 & -1 & 3\\ 1 & 1 & 3\end{bmatrix}\begin{bmatrix}\Psi_1^*\Psi_1\\ \Psi_2^*\Psi_2\\ \Psi_3^*\Psi_3\end{bmatrix} + \begin{bmatrix}1 & -1 & -1\\ 1 & -3 & 1\\ -1 & -1 & 1\end{bmatrix}\begin{bmatrix}\Psi_2^*\Psi_3+\Psi_2\Psi_3^*\\ \Psi_3^*\Psi_1+\Psi_3\Psi_1^*\\ \Psi_1^*\Psi_2+\Psi_1\Psi_2^*\end{bmatrix}\right). \tag{4.33}$$

For the scalar perturbation quantities, the situation is much simpler. Solving the MDE (2.113) as described in section 4.5 yields the value of the pressure perturbation p_n at certain points. On any triangle resulting from the triangulation of all these points in the poloidal plane, linear

[1]The approximate solution by quadrature is retained as a unit test for the analytical solution.

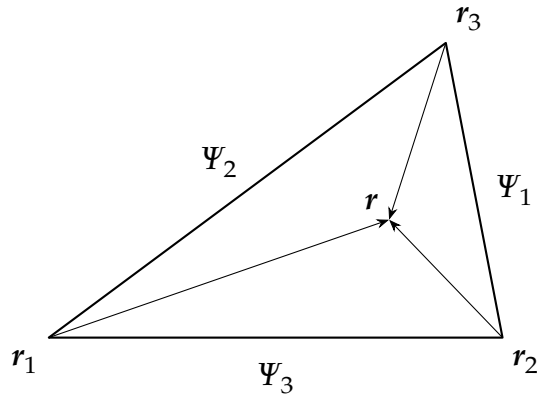

(a) Interpolation of linear Raviart–Thomas elements according to (4.28). The basis functions consist of vectors pointing from the triangle vertices $\boldsymbol{r}_k$ to the evaluation point $\boldsymbol{r}$. The degrees of freedom Ψ_k are associated with the edges opposite to the vertex $\boldsymbol{r}_k$.

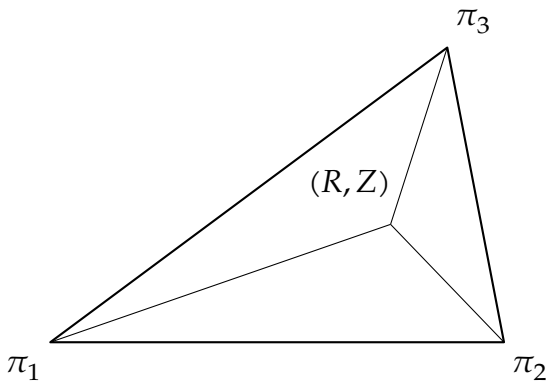

(b) Interpolation of linear Lagrange elements according to (4.34). The degrees of freedom π_k are associated with the triangle vertices $\boldsymbol{r}_k$. The basis functions are the barycentric coordinates corresponding to these vertices.

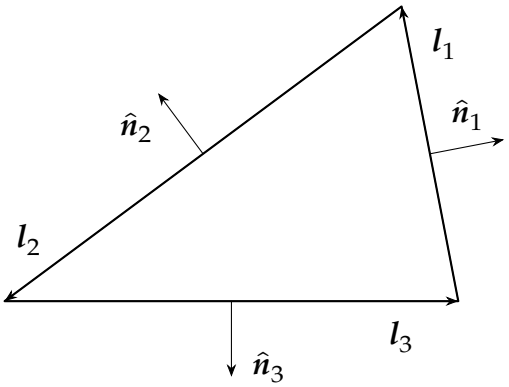

(c) Edge vectors $\boldsymbol{l}_k$ point in counter-clockwise direction in (4.33), and normal vectors $\boldsymbol{n}_k$ point outwards in (4.29).

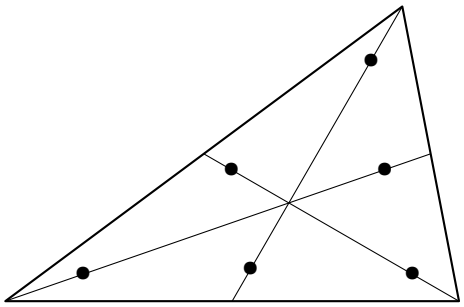

(d) Six evaluation points for the fourth-order area integral approximation given in table 4.1. The median lines are indicated for reference.

Figure 4.1: Example triangles illustrating the interpolation functions for $\boldsymbol{B}_n^{\mathrm{pol}}$ and p_n, as well as the definitions involved in the quadratures. The barycentric coordinate λ_k associated with one vertex $\boldsymbol{r}_k$ is the ratio between the area of the triangle spanned by the remaining two vertices and the evaluation point, and the total triangle area. In (4.1a) and (4.1b), the evaluation point (R, Z) has barycentric coordinates $(0.2 : 0.4 : 0.4)$.

interpolation corresponds to evaluation of Lagrange elements of second-lowest order:

$$p_n = \frac{1}{2A_\Omega} \sum_{i=1}^{3} \sum_{j=1}^{3} \sum_{k=1}^{3} \varepsilon_{ijk} (R - R_i)(Z - Z_j) \pi_k. \tag{4.34}$$

Here, the degrees of freedom π_k are simply the aforementioned values of p_n at triangle vertices. The interpolant within the triangle can also be interpreted as the sum of the degrees

of freedom weighted by the barycentric coordinates, as illustrated in figure 4.1b. Calculation of the gradient is straightforward, and similarly to the divergence of the Raviart–Thomas elements above, the value is constant on each triangle:

$$\frac{\partial p_n}{\partial R} = \frac{1}{2A_\Omega} \sum_{i=1}^{3} \sum_{j=1}^{3} \sum_{k=1}^{3} \varepsilon_{ijk} (Z - Z_j) \pi_k = \frac{1}{2A_\Omega} \sum_{i=1}^{3} \sum_{j=1}^{3} \sum_{k=1}^{3} \varepsilon_{ijk} Z_i \pi_k, \tag{4.35}$$

$$\frac{\partial p_n}{\partial Z} = \frac{1}{2A_\Omega} \sum_{i=1}^{3} \sum_{j=1}^{3} \sum_{k=1}^{3} \varepsilon_{ijk} (R - R_i) \pi_k = \frac{1}{2A_\Omega} \sum_{i=1}^{3} \sum_{j=1}^{3} \sum_{k=1}^{3} \varepsilon_{ijk} R_j \pi_k. \tag{4.36}$$

Finally, note that the approach laid out for $\boldsymbol{B}_n^{\mathrm{pol}}$ also applies to the current density perturbation $\boldsymbol{J}_n^{\mathrm{pol}}$ (or any quantity represented by contravariant density components), where the degrees of freedom I_k take the physical dimension of current, again without an underlying physical current. Likewise, $J_n^{\parallel} B_0^{-1}$ in the magnetic differential equation (2.122) is treated in the same manner as p_n.

4.4 Mesh Construction

Since the magnetic field perturbation $\delta\boldsymbol{B}$ is represented by an array containing the degrees of freedom for a finite element basis, it is necessary that these are interpreted in the same way in every iteration step, so that $\hat{K}$ in (2.15) stays the same, which is in turn required for the computation of $\hat{\Pi}$ in (2.16). As a consequence, the mesh cannot change between iteration steps. In particular, refinement of the mesh based on the result of iteration steps is not possible. It's only conceivable to use the converged result to construct a refined mesh and start iterations anew, but this is outside the scope of this thesis. Instead, we set out to construct a feasible mesh from the available information.

While not strictly necessary, for simplicity we use the same mesh for the different finite elements discussed in the previous section. Then the first restriction comes from the solution of the MDE as described in section 4.5: all mesh nodes need to be placed on nested flux surface cross-sections, resulting in a structured or *field-aligned mesh* where each triangle connects points on two adjacent cross-sections. Anticipating the behaviour of the perturbation, we need to place these cross-sections closer together near resonance positions, requiring *radial refinement*. Secondly, due to the approximation error incurred by a triangulation containing elongated triangles, we choose the number of points distributed over these cross-sections accordingly, a process we refer to as *poloidal refinement* by analogy. Finally, we construct a constrained Delaunay triangulation from this point set, along with the relevant data structures. Note that, as initially mentioned, different meshes could be used for the different finite elements, interpolating when necessary. This might yet be relevant when MEPHIT is applied to multiple toroidal modes n in parallel, such as for Fourier expansion of these modes in combination with Gorilla [16]. Both radial and poloidal refinement increase the size of the linear systems to be solved, so they should only be applied to the resonance positions of each specific n

separately. However, this is reserved for future work.

To determine the radial positions of the field-aligned mesh, we use the horizontal line extending from the magnetic axis outwards to the separatrix. In this context, r denotes the distance from the magnetic axis along this line[1], or rather its normalized variant $\hat{r}$, i.e., we search for a partition of the unit interval with some maximum subinterval length D. We also want to surround each known resonance position $\hat{r}_{\text{res}}$ symmetrically with subintervals of length d, such that the closest two points are centered around the resonance position and L points are added on each side. This results in the positions

$$\hat{r}_{\pm l} = \hat{r}_{\text{res}} \pm \left(l - \frac{1}{2} \right) d, \quad \forall l = 1, 2, \dots, L. \tag{4.37}$$

Between these finer regions, there should be a smooth transition to the coarser subintervals of maximum length D, in the sense that the ratio of adjacent subinterval lengths should not exceed some factor f. On the other hand, we want to minimize the number of points needed. Thus we extend the last subinterval of length d by subintervals of length fd, then by $f^2 d$, and so on, forming a geometric series in f, resulting in the positions

$$\hat{r}_{\pm(L+n)} = \hat{r}_{\text{res}} \pm \left(L - \frac{1}{2} + \frac{f^{n+1} - f^1}{f - 1} \right) d, \quad \forall n = 0, 1, \dots, N. \tag{4.38}$$

The resulting subinterval lengths must not exceed the given maximum D, and from that restriction, we can determine the maximum extent of the transitional region:

$$f^N d \leq D \quad \Rightarrow \quad N = \left\lfloor \frac{\ln D - \ln d}{\ln f} \right\rfloor. \tag{4.39}$$

In order to determine the points in the transitional regions, consider two adjacent resonance positions $\hat{r}_m$ and $\hat{r}_{m-1}$ and their associated additional points $\hat{r}_{-i,m}$ and $\hat{r}_{+j,m-1}$ determined by d_m, L_m, f_m and $d_{m-1}, L_{m-1}, f_{m-1}$, respectively. Starting from $i = L_m + N_m$ and $j = L_{m-1} + N_{m-1}$, we calculate the distance

$$\Delta(i, j) = \hat{r}_{-i,m} - \hat{r}_{+j,m-1}. \tag{4.40}$$

If Δ is negative, the adjacent fine regions overlap. Until Δ is positive, either i or j is reduced by one, down to a minimum of L_m and L_{m-1}, respectively. If neither can be further reduced, the algorithm fails and another set of parameters has to be chosen. If both can be reduced, the point further apart from the next point of its own set is chosen to be removed, i.e., if

$$d_m f_m^{i - L_m} \geq d_{m-1} f_m^{j - L_{m-1}}, \tag{4.41}$$

i is reduced, and otherwise j is reduced. To determine the number k of subintervals into which

[1] corresponding to ΔR in section 4.1

the resulting coarse region of length Δ is divided, we consider the maximum distance that fulfills the restrictions imposed by f_m and f_{m-1}, i.e.,

$$k(i,j) = \left\lceil \frac{\Delta(i,j)}{\min\left(D, d_m f_m^{i-L_m+1}, d_{m-1} f_m^{j-L_{m-1}+1}\right)} \right\rceil. \tag{4.42}$$

Then, until

$$\frac{\Delta(i,j)}{k(i,j)} \geq d_m f_m^{i-L_m} \quad \wedge \quad \frac{\Delta(i,j)}{k(i,j)} \geq d_{m-1} f_m^{j-L_{m-1}}, \tag{4.43}$$

the reduction scheme for i and j is applied as described above. This procedure, illustrated in figure 4.2, is repeated for each resonance position where $f_m > 0$ and $0 < d_m < D$, and the magnetic axis at $\hat{r} = 0$ and the separatrix at $\hat{r} = 1$ are treated like resonances for which no further reduction of points is possible. However, due to the usually steep increase of q towards the separatrix, resonance positions become more densely packed. Once the distance between them is too low for the fine regions and some transition region, i.e.,

$$\hat{r}_m - \hat{r}_{m-1} < \left(L_m - \frac{1}{2} + f_m\right) d_m + \left(L_{m-1} - \frac{1}{2} + f_{m-1}\right) d_{m-1}, \tag{4.44}$$

the refinement is not applied to m and all higher resonances. Instead, the procedure for the coarse region is applied directly after the last fine region is constructed, i.e.,

$$\Delta = 1 - \left(\hat{r}_{m-1} + \left(L_{m-1} - \frac{1}{2} + f_{m-1}\right) d_{m-1}\right). \tag{4.45}$$

The subintervals on the unit interval resulting from this entire procedure are shown in figure 4.3.

In a sense, the "optimal" distribution of points on a given flux surface cross-section is one that yields triangles with edges of roughly equal length. While this is not equivalent to the Delaunay triangulation which maximises the minimal interior angle of all triangles, it allows for a simple estimate. In the field aligned-mesh, we can distinguish two types of edges. *Poloidal* edges connect two adjacent points on the same cross-section, i.e., in *poloidal* direction, and *radial* edges connect two points on adjacent cross-section, i.e., roughly in *radial* direction. Given the circumference C_i of cross-section i from (4.13), the average length of poloidal edges connecting N_i points is

$$\bar{l}_i^{\mathrm{pol}} = \frac{C_i}{N_i}. \tag{4.46}$$

For the radial edges, we assume an appropriately averaged distance to the adjacent cross-section(s) $\overline{\Delta r_i}$ as the altitude of the triangle. For an equilateral triangle, which serves as a

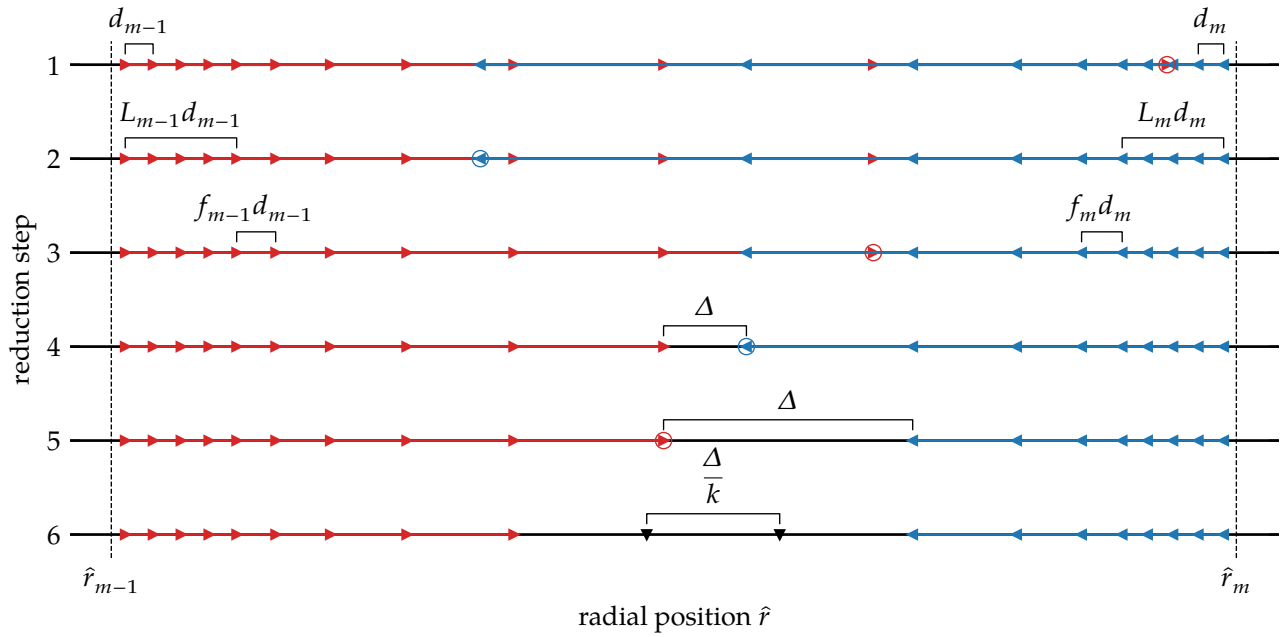

Figure 4.2: Radial refinement procedure, progressing from top to bottom. The dashed vertical lines to the left and right indicate the positions of the resonances. The right-pointing red triangles and the left-pointing blue triangles indicate the positions according to (4.37) and (4.38) surrounding each resonance, i.e., $\hat{r}_{+j,m-1}$ and $\hat{r}_{-i,m}$. The circles indicate the position that is removed in each iteration step according to the criterion in (4.41). Since d_m and f_m are quite similar to d_{m-1} and f_{m-1}, i and j are reduced in an alternating fashion. Starting from step 4, Δ as specified in (4.40) is positive, i.e., the transition regions do not overlap any more. Since the criterion (4.43) is still not fulfilled, the reduction scheme continues until step 6, where it is fulfilled with $k = 3$. The resulting equidistant positions are indicated by the down-pointing black triangles. As a result, step 4 and 6 contain the same number of positions, but their distribution is more balanced after step 6. Note that D is almost as large as the distance between the resonances, thus N_m and N_{m-1} from (4.39) are so large that the resulting positions would extend beyond the adjacent resonance. For illustration purposes, these positions and the iteration steps necessary to remove them are skipped.

rough average over all triangle shapes, this results in the edge length

$$\bar{l}_i^{\mathrm{rad}} = \frac{\overline{\Delta r}_i}{\sin 60°}. \tag{4.47}$$

Equating the average poloidal and radial edge lengths yields the number of points on cross-section i as

$$N_i = \frac{2}{\sqrt{3}} \frac{C_i}{\overline{\Delta r}_i}, \tag{4.48}$$

which is then rounded to the closest multiple of 2 in order to allow combining triangles to quadrangles for later use with Gorilla [16]. However, due to the dependence on $\overline{\Delta r}_i$, N_i in (4.48) scales linearly with the density of the radial positions, i.e., if the number of cross-

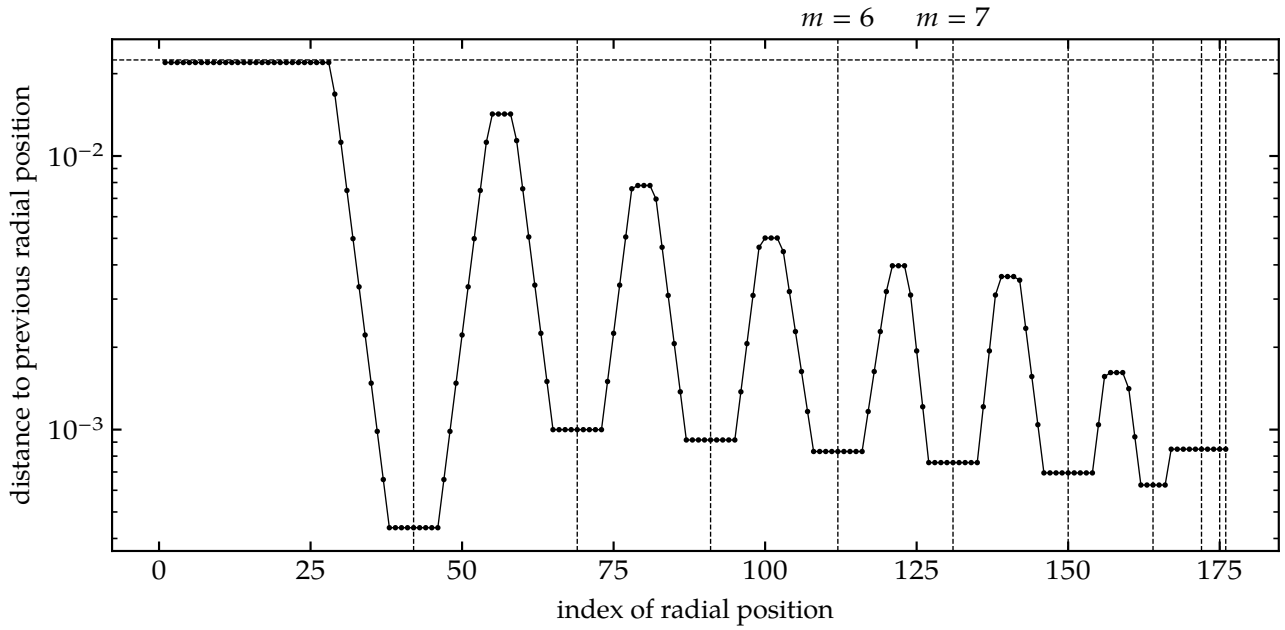

Figure 4.3: Distances between radial positions resulting from the radial refinement procedure described in figure 4.2. The dashed vertical lines indicate resonances from $m = 3$ to $m = 12$, but refinement is only performed up to $m = 9$. The dashed horizontal line shows the maximum distance D and the horizontal lines of the fine and coarse regions lie at their corresponding d_m and $\frac{\Delta}{k}$, respectively. Note that the distances are plotted over their index and not over their position because the markers would become indistinguishable in the finer regions. Combined with logarithmic scaling, the constant slope then indicates the factor f_m of the corresponding geometric series in the transition regions. For the resonances $m = 6$ and $m = 7$, which are the ones used in figure 4.2, factors are set to 1.4 and 1.6, respectively, while all others are set to 1.5. Data is taken from ASDEX Upgrade shot #33353 at 2325 ms with $n = 2$.

section is doubled due to radial refinement, the total number of points is roughly quadrupled. Since the variation of the interpolated quantities is much higher in radial direction than in poloidal direction, this increases the size of the linear systems to be solved without an accompanying gain in accuracy. As a compromise, we replace the averaged distance of adjacent cross-sections by its geometric average with the maximum distance D used in the radial refinement process:

$$N_i = \frac{2}{\sqrt{3}} \frac{C_i}{\sqrt{\overline{\Delta r}_i D}}. \tag{4.49}$$

For $\overline{\Delta r}_i$, we don't use the same radial coordinate as for radial refinement, i.e., the distance along the horizontal line extending from the magnetic axis outwards. Due to the Shafranov shift and the ellipticity of the cross-sections, it is close to the minimum distance between cross-sections. A better approximation to the average distance between cross-sections is the *small radius*, i.e., the radius of a circle with the same area A_i as the cross-section i, given by (4.12). Using half-grid quantities (see section 4.1) to average over the inner and outer

adjacent cross-sections, we get

$$\overline{\Delta r}_i = \bar{r}_{i+\frac{1}{2}} - \bar{r}_{i-\frac{1}{2}} = \sqrt{\frac{A_{i+\frac{1}{2}}}{\pi}} - \sqrt{\frac{A_{i-\frac{1}{2}}}{\pi}}, \tag{4.50}$$

except for the last cross-section N, which has only one adjacent cross-section, where we use $\overline{\Delta r}_N = \bar{r}_N - \bar{r}_{N-1}$ instead. Similar reasoning applies to the poloidal distribution of the N_i points. To roughly achieve the *average* edge length from (4.46), they would need to be placed equidistantly in *equal-arclength* poloidal angle. However, the *actual* length of a particular radial edge scales with the *actual* radial distance from the adjacent cross-section in its vicinity, and so does the length of the subtended arc. The latter in turn approximates the *actual* length of the poloidal edge nearby. Accordingly, using this rough estimation, the N_i points are spaced equidistantly in the *geometric* poloidal angle θ, which is also obtained more easily.

Now that the number of points and their positions are fixed, the constrained Delaunay triangulation can proceed as illustrated in figure 4.4. It is constrained because we impose the poloidal edges and only need to determine the radial edges connecting points on adjacent cross-sections. We start with a fixed radial edge, namely the one lying on the horizontal line extending outwards from the magnetic axis, which is also the $\theta = 0$ line. From there, we can construct a triangle either by connecting the point on the inner cross-section with the next point on the outer cross-section, or by connecting the point on the outer cross-section with the next point on the inner cross-section. These four points form a quadrangle whose diagonals are the two candidates for the next radial edge. Exactly one of the two possible triangles fulfills the Delaunay condition, i.e., the fourth point lies outside the circumcircle of the other three points[1]. If the three points comprising the triangle are numbered in counter-clockwise order, the condition can be written as

$$\det \begin{bmatrix} R_1 - R_4 & Z_1 - Z_4 & (R_1 - R_4)^2 + (Z_1 - Z_4)^2 \\ R_2 - R_4 & Z_2 - Z_4 & (R_2 - R_4)^2 + (Z_2 - Z_4)^2 \\ R_3 - R_4 & Z_3 - Z_4 & (R_3 - R_4)^2 + (Z_3 - Z_4)^2 \end{bmatrix} \leq 0. \tag{4.51}$$

The edge thus selected serves as the starting edge of the next quadrangle, and this selection process is repeated until the last triangle, which contains the starting edge at $\theta = 0$ and closes the loop. In contrast to unconstrained Delaunay triangulation, this algorithm proceeds in linear time with respect to the number of triangles, since no revision of already constructed triangles by edge flipping is necessary. In principle, it can be parallelized over the cross-sections because the selection process is independent of the neighbouring triangle loop. An illustration of the resulting mesh can be seen in figure 4.5.

Concerning the numbering of the points, edges, and triangles, we make the following observations. We number the flux surface cross-sections from 0 for the magnetic axis, a degenerate

[1] In the unlikely event that the four points form a cyclic quadrilateral, i.e., the fourth point lies exactly on the circumcircle of the other three points, *both* triangles fulfill the Delaunay condition and the choice is arbitrary.

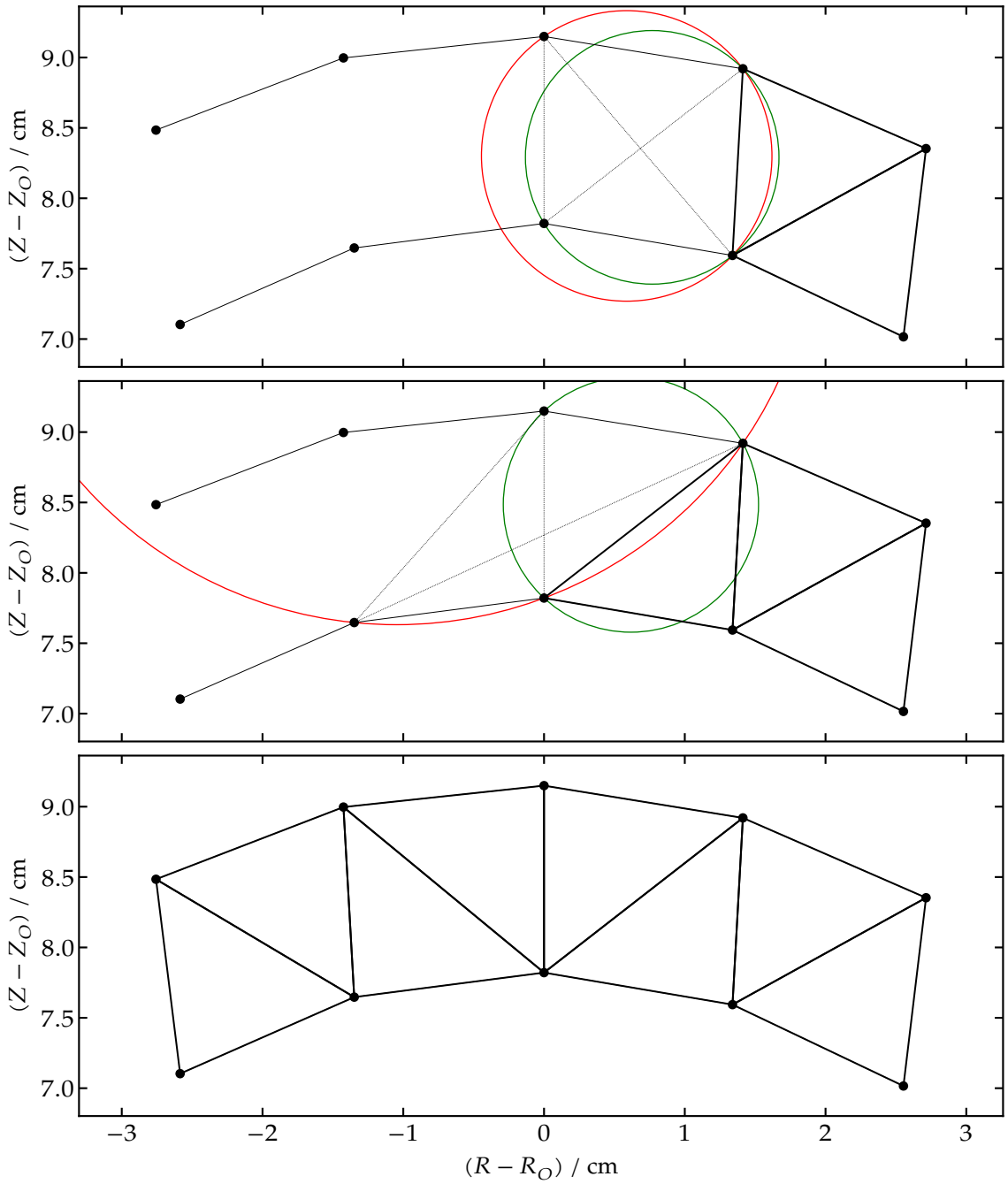

Figure 4.4: Constrained Delaunay triangulation, proceeding from the top to the bottom. A subset of points of two adjacent cross-sections is shown, situated slightly above the magnetic axis at (R_O, Z_O). The poloidal edges are already connected and the triangulation proceeds in counter-clockwise direction, i.e., from right to left. The thick lines show the triangles which have been constructed previously. The thin dotted lines indicate the quadrangle formed by including the next point of each cross-section, as well as its diagonals. In the top plot, the circumcircles of the two candidate triangles are shown in green and red. The green circle fulfills the Delaunay condition (4.51) as it encloses no fourth point. This triangle is selected and its edge is used as the starting edge in the middle plot, where the same procedure is applied again. The bottom plot shows the resulting triangulation for the given point set.

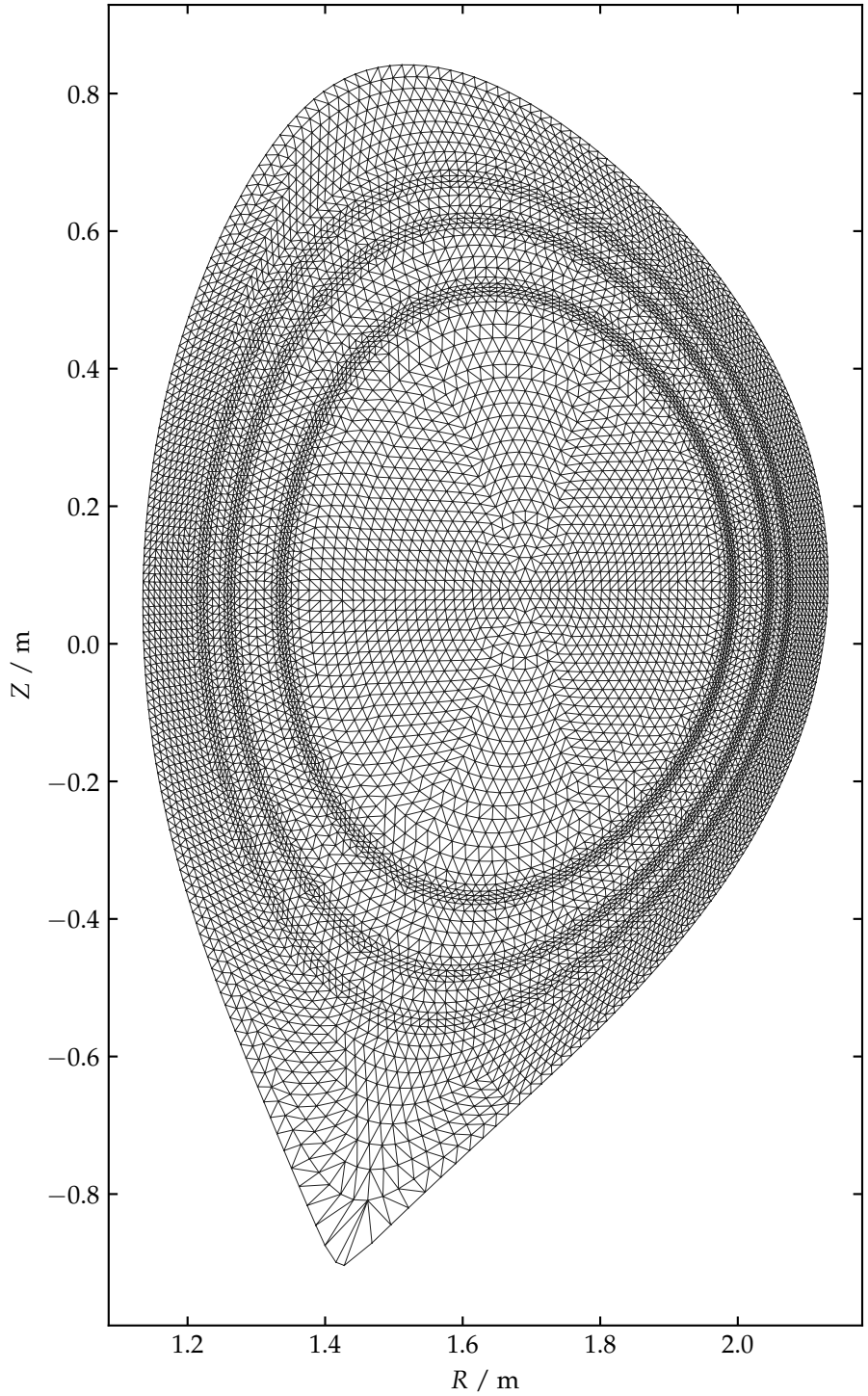

Figure 4.5: Example of a mesh resulting from the procedure described in section 4.4. For illustration purposes, a rather coarse radial separation of $D = 1.25\,\mathrm{cm}$ is used and only the resonances $(m, n) = (-3, 2), (-4, 2), (-5, 2)$ are considered in the refinement. With parameters $d = 0.35\,\mathrm{cm}, f = 1.5, L = 1$, the resulting mesh consists of 53 flux surface cross-sections, 18774 triangles, and 9531 vertices. A variant of this figure has already been published [2].

flux surface, to N^{ϱ} for the last closed flux surface[1]. The number of points on flux surface i is given by N_i^{P}, determined as previously described, and the total number of points is then

$$N^{\mathrm{P}} = \sum_{i=0}^{N^{\varrho}} N_i^{\mathrm{P}}. \tag{4.52}$$

Points are numbered in the order they are created (see above), i.e., starting at $\vartheta = 0$ and going counter-clockwise, then continuing with the next flux surface. Saving these values as a jagged array allows conversion between the *local* point number (here referring to the flux surface) and the *global* point number (here referring to the entire mesh). Next, we consider the number of triangles $N_i^{\triangle}$ between[2] flux surface cross-sections i and $i-1$. Each poloidal edge belongs to one triangle, and the number of poloidal edges on a cross-section is the same as the number of points thus connected, yielding

$$N_i^{\triangle} = N_i^{\mathrm{P}} + N_{i-1}^{\mathrm{P}}, \tag{4.53}$$

except for $i = 1$, where we have to subtract 1 to account for the lack of edges connecting the only point at $i = 0$ to itself. The total number is then

$$N^{\triangle} = 2N^{\mathrm{P}} - N_{N^{\varrho}}^{\mathrm{P}} - 1. \tag{4.54}$$

Triangles are numbered in the same manner as points. Finally, the number of triangles is the same as the number of radial edges, which taken together with the number of poloidal edges gives the total number of edges as

$$N^{\mathrm{e}} = N^{\triangle} + N^{\mathrm{P}} - 1 = 3N^{\mathrm{P}} - N_{N^{\varrho}}^{\mathrm{P}} - 2. \tag{4.55}$$

The distinction between radial and poloidal edges is also reflected in their numbering scheme. We start numbering with the poloidal edges in the same manner as the points associated with them, i.e., $i^{e,\mathrm{pol}} = i^{P} - 1$, again because the point at the magnetic axis has no poloidal edge. Then we continue with all the radial edges in the same manner as the triangles associated with them, i.e., $i^{e,\varrho} = N^{\mathrm{P}} - 1 + i^{\triangle}$.

Mapping between these indices is achieved by filling appropriate arrays during construction of the mesh. This leaves us with one last task concerning the mesh: finding the triangle containing a given point P. From the bounding boxes, i.e., the extent of each triangle in R and Z, we can construct an R* tree. Querying this tree with the coordinates of P yields a list of triangle indices in whose bounding box P is contained. We can then check individually for each of these triangles whether it contains P as follows. Assume the edge vectors $\boldsymbol{l}_k$ all point in counter-clockwise direction and the normal vectors $\boldsymbol{n}_k$ all point outwards (see figure 4.1c). Construct the vectors $\boldsymbol{p}_k$ pointing from P_k, the initial point of the $\boldsymbol{l}_k$, to P. The dot product

[1] This is also the numbering scheme used for the full-grid values mentioned in section 4.1.
[2] This is also the numbering scheme used for the half-grid values mentioned in section 4.1.

$\boldsymbol{p}_k \cdot \boldsymbol{n}_k$ is negative if P lies to the left of $\boldsymbol{l}_k$. If it is negative for all three edges, P lies inside the triangle. However, due to numerical inaccuracies, this test might fail for *both* triangles sharing an edge if P is close to that edge. To have the test succed for at least one triangle, assign a finite thickness ε to edges. Then compute the distance between the line segment and P as

$$d_k^2 = \begin{cases} \boldsymbol{p}_k \cdot \boldsymbol{p}_k & \text{if } 0 < \boldsymbol{p}_k \cdot \boldsymbol{l}_k, \\ \boldsymbol{p}_k \cdot \boldsymbol{p}_k - \frac{\boldsymbol{p}_k \cdot \boldsymbol{l}_k}{\boldsymbol{l}_k \cdot \boldsymbol{l}_k} & \text{if } 0 \leq \boldsymbol{p}_k \cdot \boldsymbol{l}_k \leq \boldsymbol{l}_k \cdot \boldsymbol{l}_k, \\ \boldsymbol{p}_{k+1} \cdot \boldsymbol{p}_{k+1} & \text{if } \quad \boldsymbol{p}_k \cdot \boldsymbol{l}_k > \boldsymbol{l}_k \cdot \boldsymbol{l}_k, \end{cases} \tag{4.56}$$

where we assumed $\boldsymbol{p}_4 \equiv \boldsymbol{p}_1$ for simplicity. If $d_k < \varepsilon$, P lies on the line segment with thickness ε and the test succeeds.

Finally, to solve for $\boldsymbol{B}_n$ with the method presented in section 2.1, we would need to impose a homogeneous Dirichlet boundary condition at infinity. A Poincaré-Steklov operator, or Dirichlet-to-Neumann map, would allow us to transform this to an inhomogeneous Neumann boundary condition on the actual boundary of the computational domain, which could be used in conjunction with (2.89). Until this is implemented, we circumscribe the mesh of the core plasma[1] with an ellipsis, use Triangle [21] for Delaunay triangulation connecting the two boundaries, and impose a homogeneous Dirichlet boundary condition on the outer boundary via (2.78). As Albert et al. [7] note: "If [the computational domain] is chosen with a large enough current-free region around the actual domain of interest, this description is suited to approximately describe the decay of the magnetic field at infinite distance."

4.5 Magnetic Differential Equations

To solve the MDEs (2.113) and (2.122), we apply a lowest-order finite difference scheme. We approximate $\boldsymbol{B}_0^{\mathrm{pol}} \cdot \nabla_{\mathrm{pol}} p_n$ as a directional derivative along a poloidal edge $\boldsymbol{l}_k$ pointing from node $\boldsymbol{r}_k$ to node $\boldsymbol{r}_{k+1}$ on the same flux surface cross-section, which in turn we approximate as a difference quotient,

$$\boldsymbol{B}_0^{\mathrm{pol}}(\boldsymbol{l}_k) \cdot \nabla_{\mathrm{pol}} p_n(\boldsymbol{l}_k) \approx \boldsymbol{B}_0^{\mathrm{pol}}(\boldsymbol{l}_k) \cdot \frac{\partial p_n}{\partial \boldsymbol{l}_k}(\boldsymbol{l}_k) \approx \boldsymbol{B}_0^{\mathrm{pol}}(\boldsymbol{l}_k) \cdot \frac{\boldsymbol{l}_k}{l_k} \frac{p_n(\boldsymbol{r}_{k+1}) - p_n(\boldsymbol{r}_k)}{l_k}, \tag{4.57}$$

where $(\boldsymbol{l}_k)$ signifes evaluation at the edge midpoint. We accordingly approximate $p_n(\boldsymbol{l}_k) \approx \frac{1}{2}(p_n(\boldsymbol{r}_{k+1}) - p_n(\boldsymbol{r}_k))$, which is actually exact for linear interpolation according to (4.34), and the discretized MDE then reads

$$\boldsymbol{B}_0^{\mathrm{pol}} \cdot \frac{\boldsymbol{l}_k}{l_k} \frac{p_n(\boldsymbol{r}_{k+1}) - p_n(\boldsymbol{r}_k)}{l_k} + \frac{\mathrm{i}n}{R} B_0^{\mathrm{tor}} \frac{p_n(\boldsymbol{r}_{k+1}) + p_n(\boldsymbol{r}_k)}{2} = -p_0'(\psi) B_n^{\psi}, \tag{4.58}$$

[1] or the entire vacuum vessel in future versions

where the evaluation point is the edge midpoint unless indicated otherwise. Reordering in terms of the unknowns, i.e., degrees of freedom $p_n(\boldsymbol{r}_k)$ yields

$$(b_k - a_k)p_n(\boldsymbol{r}_k) + (b_k + a_k)p_n(\boldsymbol{r}_{k+1}) = s_k \tag{4.59}$$

with

$$a_k = \boldsymbol{B}_0^{\text{pol}}(\boldsymbol{l}_k) \cdot \frac{\boldsymbol{l}_k}{l_k^2}, \qquad b_k = \frac{1}{2}\frac{\mathrm{i}n}{R(\boldsymbol{l}_k)} B_0^{\text{tor}}(\boldsymbol{l}_k), \qquad s_k = -p_0'(\psi) B_n^{\psi}(\boldsymbol{l}_k). \tag{4.60}$$

Note that the damping by (2.137) is accomodated by supplying an appropriately modified b_k. Now, setting up the equations for all N poloidal edges of a discretized flux surface and applying periodic boundary conditions results in a linear system of equations of the form $[K_{ij}][p_n(\boldsymbol{r}_j)] = [s_i]$ with $K_{ij} = (b_i - a_i)\delta_{i,j} + (b_i - a_i)\delta_{i,(j \bmod N)+1}$, or, in matrix form,

$$\hat{K} = \begin{bmatrix} b_1 - a_1 & b_1 + a_1 & 0 & \dots & 0 \\ 0 & b_2 - a_2 & b_2 + a_2 & \dots & 0 \\ 0 & 0 & b_3 - a_3 & \dots & 0 \\ \vdots & \vdots & \vdots & \ddots & \vdots \\ b_N + a_N & 0 & 0 & \dots & b_N - a_N \end{bmatrix}. \tag{4.61}$$

Note that this sparse matrix is weakly diagonally dominant since a_k is purely real and b_k is purely imaginary. The linear system of equations can be solved with a direct solver like UMFPACK [22]. To solve for $\frac{J_n^{\parallel}}{B_0}$ instead of p_n, we simply have to replace s_k by the right-hand side of (2.122). Since (2.133) differs from (2.112) only in the coefficients, we can apply the same approach using the chain rule

$$\frac{\partial}{\partial \vartheta} = \frac{\partial R}{\partial \vartheta}\frac{\partial}{\partial R} + \frac{\partial Z}{\partial \vartheta}\frac{\partial}{\partial Z} = \frac{\partial \boldsymbol{r}_{\text{pol}}}{\partial \vartheta} \cdot \nabla_{\text{pol}}, \tag{4.62}$$

resulting in

$$a_k = \frac{\partial \boldsymbol{r}_{\text{pol}}}{\partial \vartheta}(\boldsymbol{l}_k) \cdot \frac{\boldsymbol{l}_k}{l_k^2}, \quad b_k = -\frac{1}{2}\frac{\mathrm{i}n}{B_{0\varphi}}\frac{\partial \boldsymbol{r}_{\text{pol}}}{\partial \vartheta}(\boldsymbol{l}_k) \cdot \boldsymbol{B}_0^{\text{pol}}(\boldsymbol{l}_k), \quad s_k = \sum_{m \in m_{\text{res}}} \frac{\mathrm{i}(nq + m)}{B_{0\varphi}} \left(\frac{J_n^{\parallel}}{B_0}\right)_m \mathrm{e}^{\mathrm{i}m\vartheta(\boldsymbol{l}_k)}. \tag{4.63}$$

Finally, note that all the a_k and b_k only depend on equilibrium quantities and thus stay constant across iteration steps; only the s_k need to be updated.

4.6 Arnoldi Iterations

ARPACK [23] and similar numerical packages implementing the Arnoldi iteration mentioned in chapter 2 are designed to compute a fixed number of extremal eigenvalues, but in our case, the number r of eigenvalues above the threshold λ_{sup} is not known beforehand. To

Algorithm 1 Arnoldi iteration with breaking conditions

Input: operator $\hat{K}$, start vector $\boldsymbol{q}_0$, maximum dimension of Krylov subspace $k_{\max}$, threshold of eigenvalue magnitude $\lambda_{\sup}$, *tolerance* in convergence estimation

Output: Ritz values $\lambda_1, \dots, \lambda_r$, Ritz vectors $\boldsymbol{v}_1, \dots, \boldsymbol{v}_r$

$s_1 \leftarrow 0$
$\boldsymbol{q}_1 \leftarrow \frac{\boldsymbol{q}_0}{\|\boldsymbol{q}_0\|}$
for $k \leftarrow 1, \dots, k_{\max}$
    $\boldsymbol{q}_{k+1} \leftarrow \hat{K}\boldsymbol{q}_k$
    for $j \leftarrow 1, \dots, k$
        $H_{j,k} \leftarrow \boldsymbol{q}_j^* \cdot \boldsymbol{q}_{k+1}$
        $\boldsymbol{q}_{k+1} \leftarrow \boldsymbol{q}_{k+1} - H_{j,k}\boldsymbol{q}_j$
    $H_{k+1,k} \leftarrow \|\boldsymbol{q}_{k+1}\|$
    if $H_{k+1,k} \approx 0$ **break**
    $\boldsymbol{q}_{k+1} \leftarrow \frac{\boldsymbol{q}_{k+1}}{H_{k+1,k}}$
    $\lambda_1, \dots, \lambda_k \leftarrow \mathit{HessenbergEigenvalues}(H_{1,1}, \dots, H_{k,k})$
    $r \leftarrow \max r \,:\, \lambda_r \geq \lambda_{\sup}$
    if $\frac{|\lambda_j - s_j|}{|\lambda_j|} < \mathit{tolerance}\ \forall j \leq r$ **break**
    $s_1, \dots, s_k \leftarrow \lambda_1, \dots, \lambda_k$
$\boldsymbol{u}_1, \dots, \boldsymbol{u}_r \leftarrow \mathit{HessenbergEigenvectors}(H_{1,1}, \dots, H_{k,k}; \lambda_1, \dots, \lambda_k; r)$
$\boldsymbol{v}_1, \dots, \boldsymbol{v}_r \leftarrow \mathit{MatrixMultiplication}(\boldsymbol{q}_1, \dots, \boldsymbol{q}_k; \boldsymbol{u}_1, \dots, \boldsymbol{u}_r)$

circumvent this problem, our implementation uses this fixed number as the maximum number of iterations as well as for memory allocations, and exits early if convergence is reached. This requires roughly three times as many iteration steps as there are Ritz values above the threshold. To estimate convergence, we compute the Ritz values after each Arnoldi iteration step and compare them with the Ritz values saved in the previous iteration step. The complete approach is given as pseudocode in algorithm 1, where we assume that eigenvalues are sorted by magnitude in descending order to simplify the mathematical notation, while the actual implementation uses masked arrays. The LAPACK routines `ZHSEQR` and `ZHSEIN` are used to compute the eigenvalues and eigenvectors of the Hessenberg matrix, respectively.

With $\hat{\Lambda}_r$ and $\hat{V}_r$ now known, $\hat{I}\hat{\Pi}$ from (2.24) can in principle be computed. First, we compute the inverse of

$$\hat{L}_r = \hat{V}_r^\dagger \hat{V}_r (\hat{\Lambda}_r - \hat{I}) \tag{4.64}$$

by solving for $\hat{Y}_r$ in $\hat{L}_r \hat{Y}_r = \hat{I}$ with the LAPACK routine `ZGESV`. Note that N is usually larger than r by a factor of 10^4. Since $\hat{I}\hat{\Pi}$ is a dense $N \times N$ matrix, it would become prohibitively large to keep in memory, so we only keep the $N \times r$ matrix $\hat{V}_r$ and the $r \times r$ matrix $\hat{\Lambda}_r \hat{L}_r^{-1}$, and

perform repeated matrix–vector multiplication from the right,

$$\hat{I}\hat{1}\delta\boldsymbol{B} = \hat{V}_r\hat{\Lambda}_r\hat{L}_r^{-1}\hat{V}_r^{\dagger}\delta\boldsymbol{B}. \tag{4.65}$$

With this time–memory tradeoff, runtime scales with $O(N^2r^4)$ instead of $O(N^2)$, but it is still negligible compared to other computations performed in each iteration step.

To estimate the convergence of preconditioned iteration steps of (2.13), we consider the difference between successive values of $\delta\boldsymbol{B}$, i.e., $\delta\boldsymbol{B}^{[k]} - \delta\boldsymbol{B}^{[k-1]}$. Its L^2 norm should approximately follow a geometric series, whose convergent major is the geometric series in λ_{sup}:

$$\left\|\delta\boldsymbol{B}^{[k]} - \delta\boldsymbol{B}^{[k-1]}\right\|_2 \leq \left\|\delta\boldsymbol{B}^{[0]}\right\|_2 \lambda_{\text{sup}}^k. \tag{4.66}$$

$\delta\boldsymbol{B}$ reduces to $\boldsymbol{B}_n$, whose representation is discussed in section 4.3. The L^2 norm is then given by (4.33), albeit only for the poloidal component. However, the toroidal component fully depends on the poloidal component via (4.31), so in a sense, no information is missing when the toroidal component is omitted from essentially two-dimensional finite element area integral. Moreover, it seems that the relative error computed from the (numerical) L^2 integral of the toroidal component is bounded from below[1], possibly because the toroidal component is constant on each triangle while the poloidal component varies linearly.

4.7 Conversion between Conventions

There are more choices in the coordinate systems than we have discussed in section 1.1 and the coordinate conventions COCOS suggested by Sauter and Medvedev [24] are very useful for this kind of derivations. The GEQDSK format [15] detailed in section 4.1 explicitly specifies that (R, φ, Z) is a right-handed system, meaning $\sigma_{R\varphi Z} = +1$ in COCOS. The units of ψ are given as $\mathrm{Wb\,rad^{-1}}$, implying the poloidal flux is divided by 2π, thus setting $e_{B^{\text{pol}}} = 0$ in COCOS. We have made the same choices in section 1.1 and this leaves us with valid COCOS indices 1, 3, 5 or 7. With (1.2), we already implicitly fixed the sign $\sigma_{B^{\text{pol}}} = -1$ as well, thus using COCOS indices 3 or 7 with

$$B_0^{\text{pol}} = \nabla\psi \times \nabla\varphi. \tag{4.67}$$

This means that radially increasing ψ ($\sigma_{\psi'} = +1$) corresponds to a counter-clockwise poloidal magnetic field, and radially decreasing ψ ($\sigma_{\psi'} = -1$) corresponds to a clockwise poloidal magnetic field. However, $\sigma_{B^{\text{pol}}}$ is not directly available from GEQDSK data, which leaves open the possibility that $\sigma_{B^{\text{pol}}} = +1$ was used implicitly, inverting the sign in (4.67). This has to be decided by inspection of the toroidal current I^{tor} in the GEQDSK header, which is unambiguous because φ is fixed: a positive toroidal current produces a clockwise poloidal

[1] see figure 5.12, where inclusion of the toroidal component would result in a constant relative error (a horizontal line) after initially following the geometric series

magnetic field, and a negative toroidal current produces a counter-clockwise poloidal magnetic field. This means that the sign of the given ψ might need to be swapped to ensure consistency[1].

Finally, in a similar manner as before, we already fixed $\sigma_{\varrho\vartheta\varphi} = -1$ by defining ϑ to turn counter-clockwise in (1.6), leaving us with COCOS index 3. Again, this choice is not represented directly in GEQDSK data, and it might affect the sign of q. If I^{tor} and B^{tor} point in the same direction, the magnetic field lines form a right-handed helix (going against the direction of ϑ) and q is negative, and if I^{tor} and B^{tor} point in opposite directions, the magnetic field lines form a left-handed helix (going along the direction of ϑ) and q is positive.

To summarize, we impose COCOS index 3 and adapt the sign of some GEQDSK data if necessary, according to the information given in the file header. In the overview (4.68), where we included the Jacobian from (1.7), the signs on the left of the vertical line determine the signs to the right. Note that p is assumed to monotonically decrease radially outwards.

B^{tor}	I^{tor}	q	$\sigma_{\psi'}$	F	$p'(\psi)$	$\sqrt{g}$
$+$	$+$	$-$	$-$	$+$	$+$	$+$
$+$	$-$	$+$	$+$	$+$	$-$	$+$
$-$	$+$	$+$	$-$	$-$	$+$	$+$
$-$	$-$	$-$	$+$	$-$	$-$	$+$

(4.68)

Some trade-offs have been made in these choices. We deemed it simpler to keep the coordinates fixed and track the signs of $\sigma_{\psi'}$ and q when necessary. To compare, GPEC [25] operates on a different principle: the direction of φ depends on the helicity, such that q is always positive, i.e., φ points in clockwise direction where q is negative in (4.68). Furthermore, GPEC uses the Fourier series expansion

$$f(\psi, \varphi, \vartheta) = \mathrm{Re} \sum_{n=0}^{\infty} \sum_{m=-\infty}^{\infty} f_{m,n} \mathrm{e}^{\mathrm{i}m\vartheta - \mathrm{i}n\varphi}, \tag{4.69}$$

whereas MEPHIT uses (1.10) and (1.11), which combine to

$$f(\psi, \varphi, \vartheta) = \sum_{m=-\infty}^{\infty} f_{m,0} \mathrm{e}^{\mathrm{i}m\vartheta} + 2\,\mathrm{Re} \sum_{n=1}^{\infty} \sum_{m=-\infty}^{\infty} f_{m,n} \mathrm{e}^{\mathrm{i}m\vartheta + \mathrm{i}n\varphi}. \tag{4.70}$$

Thus, to convert GPEC output $f_{m,n}$ to the conventions of MEPHIT, $f_{m,n}$ has to be halved for $n \neq 0$, and if q is *positive* in MEPHIT, the complex phase and the poloidal mode number swap sign, i.e., $f_{m,n} \to f^*_{-m,n}$. Additionally, when comparing the radial magnetic field perturbation, MEPHIT uses the contravariant density component as discussed in section 2.1, i.e.,

$$\mathcal{B}^{\psi}_{mn} = \left(\sqrt{g}\boldsymbol{B}_n \cdot \nabla\psi\right)_m. \tag{4.71}$$

[1]The sign could also be accounted for in (4.67), but this way a particular COCOS index can be imposed on the given GEQDSK file.

With the configuration `jsurf_out` set to 1, GPEC supplies a similar quantity `Jbgradpsi`, which is defined as

$$\frac{\left(\sqrt{g}B_n^{\perp}|\nabla\psi|\right)_m}{\left\langle\sqrt{g}\,|\nabla\psi|\right\rangle}, \tag{4.72}$$

where the angle brackets indicate a flux surface average and $B_n^{\perp}$ is the component perpendicular to the flux surface; this is not to be confused with our usual notion of the component perpendicular to $\boldsymbol{B}_0$, which generally has non-zero poloidal and toroidal components. The flux surface average has the dimension of area and is roughly proportional to the flux surface area, which has to be accounted for in comparison with results from MEPHIT. The projection to $B_n^{\perp}$ uses a vector that is always pointing radially outwards, whereas the projection with $\nabla\psi$ might point in the opposite direction, meaning that $\sigma_{\psi'}$ has to be included in either MEPHIT or GPEC results. Taken together, (4.72) can then be written as $\sigma_{\psi'}\mathcal{B}^{\psi}_{mn}A^{-1}$. Finally, note that GPEC versions lower than 1.5.0 ignore the vertical offset of the computational domain defined in the GEQDSK format (discussed in section 4.1), which effectively shifts the RMP coils to a different position. This has since been corrected after benchmarking efforts with MEPHIT, the results of which can be seen in figure 5.14.

Chapter 5

Simulation Results

Perceptually uniform colour maps [26] are used in the following visualizations of simulation results.

5.1 Validation and Benchmarking of Fourier-FEM

This section has already been published as part of [1] and contains validation and benchmarking examples for the general method derived in section 2.1, which are otherwise not part of MEPHIT. Note that SI units are used in this section.

Here, we present results for an implementation of the Fourier-FEM approach in cylindrical coordinates $x^1 = Z, x^2 = R, x^3 = \varphi$, whereas the corresponding Cartesian coordinates are denoted (X, Y, Z). First, convergence of the method is shown in a comparison to analytical validation cases. Secondly, the Fourier-FEM is compared to conventional 3D FEM. The implementation of the Fourier-FEM is realized inside FreeFEM [27], while the 3D numerical computations are made with EleFAnT 3D [28]. To discretize the variational formulation, a triangular mesh in the (R, Z) plane is used in FreeFEM, while EleFAnT 3D uses quadratic order hexahedral edge elements in 3D Cartesian coordinates [29]. The test cases are sketched in figures 5.1 and 5.2 and have been inspired by TEAM (testing electromagnetic analysis methods) workshop problems [30].

5.1.1 Convergence Study

Validity and convergence of numerical computations are assessed based on analytical test cases with field components defined in a piecewise manner over cylinder radius R. For the numerical computations boundary values and possible volumetric currents are imposed. In all cases, a default scalar permeability $\mu_\mathrm{r} = 1$ is used that increases to $\mu_\mathrm{r} = 50$ in the cylinder shell $0.4 \leq R < 0.5$ with dimensions as in figure 5.1, but with extension in the Z direction up to the boundaries in order to generate simple analytical cases. All non-zero components are given by numerical value equations for standard SI units in this subsection, and physical components are indicated with coordinate indices in parentheses.

For the case of an axisymmetric $(n = 0)$ longitudinal vector potential $\bar{A}_\varphi$ we introduce an

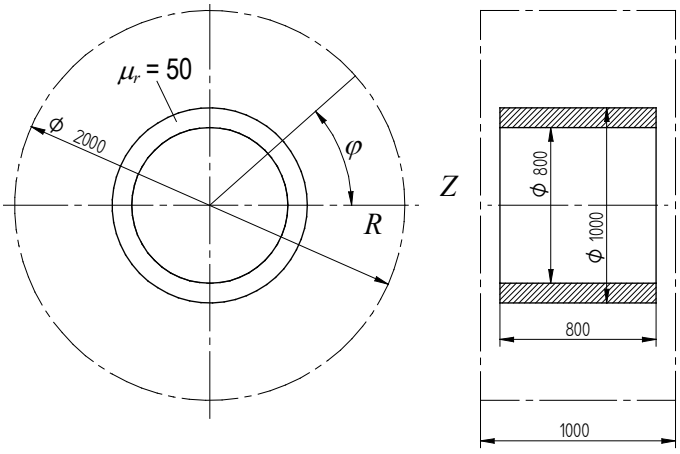

Figure 5.1: Plan (left) and elevation (right) of model problem A: A cylindrical shell with relative permeability $\mu_\mathrm{r} = 50$ surrounded by a domain with $\mu_\mathrm{r} = 1$ in a homogeneous $\boldsymbol{B}$ field in X direction imposing its normal component on the boundary. Measurements are given in units of millimeters.

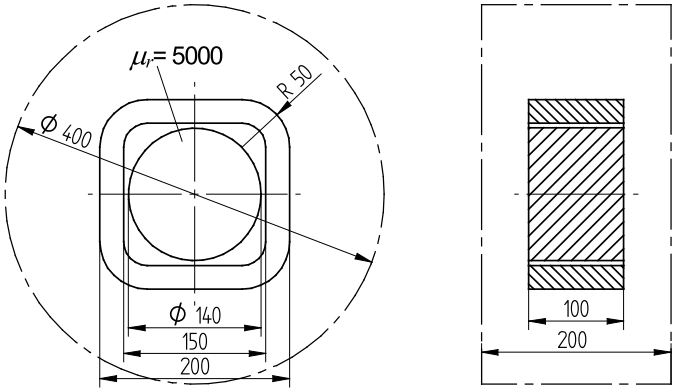

Figure 5.2: Plan (left) and elevation (right) of model problem B: A "racetrack" coil with a cylindrical core of $\mu_\mathrm{r} = 5000$, current flowing counterclockwise, and homogeneous Dirichlet boundary conditions. Measurements are given in units of millimeters and coordinates are the same as in figure 5.1.

analytical magnetic field $\bar{\boldsymbol{b}} \parallel \boldsymbol{e}^Z$ with

$$\bar{\mathcal{B}}^Z = \begin{cases} \frac{52}{25}R - \frac{1}{2}R^3 & (R < 0.4), \\ 100R & (0.4 \leq R < 0.5), \\ 2R & (0.5 \leq R), \end{cases} \tag{5.1}$$

corresponding to

$$\bar{\mathcal{J}}^\varphi = \bar{J}_{(\varphi)} = \begin{cases} R & (R < 0.4), \\ 0 & (R \geq 0.4). \end{cases} \tag{5.2}$$

On the boundaries, we impose homogeneous Neumann conditions at $Z = \pm 0.5$, and an inhomogeneous Neumann condition with $\bar{\mathcal{K}}^\varphi = \bar{H}_Z N_R = 2$ at $R = 1$. Choosing the corre-

sponding Dirichlet condition at $R = 1$ requires knowledge of the difference to the value of $\bar{A}_\varphi$ at $R = 0$, since the Neumann boundaries separate the two Dirichlet boundaries. In this example, we know the full solution and can integrate $\bar{\mathcal{B}}^Z N_Z$ along $Z = -0.5$ or $Z = 0.5$ to set the proper integration constant for the integral. The Dirichlet condition at $R = 1$ is then given by $\bar{A}_\varphi = 5.4132$ and produces results identical to the aforementioned Neumann condition.

A second case for $n = 0$ with a transverse vector potential $\bar{\boldsymbol{a}}$ yielding $\bar{\boldsymbol{B}} \parallel \boldsymbol{e}^\varphi$ is given by

$$\bar{\mathcal{B}}^\varphi = \begin{cases} \frac{1}{2}R & (R < 0.4), \\ 4R^{-1} & (0.4 \leq R < 0.5), \\ \frac{2}{25}R^{-1} & (R \geq 0.5), \end{cases} \tag{5.3}$$

corresponding to

$$\bar{\mathcal{J}}^Z = R\bar{J}_{(Z)} = \begin{cases} R & (R < 0.4), \\ 0 & (R \geq 0.4). \end{cases} \tag{5.4}$$

As an analytical test case for the oscillatory Fourier harmonic $n = 1$, we use a radial field with $\tilde{\boldsymbol{J}} = \boldsymbol{0}$ derived from the vector potential

$$\tilde{\boldsymbol{A}} = \tilde{A}_Z(R) e^{\mathrm{i}n\varphi} \boldsymbol{e}^Z \tag{5.5}$$

with

$$\tilde{A}_Z(R) = \begin{cases} \frac{20000}{128927}R & (R < 0.4), \\ \frac{510000}{128927}R - \frac{78400}{128927}R^{-1} & (0.4 \leq R < 0.5), \\ \frac{106436}{128927}R + \frac{22491}{128927}R^{-1} & (R \geq 0.5), \end{cases} \tag{5.6}$$

resulting in

$$\tilde{\mathcal{B}}^R = R\tilde{B}_{(R)} = \mathrm{i}n\tilde{A}_Z, \qquad \tilde{\mathcal{B}}^\varphi = \tilde{B}_{(\varphi)} = -\frac{\mathrm{d}}{\mathrm{d}R}\tilde{A}_Z, \tag{5.7}$$

Figure 5.3 shows the convergence of the L^2 error in contravariant density components $\mathcal{B}^k$ of the magnetic flux density ($\mathcal{B}^R, \mathcal{B}^Z$ for $n = 0$ longitudinal and $n = 1$ transverse, and $\mathcal{B}^\varphi$ for $n = 0$ transverse) from numerical computations. The convergence rate over degrees of freedom is cubic, as expected from the discretization in the third-lowest order finite element space – Lagrange elements for $\bar{A}_3$ and Nédélec elements for $\boldsymbol{a}$, respectively. As with previous examples, the direct solver UMFPACK [22] is used except for the transverse $n = 0$ part, where the conjugate gradient (CG) method is used. Alternatively, as noted for (2.93), a small non-zero value for n^2 could be used in conjunction with a direct solver. For this particular example, similar results to CG can be achieved with a value of 10^{-9}, while a value of 10^{-8} results in a higher minimum error, and a value of 10^{-10} results in a drastically increasing error past a certain level of refinement. No attempt has been made to estimate a generally "safe" value, and usage of an iterative solver is deemed more numerically robust.

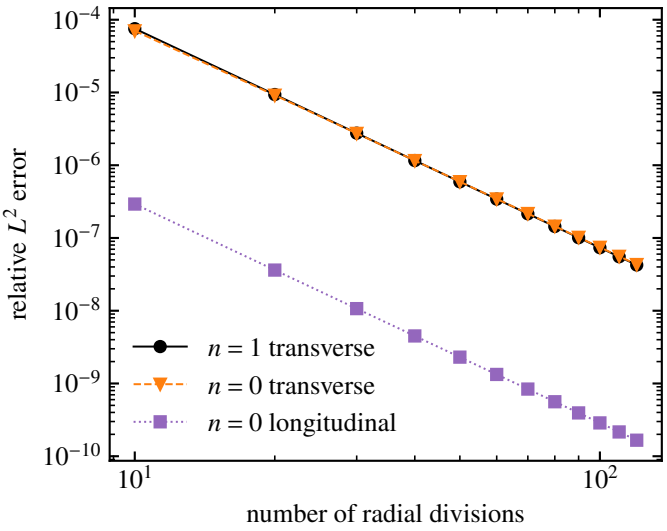

Figure 5.3: Convergence of $\mathcal{B}^k$ from numerical Fourier-FEM computations for analytical test cases. Using third-order finite elements, the relative error decreases cubically with the number of radial divisions, i.e., for edge length h, it is proportional to h^{-3}. The consistently lower relative error for the longitudinal component was not investigated further and thus should not be assumed to be a general feature of the presented approach.

5.1.2 Shielding by a Finite Cylindrical Shell

This test treats magnetic shielding of a finite-height cylindrical shell with relative magnetic permeability $\mu_\mathrm{r} = 50$ compared to the remaining domain, as depicted in figure 5.1. Here we impose a homogeneous $\boldsymbol{B}$ field pointing in the X direction on the boundary via a Dirichlet condition specifying its normal component. Only the $n = 1$ harmonic is required to solve this problem, as cylindrical field components are proportional to $\cos\varphi$ and $\sin\varphi$. The Fourier-FEM computation is compared to a full three-dimensional computation in the code EleFAnT 3D [28]. The Fourier-FEM uses second-lowest order triangular Nédélec elements with vertices on a regular rectangular grid with a spacing of 1 mm and using the up–down symmetry with $Z = 0$ at the symmetry plane. A homogeneous Dirichlet condition is imposed near the cylinder axis at $R = 10^{-31}$ m to obtain a regular solution.

Figure 5.4 shows results of this computation along the radial direction on a cut at $Z = 0$. The agreement is visibly good over a wide range in R and deteriorates near the outer border of the cylindrical shell at $R = 500\,\mathrm{mm}$, where the permeability is discontinuous.

5.1.3 “Racetrack” Coil with Cylindrical Core

The final application is a racetrack-shaped coil with an iron core as depicted in figure 5.2. To be compatible with the Fourier-FEM, the core has to share the coordinate symmetries and is thus limited to a cylindrical shape. In contrast, the current density in the coil can be of arbitrary shape and contributes to different harmonics. This is illustrated in figure 5.5 which shows a stream function T_Z that decreases linearly from the inside to the outside of the coil

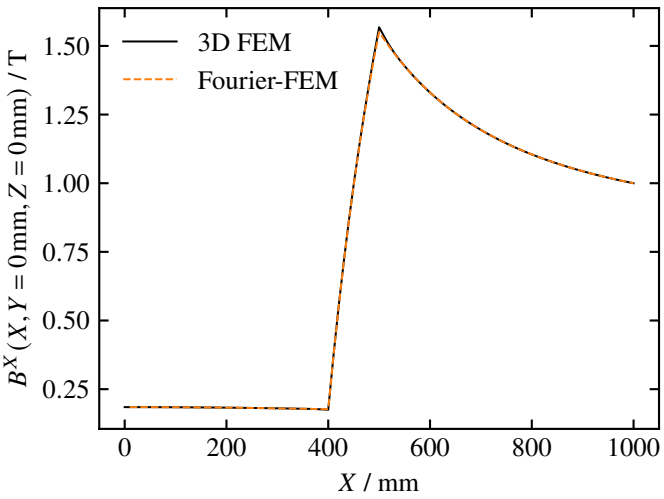

Figure 5.4: Results for model problem A: Magnetic field component B^X along X evaluated at the mid symmetry plane $Z = 0$.

cross-section and is normalized so that the total circulating current amounts to 1 kA. Due to mirror symmetries, only every fourth harmonic ($n = 0, 4, 8, \dots$) is non-zero. Superposition up to $n = 12$ gives a shape in figure 5.6 that is visually indistinguishable from the reference, illustrating the convergence of the Fourier series.

In the numerical computation, grid points are chosen equidistant in R and Z and separated by 1 mm. Brezzi–Douglas–Marini elements of lowest order are used to impose $\tilde{j}$, while $\tilde{a}$ is represented by Nédélec elements of second-lowest order. Lagrange elements of first and second order are used for $\bar{J}^3$ and $\bar{A}_3$, respectively. Figure 5.7 shows the first five non-vanishing harmonics of $\boldsymbol{J}$, decaying with increasing n, as expected.

For homogeneous Dirichlet boundary values, the resulting first five non-zero harmonics of the B^Z component are depicted in figure 5.8. In figure 5.9 the superposition of 17 non-zero harmonics up to $n = 64$ of this result is compared to the reference 3D FEM computation along the Cartesian X coordinate axis. The curves match visually, apart from a slight shift near $R = 70$ mm, at the border of the iron core where the permeability is discontinuous.

5.2 Perturbed Equilibrium Results

The methods presented in chapters 2 to 4 are applied to experimental data of ASDEX Upgrade, specifically shot #33353 at 2.9 s as used by Markl et al. [13]. Figure 5.10 shows the eigenvalue spectrum resulting from the iterative scheme derived in chapter 2. Compared to the full system size of 5×10^5 corresponding to the number of edges in the mesh, the size of the Krylov subspace of 20 to 30 makes the application of the preconditioner (and its computation via roughly 60 to 75 iterations) feasible. The eigenvector associateed with the largest eigenvalue is depicted in figure 5.11. For the pure iMHD model, it attains its largest magnitude around the $(m, n) = (-3, 2)$ rational surface, and the eigenvectors associated with the next few eigenvalues

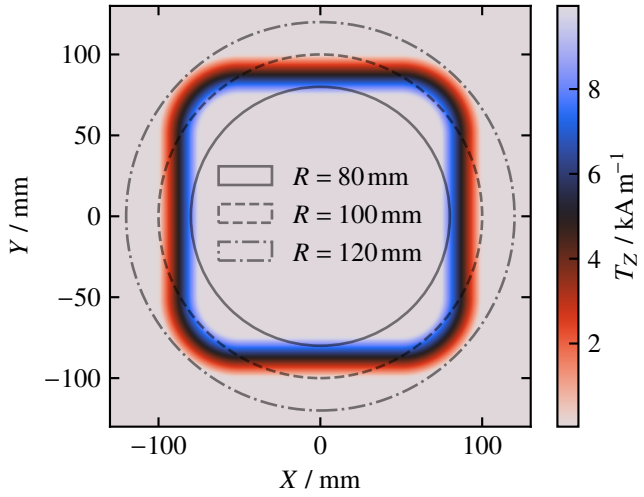

Figure 5.5: Current stream function T_Z and circular cuts at different radii indicated by gray lines, viewed from top.

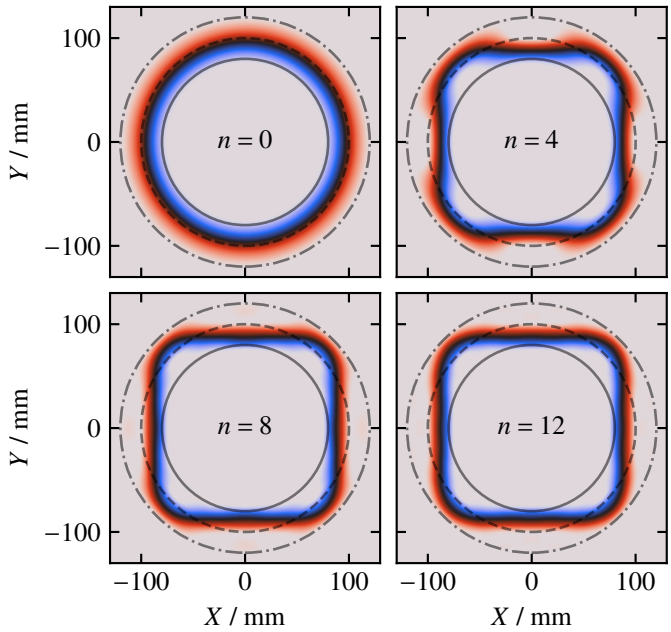

Figure 5.6: Reconstruction of current stream function T_Z in figure 5.5 by Fourier sums up to the harmonic index indicated in the plot.

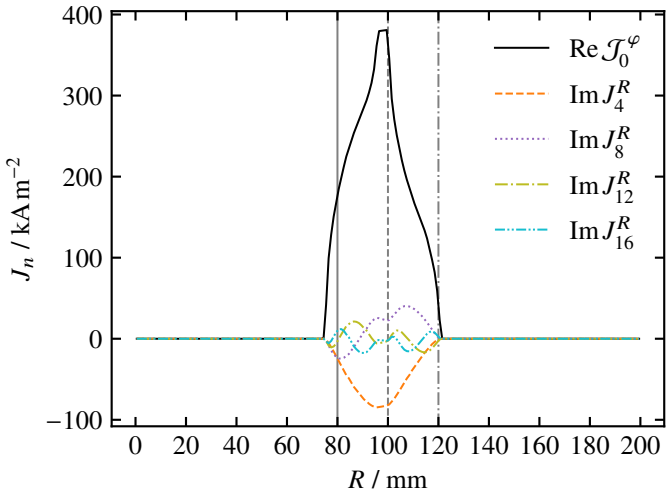

Figure 5.7: Radial dependency of first five non-zero harmonics of current density $\boldsymbol{J}$ at any $|Z| < 50\,\mathrm{mm}$. Vertical lines indicate the cuts shown in figure 5.5.

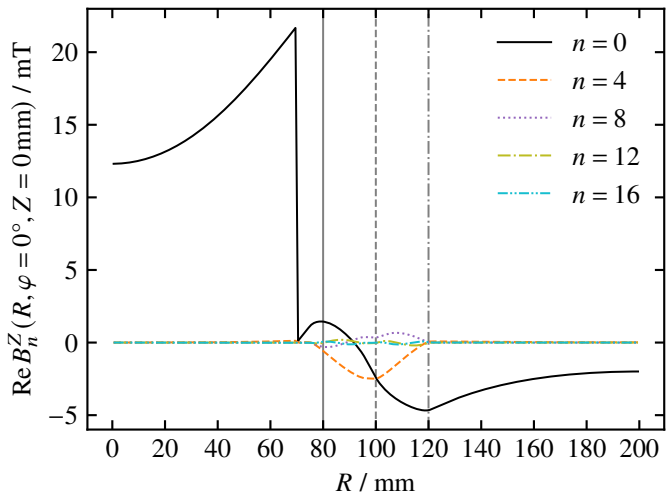

Figure 5.8: Resulting B^Z component from Fourier-FEM: radial dependency of first five non-zero real harmonics. Vertical lines indicate the cuts shown in figure 5.5.

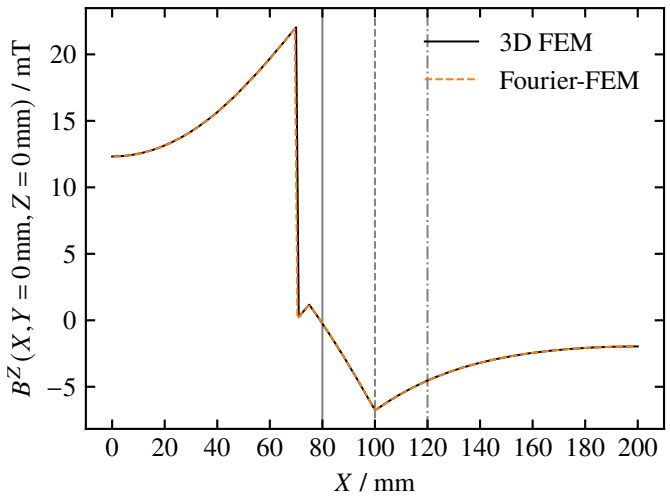

Figure 5.9: Comparison of B^Z between 3D FEM and 2D Fourier-FEM with first 17 non-zero harmonics shows excellent agreement, with only a slight shift at $X = 70\,\mathrm{mm}$ where the permeability is discontinuous. Vertical lines indicate the cuts shown in figure 5.5.

are generally also localized around rational surfaces. The hybrid iMHD/kinetic model instead yields an eigenvector localized around a flux surface close to the magnetic axis for its largest eigenvalue, but otherwise follows the same trend. The convergence behaviour shown in figure 5.12 is what would be expected from the Neumann series (2.6).

Figure 5.13 shows the spectrum of the magnetic field perturbation in poloidal Fourier space over the radial coordinate, visualizing the effects of the plasma response near resonant surfaces. Figure 5.14 shows a few of these poloidal modes separately. It can be seen that the vacuum perturbations of MEPHIT and GPEC agree, but the full perturbation of the pure iMHD models deviate from each other. This is likely due to the fact that the current of finite width imposed by equation (2.141) cannot completely reproduce the behaviour of an infinitesimal current sheet[1]. This might be alleviated by use of XFEM, which allows for basis functions with singularities, but such attempts are beyond the scope of this thesis. Instead, this model is a stepping stone for the hybrid iMHD/kinetic model, which does not exhibit singular current densities in the first place. Moreover, there is still some qualitative discrepancy close to the axis, as can be seen from figure 5.15, which we discuss further in section 5.2.1. The hybrid iMHD/kinetic model yields reduced shielding for the $(m, n) = (-6, 2)$ mode, which is also singled out by Markl et al. [13] as relevant to the discussion about ELM mitigation/suppression in simulations, whereas experiments seem to be more sensitive to the $(m, n) = (-7, 2)$ mode, which appears less affected also in figure 5.14. Isotope effects resulting from the finite Larmor radius expansion are shortly discussed in section 5.2.2.

[1]This assumption is supported by the fact that agreement has already improved compared to previous attempts [2] due to improved approximations in the slab model.

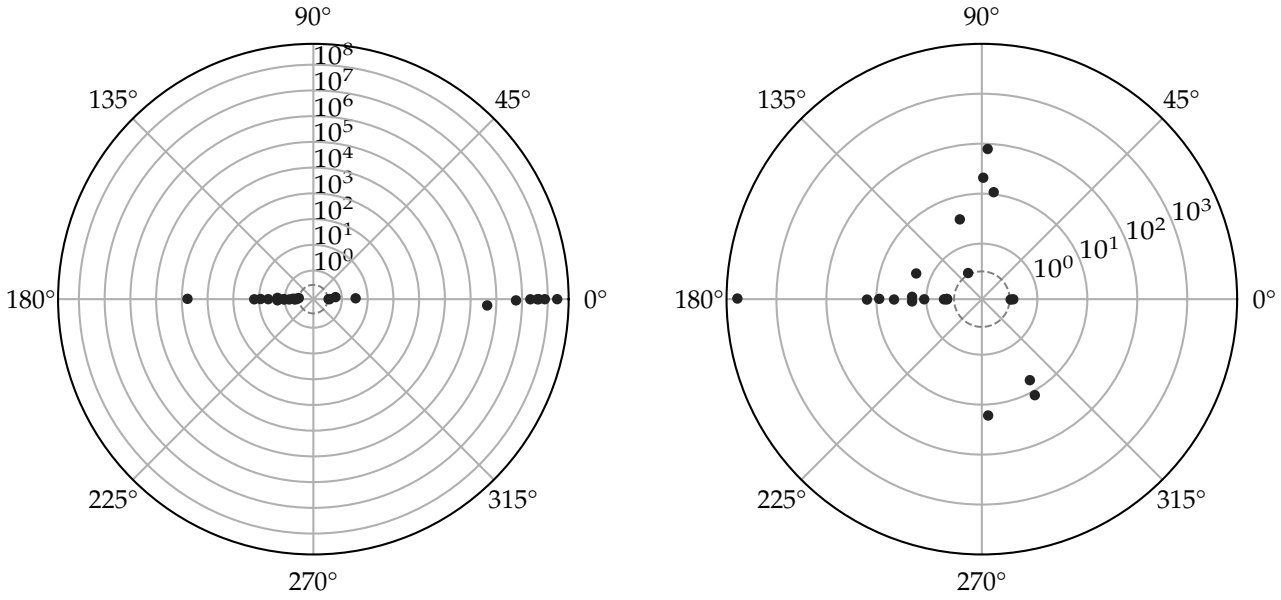

(a) Plasma current response from the pure iMHD model. The largest 27 eigenvalues are shown, 16 of which have a magnitude greater than one.

(b) Plasma current response from the hybrid iMHD/kinetic model. The largest 22 eigenvalues are shown, 15 of which have a magnitude greater than one.

Figure 5.10: Eigenvalues of the iteration operator $\hat{K}$ as discussed in chapter 2 in the complex plane. Note that the radius is plotted logarithmically outside the innermost grid circle, corresponding to a value of one, and linearly inside. A threshold value of $\lambda_{\text{sup}} = 0.5$, indicated by the dashed gray circle, and a tolerance of 10^{-9} (see section 4.6) have been used. The pure iMHD model yields eigenvalues which are clustered around the real line and have higher magnitude than the hybrid iMHD/kinetic model, but the number of relevant eigenvalues is quite similar.

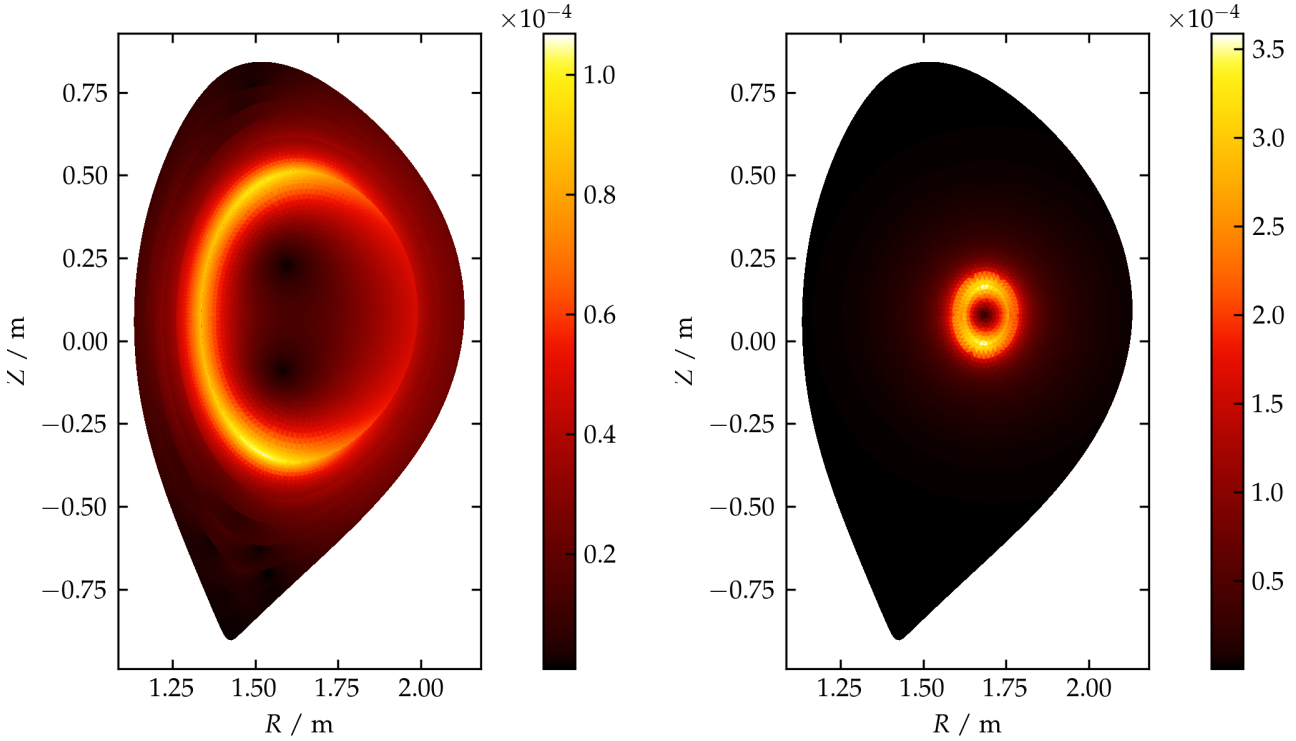

(a) Plasma current response from the pure iMHD model. This eigenvector attains its largest magnitude around the $(m, n) = (-3, 2)$ resonance position.

(b) Plasma current response from the hybrid iMHD/kinetic model. This eigenvector attains its largest magnitude around a flux surface between the $(m, n) = (-3, 2)$ resonance position and the magnetic axis.

Figure 5.11: The magnitude of the eigenvector corresponding to the largest eigenvalue of the iteration operator $\hat{K}$ discussed in chapter 2, interpreted as magnetic field perturbation in arbitrary units. This visualizes the contribution of the magnetic perturbation field which is most strongly amplified by the plasma response.

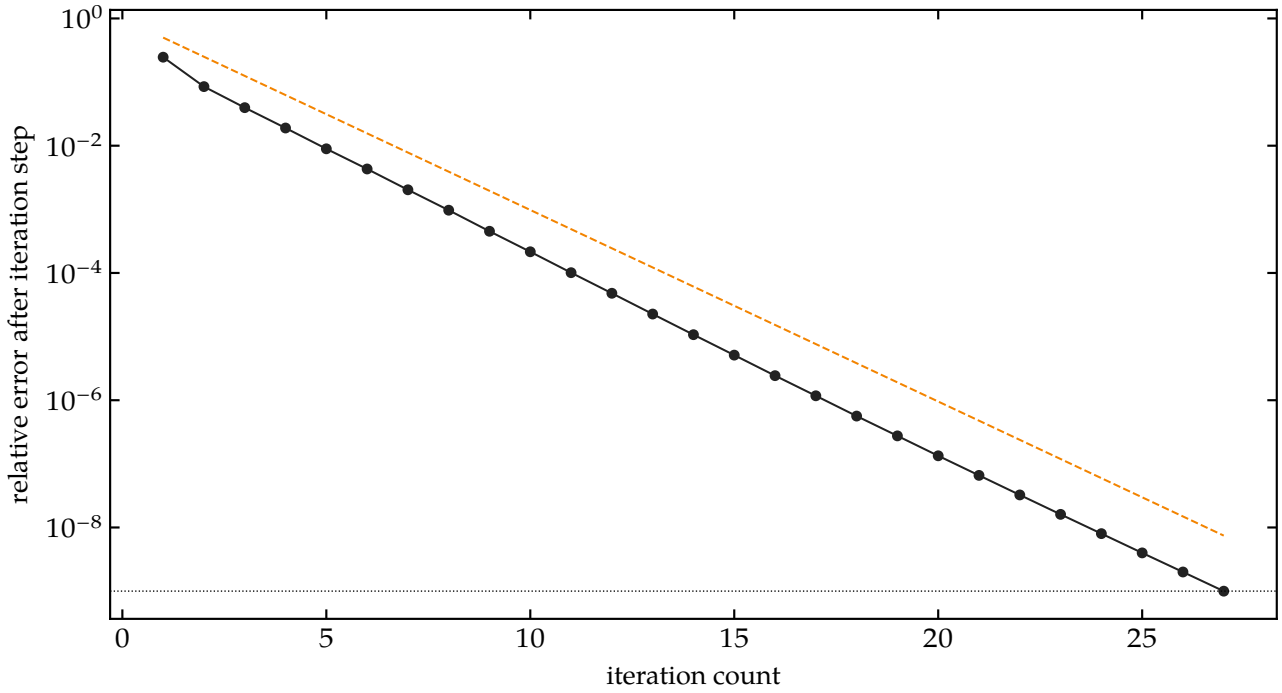

Figure 5.12: Convergence of the preconditioned iterations as discussed in section 4.6, specifically (4.66), for the hybrid iMHD/kinetic model. After 27 iteration steps, a relative error of 9.98×10^{-10} is achieved, which is one iteration step below the requested relative error of 10^{-9} indicated by the dotted horizontal line. The black circles indicate this relative error, i.e., the L^2 norm of the difference to the previous iteration step over the L^2 norm of the vacuum magnetic perturbation. The dashed orange line indicates a convergent major, the geometric series with a factor of $\lambda_{\text{sup}} = 0.5$, which is the supremum of the remaining eigenvalues of the preconditioned iterations discussed in chapter 2.

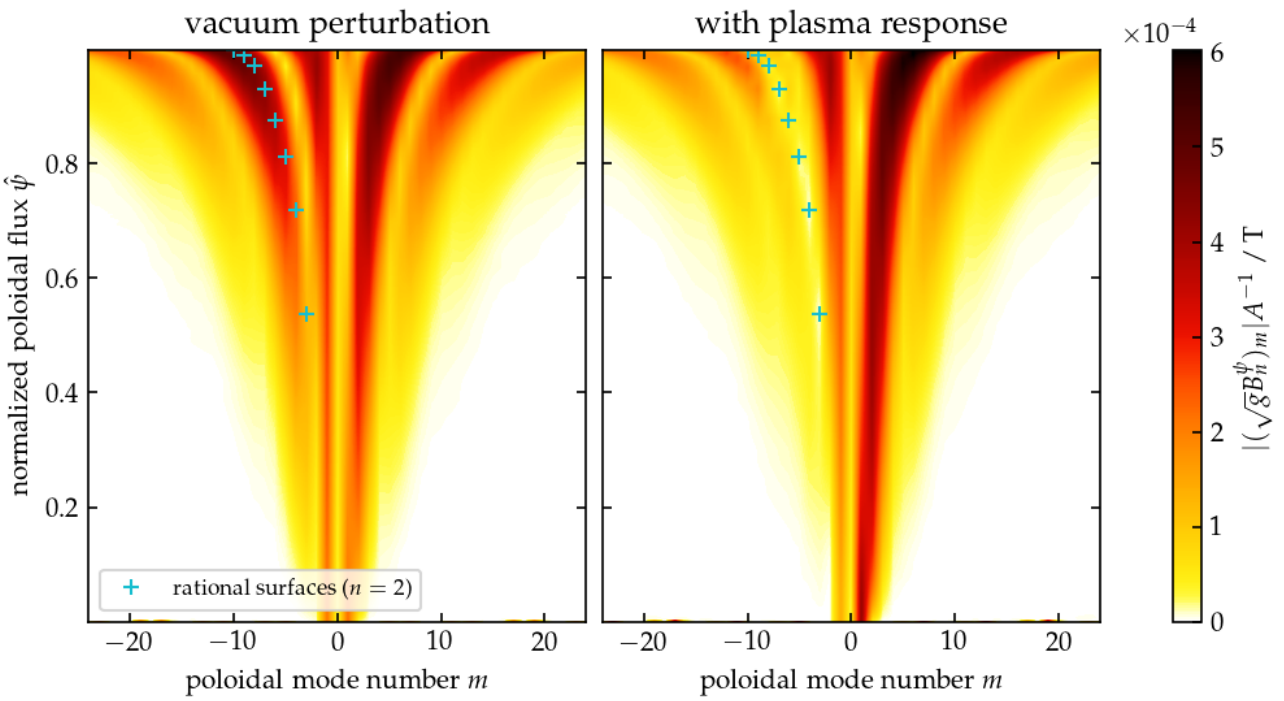

Figure 5.13: Spectrum of the magnetic field perturbation for toroidal mode number $n = 2$. The shielding by the plasma response is apparent near the resonant surfaces indicated by the blue crosses.

5.2.1 Near-Axis Behaviour

We consider the asymptotic behavior near the magnetic axis at (R_O, Z_O) of the radial magnetic field perturbation as given by (4.72), which we fully expand to

$$\frac{\sigma_{\psi'} \mathcal{B}^{\psi}_{mn}}{A} = \frac{\left(\sqrt{g} B^{\psi}_n\right)_m}{\left\langle \sqrt{g} \, |\nabla\psi| \right\rangle} = \frac{\frac{\sigma_{\psi'}}{2\pi} \int_0^{2\pi} \sqrt{g} \boldsymbol{B}_n \cdot \nabla\psi \, \mathrm{e}^{-\mathrm{i}m\theta} \, \mathrm{d}\vartheta}{\int_0^{2\pi} \sqrt{g} \, |\nabla\psi| \, \mathrm{d}\vartheta}. \tag{5.8}$$

We are interested in the leading order of the Taylor series in ψ, so we start with the series expansion of each factor in $x = R - R_O$ and $y = Z - Z_O$, and then take the coordinate transform. For transformation from cylindrical to symmetry flux coordinates, we assume elliptical contours for the flux surfaces

$$\hat{\psi} = \hat{r}^2 = \frac{x^2}{a^2} + \frac{y^2}{b^2}, \tag{5.9}$$

where $\hat{\psi}$ is normalized ψ. Without loss of generality, we continue with $\hat{\psi}$ instead of ψ, as the normalization constant cancels in the numerator and denominator of (5.8) and we can ignore the sign $\sigma_{\psi'}$. Now, using the geometrical poloidal angle θ, the associated coordinate transform is

$$x = a\hat{r} \cos\theta, \qquad y = b\hat{r} \sin\theta. \tag{5.10}$$

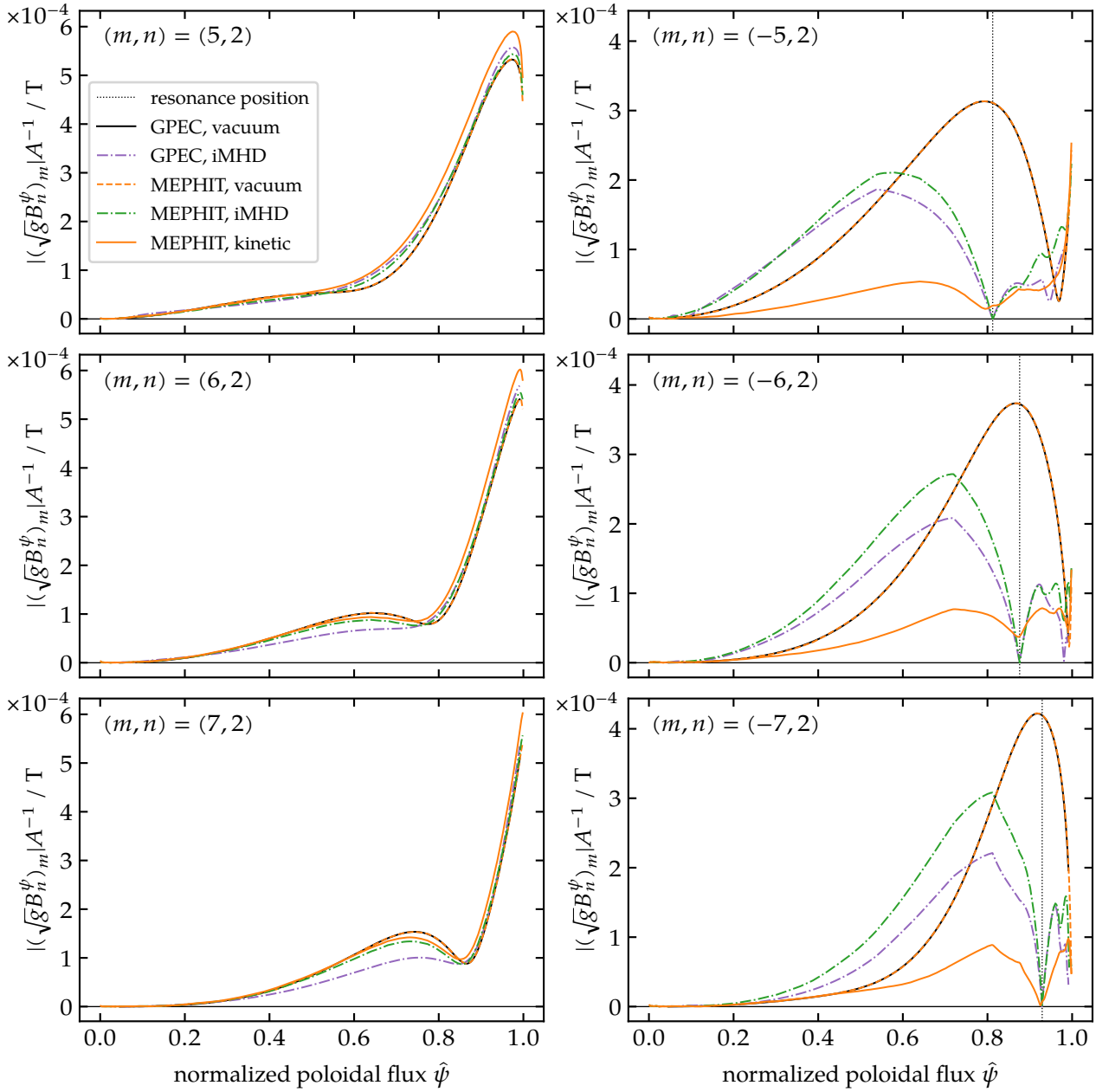

Figure 5.14: Fourier amplitudes of the magnetic perturbation fields resulting from MEPHIT and GPEC for a few selected poloidal/toroidal modes. Note that vacuum perturbations agree up to the line width. While non-resonant poloidal modes are not qualitatively altered in their shape, their resonant counterparts with the same periodicity show significant shielding at the resonance position and field penetration in the interior region. The amplitude is generally reduced in the kinetic vs. the iMHD case, and at least for $m = -5$ and $m = -6$, shielding is also reduced.

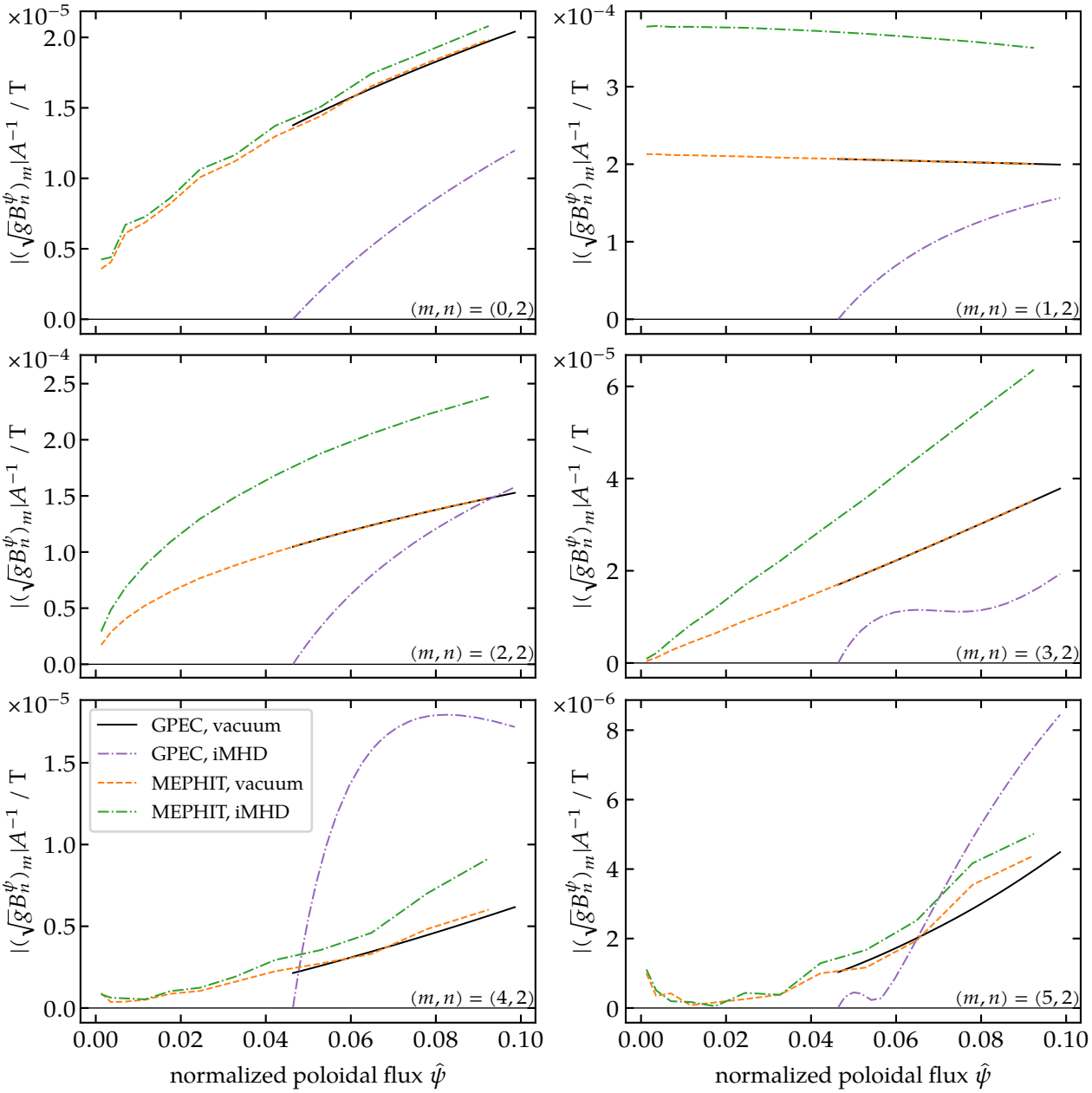

Figure 5.15: Fourier amplitudes of the magnetic perturbation fields resulting from MEPHIT (ideal MHD) and GPEC for a few selected poloidal/toroidal modes, enhanced around the magnetic axis. Due to the low poloidal resolution close to the axis, the results of the Fourier transform in MEPHIT are somewhat imprecise. The leading-order estimate given in table 5.2 still holds, although the application of a numerical derivative is not feasible.

To show that the geometric θ approximates magnetic ϑ well near the axis, we consider the Jacobian of symmetry flux coordinates,

$$\sqrt{g} = C(\hat{\psi})R^2, \tag{5.11}$$

with some flux function $C(\hat{\psi})$ that accounts for the flux functions in (1.7) and the normalization of ψ, and compare it to the progression of coordinate transforms from Cartesian to symmetry flux coordinates,

$$\begin{aligned}\sqrt{g} &= \frac{\partial(X,Y,Z)}{\partial(\hat{\psi},\varphi,\vartheta)} = \frac{\partial(X,Y,Z)}{\partial(R,\varphi,Z)}\frac{\partial(R,Z)}{\partial(\hat{\psi},\vartheta)} = R\frac{\partial(x,y)}{\partial(\hat{\psi},\vartheta)} = R\frac{\partial(x,y)}{\partial(\hat{r},\theta)}\frac{\partial(\hat{r},\theta)}{\partial(\hat{\psi},\vartheta)} \\ &= Ra^2b^2\hat{r}\frac{\partial(\hat{r},\theta)}{\partial(\hat{\psi},\vartheta)} = Ra^2b^2\cancel{\hat{r}}\frac{1}{2\cancel{\hat{r}}}\frac{\partial\theta}{\partial\vartheta}.\end{aligned} \tag{5.12}$$

Comparison of (5.11) and (5.12) yields

$$\frac{\partial\theta}{\partial\vartheta} = \frac{2C(\hat{\psi})}{a^2b^2}R. \tag{5.13}$$

With $R \approx R_\mathrm{O}$ near the axis, this factor is constant. This means it is necessarily equal to 1, and geometric θ and magnetic ϑ are equal (up to a constant offset) in this approximation.

Expanding (5.11) in x and transforming to $(\hat{r},\theta)$ yields

$$\begin{aligned}\sqrt{g} &= C(\hat{\psi})\left(x^2 + 2R_\mathrm{O}x + R_\mathrm{O}^2\right) = C(\hat{\psi})\left(a^2\hat{r}^2(\cos\theta)^2 + 2R_\mathrm{O}a\hat{r}\cos\theta + R_\mathrm{O}^2\right) \\ &= C(\hat{\psi})\sum_{j=0}^{2} c_j\hat{r}^j(\cos\theta)^j\end{aligned} \tag{5.14}$$

with factors

$$c_0 = R_\mathrm{O}^2, \qquad c_1 = 2R_\mathrm{O}a, \qquad c_2 = a^2. \tag{5.15}$$

The flux surface average is given by

$$A = \left\langle\sqrt{g}\,|\nabla\psi|\right\rangle = 2C(\hat{\psi})\int_0^{2\pi}\left(x^2 + R_\mathrm{O}x + 2R_\mathrm{O}^2\right)\sqrt{\frac{x^2}{a^4} + \frac{y^2}{b^4}}\,\mathrm{d}\theta \tag{5.16}$$

$$= 4C(\hat{\psi})\frac{\hat{r}}{a}\sum_{j=0}^{2} c_j\hat{r}^j\int_0^{2\pi}(\cos\theta)^j\sqrt{1 - \left(1 - \frac{a^2}{b^2}\right)(\sin\theta)^2}\,\mathrm{d}\theta \tag{5.17}$$

$$= C(\hat{\psi})(C_0\hat{r} + C_2\hat{r}^3). \tag{5.18}$$

The remaining coefficients are given in terms of complete elliptic integrals of the first and

second kind, although we are mostly interested in the order of magnitude:

$$C_0 = 16\frac{a}{b}E\left(1-\tfrac{b^2}{a^2}\right)\frac{R_\mathrm{O}^2}{a} \leq 8\pi\frac{R_\mathrm{O}^2}{a}, \tag{5.19}$$

$$C_2 = \frac{8}{3b}\left(\frac{a}{b}\frac{1}{1-\frac{a^2}{b^2}}\left(aK\left(1-\tfrac{a^2}{b^2}\right)+bK\left(1-\tfrac{b^2}{a^2}\right)\right)-\right.$$
$$\left.-\left(1+\frac{1}{1-\frac{a^2}{b^2}}\right)\left(aE\left(1-\tfrac{b^2}{a^2}\right)+bE\left(1-\tfrac{a^2}{b^2}\right)\right)\right)a \leq 4\pi a, \tag{5.20}$$

$$\frac{C_2}{C_0} \sim \frac{a^2}{R_\mathrm{O}^2}. \tag{5.21}$$

For our estimation, we expand the reciprocal in $\hat{r}$,

$$\frac{1}{A} = \frac{1}{\left\langle\sqrt{g}\,|\nabla\psi|\right\rangle} = \frac{1}{C(\hat{\psi})}\frac{\hat{r}^{-1}}{C_0}\left(1-\frac{C_2}{C_0}\hat{r}^2+\frac{C_2^2}{C_0^2}\hat{r}^4-\cdots\right), \tag{5.22}$$

and keep only the leading order, as successive coefficients fall off rapidly.

Finally, we expand the Taylor series of the toroidal Fourier amplitudes of the cylindrical components of $\boldsymbol{B}_n$:

$$B_n^R = \sum_{m_1=0}^{\infty}\sum_{m_2=0}^{\infty}\frac{x^{m_1}y^{m_2}}{m_1!m_2!}\frac{\partial^{m_1+m_2}}{\partial R^{m_1}\,\partial Z^{m_2}}B_n^R(R_\mathrm{O},Z_\mathrm{O}), \tag{5.23}$$

$$B_n^Z = \sum_{m_1=0}^{\infty}\sum_{m_2=0}^{\infty}\frac{x^{m_1}y^{m_2}}{m_1!m_2!}\frac{\partial^{m_1+m_2}}{\partial R^{m_1}\,\partial Z^{m_2}}B_n^Z(R_\mathrm{O},Z_\mathrm{O}). \tag{5.24}$$

Taking the projection $\boldsymbol{B}_n\cdot\nabla\hat{\psi}$ and transforming from (x,y) to $(\hat{r},\theta)$ yields

$$\begin{aligned}B_n^{\hat{\psi}} &= 2\sum_{m_1=0}^{\infty}\sum_{m_2=0}^{\infty}\frac{x^{m_1}y^{m_2}}{m_1!m_2!}\left(\frac{x}{a^2}\frac{\partial^{m_1+m_2}}{\partial R^{m_1}\,\partial Z^{m_2}}B_n^R(R_\mathrm{O},Z_\mathrm{O})+\frac{y}{b^2}\frac{\partial^{m_1+m_2}}{\partial R^{m_1}\,\partial Z^{m_2}}B_n^Z(R_\mathrm{O},Z_\mathrm{O})\right)\\ &= 2\sum_{m_1=0}^{\infty}\sum_{m_2=0}^{\infty}\frac{\hat{r}^{m_1+m_2+1}(a\cos\theta)^{m_1}(b\sin\theta)^{m_2}}{m_1!m_2!}\left(\frac{\cos\theta}{a}\frac{\partial^{m_1+m_2}}{\partial R^{m_1}\,\partial Z^{m_2}}B_n^R(R_\mathrm{O},Z_\mathrm{O})+\right.\\ &\qquad\left.+\frac{\sin\theta}{b}\frac{\partial^{m_1+m_2}}{\partial R^{m_1}\,\partial Z^{m_2}}B_n^Z(R_\mathrm{O},Z_\mathrm{O})\right).\end{aligned} \tag{5.25}$$

For brevity, we collect factors independent of $\hat{r}$ and θ,

$$\beta_{m_1,m_2}^R = \frac{2}{a}\frac{a^{m_1}b^{m_2}}{m_1!m_2!}\frac{\partial^{m_1+m_2}}{\partial R^{m_1}\,\partial Z^{m_2}}B_n^R(R_\mathrm{O},Z_\mathrm{O}), \tag{5.26}$$

$$\beta_{m_1,m_2}^Z = \frac{2}{b}\frac{a^{m_1}b^{m_2}}{m_1!m_2!}\frac{\partial^{m_1+m_2}}{\partial R^{m_1}\,\partial Z^{m_2}}B_n^Z(R_\mathrm{O},Z_\mathrm{O}). \tag{5.27}$$

Furthermore, we introduce a new summation index $m_0 = m_1 + m_2$ instead of m_2, which

allows grouping by the largest exponent:

$$\begin{aligned} B_n^{\hat{\psi}} &= \sum_{m_1=0}^{\infty} \sum_{m_2=0}^{\infty} \hat{r}^{m_1+m_2+1} (\cos\theta)^{m_1} (\sin\theta)^{m_2} \left(\beta^R_{m_1,m_2} \cos\theta + \beta^Z_{m_1,m_2} \sin\theta \right) \\ &= \sum_{m_0=0}^{\infty} \hat{r}^{m_0+1} \sum_{m_1=0}^{m_0} (\cos\theta)^{m_1} (\sin\theta)^{m_0-m_1} \left(\beta^R_{m_1,m_0-m_1} \cos\theta + \beta^Z_{m_1,m_0-m_1} \sin\theta \right). \end{aligned} \tag{5.28}$$

Before considering the Fourier transform in θ, we include $\sqrt{g}$ from (5.14),

$$\begin{aligned} \sqrt{g} B_n^{\hat{\psi}} = C(\hat{\psi}) \sum_{j=0}^{2} c_j \sum_{m_0=0}^{\infty} \hat{r}^{m_0+1+j} \sum_{m_1=0}^{m_0} (\cos\theta)^{m_1+j} (\sin\theta)^{m_0-m_1} \Big(\beta^R_{m_1,m_0-m_1} \cos\theta + \\ + \beta^Z_{m_1,m_0-m_1} \sin\theta \Big). \end{aligned} \tag{5.29}$$

Anticipating the Fourier transform, we use complex forms for sine and cosine. For a given exponent K, we see that exponents of $\exp \mathrm{i}\theta$ range from $-K$ to K. Again, we are not interested in constant coefficients, and just abbreviate them without explicit transformation:

$$(\cos\theta)^K = \sum_{k=0}^{K} \frac{1}{2^K} \binom{K}{k} \mathrm{e}^{\mathrm{i}(K-2k)\theta} = \sum_{k=-K}^{K} \sigma_k \mathrm{e}^{\mathrm{i}k\theta}, \tag{5.30}$$

$$(\sin\theta)^K = \sum_{k=0}^{K} \frac{(-1)^k}{2^K \mathrm{i}^K} \binom{K}{k} \mathrm{e}^{\mathrm{i}(K-2k)\theta} = \sum_{k=-K}^{K} \eta_k \mathrm{e}^{\mathrm{i}k\theta}. \tag{5.31}$$

The combined maximum exponent in (5.29) is $K = \cancel{m_1} + j + m_0 - \cancel{m_1} + 1$, yielding

$$\sqrt{g} B_n^{\hat{\psi}} = C(\hat{\psi}) \sum_{j=0}^{2} c_j \sum_{m_0=0}^{\infty} \hat{r}^{m_0+1+j} \sum_{k=-m_0-1-j}^{m_0+1+j} \alpha_{m_0,k} \mathrm{e}^{\mathrm{i}k\theta} \tag{5.32}$$

with some constant coefficients $\alpha_{m_0,k}$. The Fourier transform is then simply

$$\mathcal{B}^{\hat{\psi}}_{mn} = \left(\sqrt{g} B_n^{\hat{\psi}} \right)_m = \frac{1}{2\pi} \int_0^{2\pi} \sqrt{g} B_n^{\hat{\psi}} \mathrm{e}^{-\mathrm{i}m\theta} \,\mathrm{d}\theta = \frac{C(\hat{\psi})}{2\pi} \sum_{j=0}^{2} c_j \sum_{m_0=0}^{\infty} \hat{r}^{m_0+1+j} \sum_{k=-m_0-1-j}^{m_0+1+j} \alpha_{m_0,k} \int_0^{2\pi} \mathrm{e}^{\mathrm{i}(k-m)\theta} \,\mathrm{d}\theta. \tag{5.33}$$

We include the normalization from (5.22), cancel $C(\hat{\psi})$, and absorb the remaining constants into c_j, i.e., $c_j \to c_j / 2\pi C_0$, effectively reducing the order of $\hat{r}$ by 1. The integral reduces to a Kronecker delta and we finally have

$$\frac{\mathcal{B}^{\hat{\psi}}_{mn}}{A} = \sum_{j=0}^{2} c_j \sum_{m_0=0}^{\infty} \hat{r}^{m_0+j} \sum_{k=-m_0-1-j}^{m_0+1+j} \alpha_{m_0,k} \delta_{k,m} = \sum_{j=0}^{2} \sum_{m_0=0}^{\infty} c_j \alpha_{m_0,m} \hat{r}^{m_0+j} \left[\!\left[m_0 + 1 + j \geq |m| \right]\!\right]. \tag{5.34}$$

In the last step, we used the Iverson bracket[1] to reduce the innermost summation. It can be interpreted as imposing a lower bound on m_0 depending on j and $|m|$. We are interested in the leading orders in $\hat{r}$, so we carry out the summations for the first few terms and group the results accordingly, yielding table 5.1.

Table 5.1: Taylor series expansion of the radial magnetic field perturbation $\mathcal{B}^{\hat{\psi}}_{mn}A^{-1}$, depending on poloidal mode number m according to (5.34). The schematic continues regularly for $|m| > 2$.

$\lvert m\rvert$	$\mathcal{B}^{\hat{\psi}}_{mn}A^{-1}$ grouped by m_0	$\mathcal{B}^{\hat{\psi}}_{mn}A^{-1}$ grouped by $m_0 + j$
0	$\alpha_{0,m}(c_2\hat{r}^2 + c_1\hat{r}^1 + c_0\hat{r}^0) +$ $\alpha_{1,m}(c_2\hat{r}^3 + c_1\hat{r}^2 + c_0\hat{r}^1) + \cdots$	$\hat{r}^0\ c_0\alpha_{0,m} +$ $\hat{r}^1(c_0\alpha_{1,m} + c_1\alpha_{0,m}) + \cdots$
1	$\alpha_{0,m}(c_2\hat{r}^2 + c_1\hat{r}^1 + c_0\hat{r}^0) +$ $\alpha_{1,m}(c_2\hat{r}^3 + c_1\hat{r}^2 + c_0\hat{r}^1) + \cdots$	$\hat{r}^0\ c_0\alpha_{0,m} +$ $\hat{r}^1(c_0\alpha_{1,m} + c_1\alpha_{0,m}) + \cdots$
2	$\alpha_{0,m}(c_2\hat{r}^2 + c_1\hat{r}^1) +$ $\alpha_{1,m}(c_2\hat{r}^3 + c_1\hat{r}^2 + c_0\hat{r}^1) +$ $\alpha_{2,m}(c_2\hat{r}^4 + c_1\hat{r}^3 + c_0\hat{r}^2) + \cdots$	$\hat{r}^1(c_0\alpha_{1,m} + c_1\alpha_{0,m}) +$ $\hat{r}^2(c_0\alpha_{2,m} + c_1\alpha_{1,m} + c_2\alpha_{0,m}) +$ $\hat{r}^3(c_0\alpha_{3,m} + c_1\alpha_{2,m} + c_0\alpha_{1,m}) + \cdots$
3	$\alpha_{0,m}\ c_2\hat{r}^2 +$ $\alpha_{1,m}(c_2\hat{r}^3 + c_1\hat{r}^2) +$ $\alpha_{2,m}(c_2\hat{r}^4 + c_1\hat{r}^3 + c_0\hat{r}^2) + \cdots$	$\hat{r}^2(c_0\alpha_{2,m} + c_1\alpha_{1,m} + c_2\alpha_{0,m}) +$ $\hat{r}^3(c_0\alpha_{3,m} + c_1\alpha_{2,m} + c_2\alpha_{1,m}) +$ $\hat{r}^4(c_0\alpha_{4,m} + c_1\alpha_{3,m} + c_2\alpha_{2,m}) + \cdots$
4	$\alpha_{1,m}\ c_2\hat{r}^3 +$ $\alpha_{2,m}(c_2\hat{r}^4 + c_1\hat{r}^3) +$ $\alpha_{3,m}(c_2\hat{r}^5 + c_1\hat{r}^4 + c_0\hat{r}^3) + \cdots$	$\hat{r}^3(c_0\alpha_{3,m} + c_1\alpha_{2,m} + c_2\alpha_{1,m}) +$ $\hat{r}^4(c_0\alpha_{4,m} + c_1\alpha_{3,m} + c_2\alpha_{2,m}) +$ $\hat{r}^5(c_0\alpha_{5,m} + c_1\alpha_{4,m} + c_2\alpha_{3,m}) + \cdots$

Judging from table 5.1, the leading order for $m = 0$ should be $\hat{\psi}^0$, but in figure 5.15, it appears to be $\hat{\psi}^{\frac{1}{2}}$ instead, implying $\alpha_{0,0} = 0$. This can be explained by revisiting (5.29) and the transformation following it. The exponents of $\exp \mathrm{i}\theta$ are actually all *even* for *even* K and all *odd* for *odd* K. The case distinction is cumbersome for the general derivation, but consider the coefficients of $\hat{r}^0$ in the case $m = 0$. It only has contributions from $m_0 = 0$ and $j = 0$, meaning $K = m_0 + j + 1 = 1$. Thus $k = \pm 1$, which does not contribute to the $m = 0$ mode; however, it contributes to the $m = \pm 1$ modes, which show the expected behavior. All other coefficients of $\hat{r}^{K-1}$ for all m have at least one even and odd non-zero contribution, so we have the only exception covered. We arrive at the *leading order* in $\hat{\psi}$ for $\mathcal{B}^{\hat{\psi}}_{mn}A^{-1}$ and its derivative near the magnetic axis given in table 5.2.

Comparing the full perturbation including plasma response and the vacuum perturbation between GPEC and MEPHIT, we notice a few peculiarities. The predicted behavior is followed by the vacuum perturbations of both MEPHIT and GPEC, as well as the full perturbation of MEPHIT (up to the availabe precision), but not by the full perturbation of GPEC, except possibly for $m = 0, \pm 2$. The derivation depends only on geometrical considerations, so the

[1] yields 1 if its argument is true an 0 otherwise

Table 5.2: Leading order of radial coordinate $\hat{\psi}$ in Taylor series expansion of the radial magnetic field perturbation $\mathcal{B}^{\hat{\psi}}_{mn}A^{-1}$ and its radial derivative in table 5.1, depending on poloidal mode number m.

$\lvert m\rvert$	$\mathcal{B}^{\hat{\psi}}_{mn}A^{-1}$	$\partial_{\hat{\psi}}\left(\mathcal{B}^{\hat{\psi}}_{mn}A^{-1}\right)$
0	$\hat{\psi}^{\frac{1}{2}}$	$\hat{\psi}^{-\frac{1}{2}}$
1	$\hat{\psi}^{0}$	$\hat{\psi}^{-\frac{1}{2}}$
2	$\hat{\psi}^{\frac{1}{2}}$	$\hat{\psi}^{-\frac{1}{2}}$
3	$\hat{\psi}^{1}$	$\hat{\psi}^{0}$
4	$\hat{\psi}^{\frac{3}{2}}$	$\hat{\psi}^{\frac{1}{2}}$
5	$\hat{\psi}^{2}$	$\hat{\psi}^{1}$

result of any Fourier transform as derived should result in the expected behaviour; however, GPEC operates directly on the poloidal modes. In private corresespondence, Park and Logan [25] acknowledged this discrepancy, but they point out that "incorrect asymptotics do not impact bulk response benchmarks with other established codes [31, 32]". The underlying code DCON exhibits a singular point at the axis, which explains the lower bound $\hat{\psi} \approx 0.05$ of the curves for GPEC in figure 5.15.

5.2.2 Isotope Effects

The results presented in this section have already been submitted for publication [4].

To characterize the plasma response current from the kinetic model presented in chapter 3, we perform a sweep over the $E \times B$ velocity by adding an appropriate offset to E_{0r}, once for a pure deuterium plasma and once for a pure hydrogen plasma. $(B^r_1/B^\varphi_0)_{\boldsymbol{m}}$ is set constant and the parallel current density perturbation resulting from (3.120) is then integrated in analogy to (15) of [13],

$$I_{\parallel \boldsymbol{m}} = 2\pi \int_{r_{\boldsymbol{m}}-\Delta r}^{r_{\boldsymbol{m}}-\Delta r} \mathrm{d}r \left(\frac{\sqrt{g}J_\parallel}{R}\right)_{\boldsymbol{m}}, \tag{5.35}$$

where Δr was set to the width $\delta_{\boldsymbol{m}}$ of the resonant layer. The results for this parallel response current for two Fourier modes of interest are shown in figure 5.16.

For the same modes, we run the full iterative scheme twice with different offsets for E_{0r}, once "on" and once "off" the electron fluid resonance seen in the sweep, again for a pure deuterium and a pure hydrogen plasma. Since the difference between the isotopes would be harly visible in figure 5.14, figure 5.17 provides an enlarged version, showing the effect of isotope discrimination in the kinetic approximation.

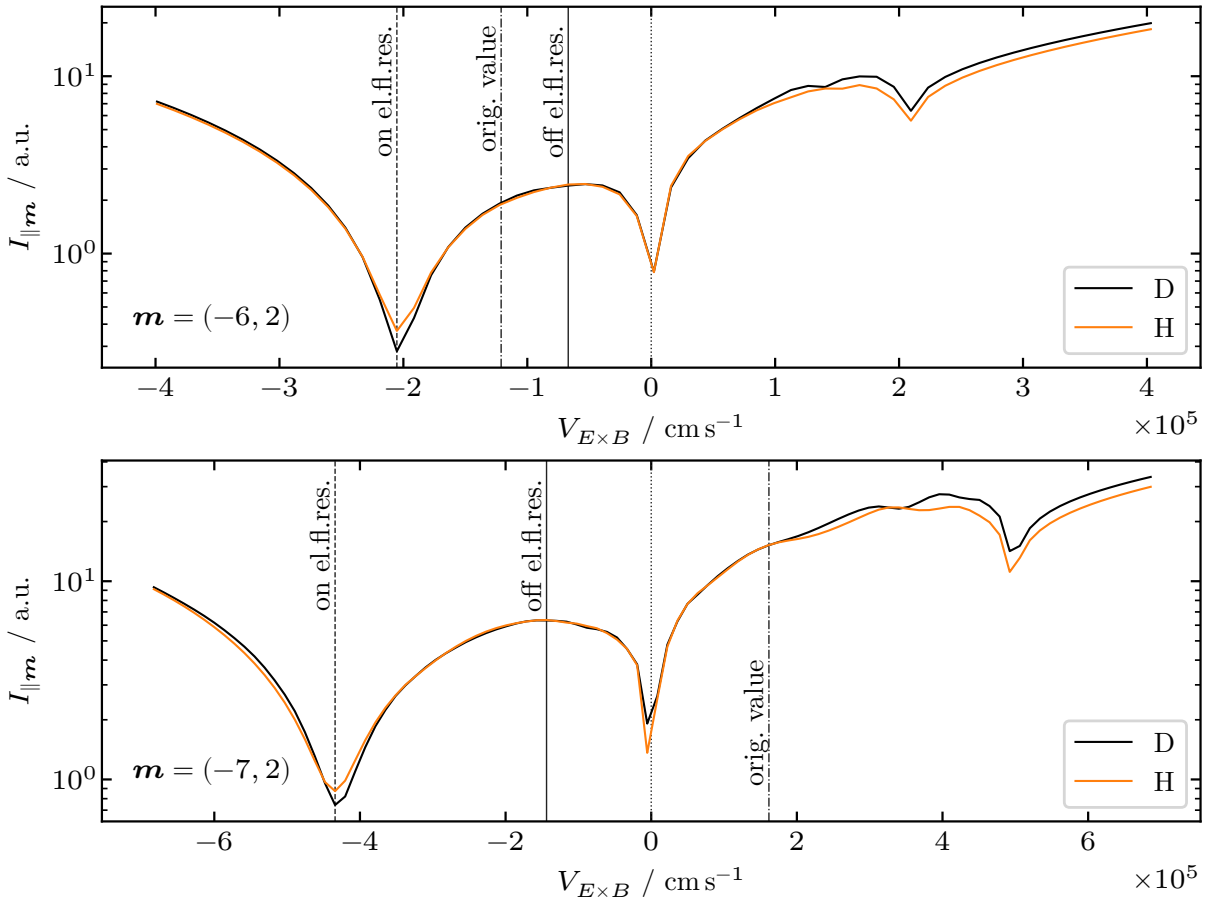

Figure 5.16: Parallel response current within the resonant layer as a function of $E \times B$ velocity at constant magnetic field perturbation for deuterium and hydrogen. The dotted vertical line indicates the electrical or gyrocenter resonance at $V_{E\times B} = 0$. The electron fluid resonance at negative velocities yields the lowest parallel response current, as is expected. A tentative ion fluid resonance occurs at positive velocities. The dashed and solid vertical lines indicate the velocities chosen for a full iterative solution "on" and "off" the electron fluid resonance in figure 5.17. The dash-dotted vertical line indicates the original value, i.e., without the offset for the sweep.

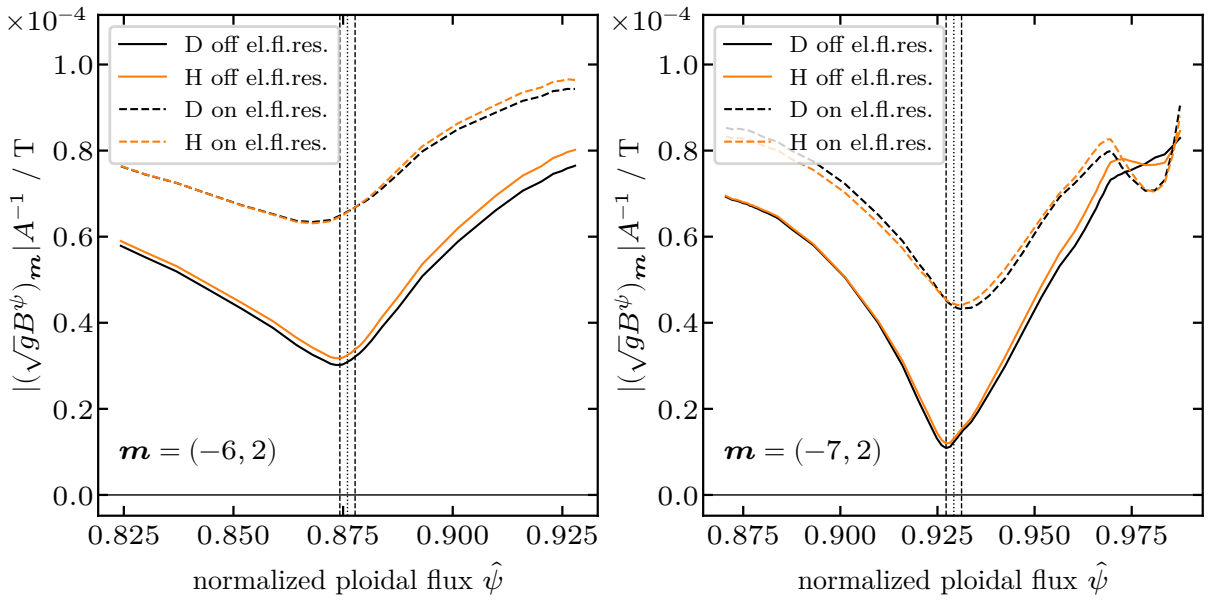

Figure 5.17: Fourier amplitude of the radial magnetic field perturbation, the same quantity as in figure 5.14, but enlarged around the resonance position indicated by the dotted vertical line. The dashed vertical line indicates twice the resonant layer width $\delta_{\boldsymbol{m}}$. Shielding is slightly lower for hydrogen than for deuterium in the kinetic approximation, at least off the electron fluid resonance.

Despite a very similar radial perturbation magnetic field, the parallel misalignment electrostatic field is rather different for the hydrogen and deuterium ions. This field is shown in figure 5.18 together with the respective parallel plasma response current densities. The latter are very similar (which explains similar RMP shielding) since these densities are mainly produced by the electrons in a narrow region around the resonant flux surface where the contribution of the electrostatic potential perturbation to the misalignment field is much smaller than the contribution of the axisymmetric electric field via the corrugation of magnetic flux surfaces. In contrast to the electrons, the region where ions interact with RMPs via Landau damping is much wider than the region of electron interaction. Although the ion contribution to the parallel shielding current is small, their resonant interaction with RMPs leads to quasilinear toroidal torque which is not necessarily small compared to the electron torque.

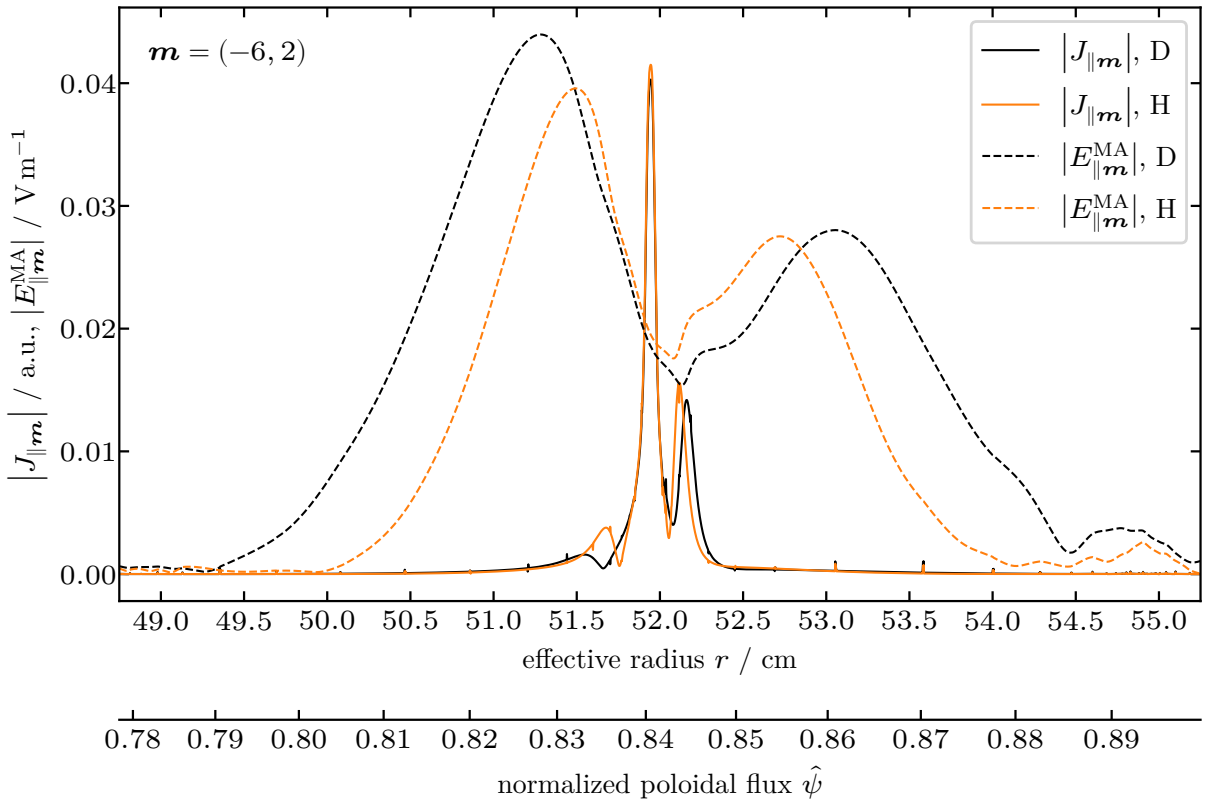

Figure 5.18: Parallel misalignment field and parallel response current density for deuterium (black) and hydrogen (orange) ions for mode $\boldsymbol{m} = (-6, 2)$ off the electron fluid resonance as indicated in figure 5.16.

Chapter 6

Conclusion and Outlook

In this work, an ideal MHD model of resonant magnetic perturbations (RMPs) in realistic tokamak geometry has been derived from first principles and implemented as the code MEPHIT. The previously established iteration scheme with a custom preconditioner [7] is demonstrated to be compatible with this model. As part of each iteration step, Ampère's equation is solved with a finite element method. To this end, we developed a general formalism to apply a Fourier series expansion along a symmetry direction in the context of the Galerkin method, which is validated against established model problems [1]. The simulation results for the ASDEX Upgrade tokamak have been benchmarked against the established ideal MHD code GPEC [33], showing at least qualitative agreement. An analytical derivation of the near-axis behaviour further supports the results obtained via MEPHIT. Moreover, the ideal MHD model has been combined with a kinetic model of the plasma response current in the region surrounding rational surfaces, a novel approach which is also shown to be compatible with the iterative scheme. It has been derived in the straight-cylinder limit, which is then extended to toroidal geometry. Inclusion of the second-order contribution of finite Larmor radius expansion allows discrimination between hydrogen isotopes in principle, although the influence of ions on shielding of RMPs is rather small. Despite the very similar radial perturbation magnetic field, the parallel misalignment electrostatic field is rather different for the hydrogen and deuterium ions, which in turn affects quasi-linear effects such as toroidal torque from RMPs. Further investigation is warranted to explain the experimentally observed differences [34], likely necessitating a kinetic integral model, but this endeavour is beyond the scope of this thesis.

The presented model is quite extensible, and an interface to the fully three-dimensional drift-kinetic code Gorilla [16] is planned. The latter also extends its mesh to the scrape-off layer and the private flux region, which we expect to be applicable also to MEPHIT, given that it operates on cylindrical coordinates which do not exhibit singularities within the computational domain. Further benchmarking of the existing model is currently underway, specifically with the code MARS [35, 36] and for the MAST Upgrade tokamak. On a more technical note, there is still room for improvement in the implementation of MEPHIT. Higher-order finite elements, XFEM to handle the singularities in the ideal MHD model, and adaptive mesh refinement come to mind. Parallelization would further improve performance, making the running time comparable to GPEC [33].

Bibliography

[1] Christopher G. Albert, Patrick Lainer, and Oszkár Bíró. "2D Fourier finite element formulation for magnetostatics in curvilinear coordinates with a symmetry direction." In: *Computer Physics Communications* 277 (2022), p. 108401. ISSN: 0010-4655. DOI: 10.1016/j.cpc.2022.108401.

[2] P Lainer, S V Kasilov, W Kernbichler, M Reichelt, and C G Albert. "Iterative approach to linear ideal MHD modeling of plasma response to 3D magnetic perturbations in tokamaks." In: *Journal of Physics: Conference Series* 2397.1 (Dec. 2022), p. 012014. DOI: 10.1088/1742-6596/2397/1/012014.

[3] Patrick Lainer, Jonatan Schatzlmayr, Christopher G. Albert, Martin Heyn, Sergiy Kasilov, Winfried Kernbichler, and Markus Markl. "Towards iterative 2D and 3D kinetic modelling of RMP interaction with tokamak plasmas." In: *49th EPS Conference on Plasma Physics*. 2023.

[4] P. Lainer, M. Markl, M. F. Heyn, S. V. Kasilov, J. Schatzlmayr, C. G. Albert, W. Suttrop, the ASDEX Upgrade Team, and the EUROfusion Tokamak Exploitation Team. "Hybrid kinetic-MHD model of RMP interaction with tokamak plasmas." In: *Journal of Physics: Conference Series* (Aug. 2024). Submitted.

[5] W. D. D'haeseleer, W. N. G. Hitchon, J. D. Callen, and J. L. Shohet. *Flux Coordinates and Magnetic Field Structure. A Guide to a Fundamental Tool of Plasma Theory*. Springer Series in Computational Physics. Springer-Verlag, 1991.

[6] R.C. Grimm, R.L Dewar, and J. Manickam. "Ideal MHD stability calculations in axisymmetric toroidal coordinate systems." In: *Journal of Computational Physics* 49.1 (1983), pp. 94–117. ISSN: 0021-9991. DOI: 10.1016/0021-9991(83)90116-X.

[7] C G Albert, M F Heyn, S V Kasilov, W Kernbichler, A F Martitsch, and A M Runov. "Kinetic modeling of 3D equilibria in a tokamak." In: *Journal of Physics: Conference Series* 775 (Nov. 2016), p. 012001. DOI: 10.1088/1742-6596/775/1/012001.

[8] Gabriel Weinreich. *Geometrical vectors*. Univ. Chicago Press, 1998.

[9] Franco Brezzi and Michel Fortin. *Mixed and hybrid finite element methods*. Vol. 15. Springer Science & Business Media, 2012.

[10] Edoardo Zoni and Yaman Güçlü. "Solving hyperbolic-elliptic problems on singular mapped disk-like domains with the method of characteristics and spline finite elements." In: *J. Comput. Physics* 398 (2019), p. 108889. ISSN: 00219991. DOI: 10.1016/j.jcp.2019.108889.

[11] Michael Reichelt. "Numerical Analysis of 3D Perturbations in Tokamak Plasmas." Master's thesis. Graz University of Technology, 2023.

[12] Michael Reichelt. "Least Squares Galerkin Formulation for Magnetic Differential Equations." Conference talk at Numerical Methods for the Kinetic Equations of Plasma Physics 2023 (NumKin 2023). Garching, Germany, Nov. 6, 2023.

[13] Markus Markl et al. "Kinetic study of the bifurcation of resonant magnetic perturbations for edge localized mode suppression in ASDEX Upgrade." In: *Nuclear Fusion* 63.12 (Sept. 2023), p. 126007. DOI: 10.1088/1741-4326/acf20c.

[14] Martin F. Heyn, Ivan B. Ivanov, Sergei V. Kasilov, Winfried Kernbichler, Peter Leitner, Viktor V. Nemov, Wolfgang Suttrop, and the ASDEX Upgrade Team. "Quasilinear modelling of RMP interaction with a tokamak plasma: application to ASDEX Upgrade ELM mitigation experiments." In: *Nuclear Fusion* 54.6 (May 2014), p. 064005. DOI: 10.1088/0029-5515/54/6/064005.

[15] Lao. *G EQDSK FORMAT*. Feb. 1997. URL: https://w3.pppl.gov/ntcc/TORAY/G_EQDSK.pdf.

[16] M. Eder, C. G. Albert, L. M. P. Bauer, S. V. Kasilov, and W. Kernbichler. "Quasi-geometric integration of guiding-center orbits in piecewise linear toroidal fields." In: *Physics of Plasmas* 27.12 (2020), p. 122508. DOI: 10.1063/5.0022117.

[17] James D. Hanson and Steven P. Hirshman. "Compact expressions for the Biot–Savart fields of a filamentary segment." In: *Physics of Plasmas* 9.10 (Oct. 2002), pp. 4410–4412. ISSN: 1070-664X. DOI: 10.1063/1.1507589.

[18] Patrick Lainer. "Numerical Treatment of Linearly Perturbed Ideal Magnetohydrodynamic Equilibria in a Tokamak." Master's thesis. Graz University of Technology, 2019.

[19] F. Hecht. "New development in FreeFem++." In: *J. Numer. Math.* 20.3-4 (2012), pp. 251–265. ISSN: 1570-2820. URL: https://freefem.org/.

[20] G. R. Cowper. "Gaussian quadrature formulas for triangles." In: *International Journal for Numerical Methods in Engineering* 7.3 (1973), pp. 405–408. DOI: 10.1002/nme.1620070316.

[21] Jonathan Richard Shewchuk. "Triangle: Engineering a 2D Quality Mesh Generator and Delaunay Triangulator." In: *Applied Computational Geometry: Towards Geometric Engineering*. Ed. by Ming C. Lin and Dinesh Manocha. Vol. 1148. Lecture Notes in Computer Science. Springer-Verlag, May 1996, pp. 203–222. DOI: 10.1007/BFb0014497.

[22] Timothy A. Davis. "Algorithm 832: UMFPACK V4.3—an Unsymmetric-Pattern Multifrontal Method." In: *ACM Trans. Math. Softw.* 30.2 (June 2004), pp. 196–199. ISSN: 0098-3500. DOI: 10.1145/992200.992206. URL: https://doi.org/10.1145/992200.992206.

[23] R. B. Lehoucq, D. C. Sorensen, and C. Yang. *ARPACK Users' Guide*. Society for Industrial and Applied Mathematics, 1998. DOI: 10.1137/1.9780898719628.

[24] O. Sauter and S.Yu. Medvedev. "Tokamak coordinate conventions: COCOS." In: *Computer Physics Communications* 184.2 (2013), pp. 293–302. DOI: 10.1016/j.cpc.2012.09.010.

[25] Jong-Kyu Park and Nikolas Logan. *Coordinates – GPEC 1.5.0 documentation*. June 18, 2016. URL: https://princetonuniversity.github.io/GPEC/outputs.html.

[26] Peter Kovesi. *Good Colour Maps: How to Design Them*. 2015. arXiv: 1509.03700 [cs.GR]. URL: https://arxiv.org/abs/1509.03700.

[27] F. Hecht. "New development in FreeFem++." In: *J. Numer. Math.* 20.3-4 (2012), pp. 251–265. ISSN: 1570-2820. URL: https://freefem.org/.

[28] K. R. Richter Oszkár Bíró. *Program package Electromagnetic Field Analysis Tools (EleFAnT3D)*. TU Graz, IGTE. 2000.

[29] A. Kameari. "Calculation of transient 3D eddy current using edge-elements." In: *IEEE Trans. Magn.* 26.2 (1990), pp. 466–469. ISSN: 1941-0069. DOI: 10.1109/20.106354.

[30] L. R. Turner, K. Davey, N. Ida, D. Rodger, A. Kameari, A. Bossavit, and C. R. I. Emson. *Workshops and problems for benchmarking eddy current codes*. Tech. rep. ANL/FPP/TM–224. Argonne National Lab., 1988. URL: http://inis.iaea.org/Search/search.aspx?orig_q=RN:20009769 (visited on 03/10/2021).

[31] J. W. Berkery, Y. Q. Liu, Z. R. Wang, S. A. Sabbagh, N. C. Logan, J.-K. Park, J. Manickam, and R. Betti. "Benchmarking kinetic calculations of resistive wall mode stability." In: *Physics of Plasmas* 21.5 (May 2014), p. 052505. ISSN: 1070-664X. DOI: 10.1063/1.4873894.

[32] Zhirui Wang, Jong-Kyu Park, Yueqiang Liu, Nikolas Logan, Kimin Kim, and Jonathan E. Menard. "Theory comparison and numerical benchmarking on neoclassical toroidal viscosity torque." In: *Physics of Plasmas* 21.4 (Apr. 2014), p. 042502. ISSN: 1070-664X. DOI: 10.1063/1.4869251.

[33] Jong-Kyu Park, Allen H. Boozer, Jonathan E. Menard, Andrea M. Garofalo, Michael J. Schaffer, Richard J. Hawryluk, Stanley M. Kaye, Stefan P. Gerhardt, and Steve A. Sabbagh. "Importance of plasma response to nonaxisymmetric perturbations in tokamaks." In: *Physics of Plasmas* 16.5 (2009), p. 056115. DOI: 10.1063/1.3122862.

[34] N. Leuthold et al. "Progress towards edge-localized mode suppression via magnetic perturbations in hydrogen plasmas." In: *Nuclear Fusion* 64.2 (Jan. 2024), p. 026017. DOI: 10.1088/1741-4326/ad1625.

[35] Y. Q. Liu, A. Bondeson, C. M. Fransson, B. Lennartson, and C. Breitholtz. "Feedback stabilization of nonaxisymmetric resistive wall modes in tokamaks. I. Electromagnetic

model." In: *Physics of Plasmas* 7.9 (Sept. 2000), pp. 3681–3690. ISSN: 1070-664X. DOI: 10.1063/1.1287744.

[36] Yueqiang Liu, M. S. Chu, I. T. Chapman, and T. C. Hender. "Toroidal self-consistent modeling of drift kinetic effects on the resistive wall mode." In: *Physics of Plasmas* 15.11 (Nov. 2008), p. 112503. ISSN: 1070-664X. DOI: 10.1063/1.3008045.